Aerodynamic Analysis of a Novel Wind Turbine for an Omni-flow Wind Energy System

Pei Ying

A thesis submitted to the University of Hertfordshire in partial fulfilment of the requirements of the degree of Doctor of Philosophy

The programme of research was carried out in the School of Engineering & Technology, University of Hertfordshire

April 2016

Abstract

The purpose of this research is to propose a novel wind turbine for an omni-flow wind energy system and investigate its aerodynamic performance. The geometry of the novel wind turbine is based upon the impulse turbine technology which has been successful in wave energy. In this study, both numerical and experimental studies were conducted to evaluate the aerodynamic features of this wind turbine. The numerical method was validated by a comparison between numerical and experimental results over a range of tip speed ratios.

Results obtained from experiments and simulations indicate that the proposed wind turbine can be employed. Additionally, on the basis of the analyses performed, this new wind turbine has the potential for having a good startup feature, which means that this wind turbine can be suitable for applications in an urban environment. As an important component, the stator of this wind turbine can increase the passing flow velocity by 20%. Meanwhile, the passing flow direction also can be optimised by the stator.

Aerodynamics of the wind turbine was analysed under the non-uniform flow condition, because the flow is non-uniform inside the omni-flow wind energy system. It was found that the maximum power coefficient of such a turbine under the non-uniform flow condition is lower than that under the uniform flow condition. Due to the non-uniform flow, the blades experience different flow velocities, and as a consequence, undergo different aerodynamic loads during one operation cycle. Thus the generated torque and thrust on a blade are subjected to frequent and periodical changes.

Influences of the geometrical parameters on the aerodynamic characteristics of this wind turbine were investigated. From the initial study, it was found that changes of hub-to-tip ratios, numbers of blades, aerofoils and numbers of guide vanes, can significantly affect the

power performance. Additionally, the wind turbine obtained high values of maximum torque coefficients with changing geometrical parameters.

To my dear mother and father

谨此献给我亲爱的母亲和父亲

Acknowledgements

Foremost, I wish to express my sincere gratitude to Dr. Yong Kang Chen, Dr. Yi Geng Xu and Dr. Yuan Tian for their invaluable academic supervision. During this period, Dr. Yong Kang Chen guided me with great encouragement and patience through this work.

I wish to thank the School technical staff. Many thanks must be given to the technicians of both the Wind Tunnel Laboratory and the Workshop in the School. Sincere thanks go to administrators in Science and Technology Research Institute.

Heartfelt thanks also go to my close friends, Aiyuan Yang, Zeng Shen, Yang Jiao, Xu Zhang and Chuanli Zhao, who always stand by my side. Thanks go to my friends who always encourage and trust me.

Last but not least, I must thank my family for their support and unconditional love, not just through the past years of my study, but up until now.

Publications

Journal Papers

[1] **P. Ying**, Y. K. Chen, and Y. G. Xu, "An aerodynamic analysis of a novel small wind turbine based on impulse turbine principles," *Renewable Energy*, vol. 75, pp. 37-43, 2015.

[2] **P. Ying**, Y. K. Chen, Y. G. Xu, and Y. Tian**,** "Computational and experimental investigations of an omni-flow wind turbine," *Applied Energy*, vol. 146, pp. 74-83, 2015.

Papers in Conference Proceedings

[3] **P. Ying**, Y. K. Chen, and Y. G. Xu, "Computational Modelling of Blades for a Novel Wind Turbine, " *Proc. of the International Conference on Modelling, Identification and Control*, Wuhan, China, 2012, pp. 878-882.

[4] Y. K. Chen, **P. Ying**, Y. G. Xu, and Y. Tian, "On the turbulent flow models in modelling of omni-flow wind turbine, " *Proc. of the International Conference on Next Generation Wind Energy*, Madrid, Spain, 2014.

Contents

List of Figures

List of Tables

Nomenclature

Latin Symbols

A	projected area of aerofoil (m^2)	T	torque (Nm)
$A1, A2$	entrance area of flow passage (m^2)	T_r	resistive torque (Nm)
B	blade number	u	component of $\vec{U}$ in x direction (m/s)
c	chord of a blade aerofoil (m)		
C_B	correction for blockage effect	u'	fluctuating components of u (m/s)
C_D	drag coefficient		
$\overline{C_f}$	friction coefficient	$\bar{u}$	mean component of u (m/s)
C_L	lift coefficient	u_t	friction velocity (m/s)
C_N	thrust coefficient	$\vec{U}$	velocity vector (m/s)
C_P	power coefficient	$U_{corrected}$	corrected flow velocity in the wind tunnel (m/s)
$C_{P,max}$	maximum power coefficient		
$C_{Pressure}$	pressure coefficient	$U_{covered}$	flow velocity at the entrance for a covered model (m/s)
C_T	torque coefficient		
D	diameter of the chamber (m)	$U_{measured}$	measured flow velocity in the wind tunnel (m/s)
e	error in experiments		
f	frequency (Hz)	$U_{uncovered}$	flow velocity at the entrance (m/s)
F	aerodynamic force (N)		
F'	normal force (N)	v	component of $\vec{U}$ in y direction (m/s)
F_D	drag (N)		
F_L	lift (N)	v'	fluctuating components of v (m/s)
F_N	thrust (N)		
F_T	tangential force (N)	$\bar{v}$	mean component of v (m/s)
L	length of the chamber (m)	y	distance from the wall (m)
$\dot{m}$	mass flow rate (kg/s)	y^+	dimensionless distance from the wall
N	rotational speed (rpm)		
p	pressure (N/m^2)	z	position on z-axis (m)
p_o	reference pressure (N/m^2)	w	component of $\vec{U}$ in z direction (m/s)
P	power output (W)		
r	local blade radius (m)	w'	fluctuating components of w (m/s)
R	blade radius (m)		
Re	Reynolds number	$\bar{w}$	mean component of w (m/s)
t	time (s)		

Greeks symbols

α	angle of attack (^{o})	δ	the max height between the camber line and chord line (m)
γ	correction factor for adding a cover		

η	efficiency	τ_w	wall shear stress (N/ m^2)
λ	tip speed ratio	φ	angle between flow direction and a vertical axis (°)
υ	kinematic viscosity (m^2/s)		
ρ	fluid density (kg/m^3)	ω	angular speed of the rotor (rad/s)
$\bar{\rho}$	mean fluid density (kg/ m^3)		
σ	solidity		

Acronyms

ABS	acrylonitrile butadiene styrene	LES	large eddy simulation
BEM	blade element momentum	MRF	moving reference frame
CFD	computational fluid dynamics	NREL	National Renewable Energy Laboratory
DNS	direct numerical simulation		
HAWT	horizontal axis wind turbine	OWC	oscillating water column
IFGV	impulse turbine with fixed guide vanes	RANS	Reynolds-averaged Navier Stokes equations
ISGV	impulse turbine with self-pith-controlled guide vanes	SST	shear stress transport
		VAWT	vertical axis wind turbine

Chapter 1 Introduction

1.1 Necessity of a Novel Wind Turbine in Urban Areas

Due to the concerns about global warming, wind energy technology has been developed and has become one of the major technologies in the renewable energy field. As shown in Figure 1.1, the capacity of global cumulative wind energy has increased continuously in the last decade. In 2012, an employment of wind energy has avoided € 9.6 billion of fossil fuels costs, which means less CO_2 emissions [1]. In 2020, an estimated € 22 billion in fuel costs can be avoided [1]. In Denmark, wind turbines have provided around 39% of total electricity consumption in 2014 [2]. The European Wind Energy Association predicts that the wind energy will account for 24.4% of the EU's electricity demand in 2030 [3].

In recent years, technologies in wind turbines have matured. Wind turbines generally work well in land based wind farms or in large offshore wind farms, where there is good quality wind [4, 5]. However, wind farms are in remote areas far from residential areas. The electricity produced from wind farms suffers from long-distance transmission through electric grids with high losses and high costs. Due to the size, the modern large wind turbines need a high cost in transportation and installation of components.

In the UK, approximately 50% of energy consumption is in buildings [6]. The UK government has set a target of 80% carbon reduction by 2050 [7]. The wind turbine integrated into building is one of emerging technologies that can reduce CO_2 emission [8, 9]. Compared with large wind turbines in wind farms, small wind turbines that function as distributed electricity generators in urban areas can reduce the power losses and high costs in electricity transmission over long distances. Because the wind speed on tops of buildings can be

significantly higher than that near ground in the urban environment, several types of small wind turbines have been presented for working on the roofs of tall buildings [10, 11].

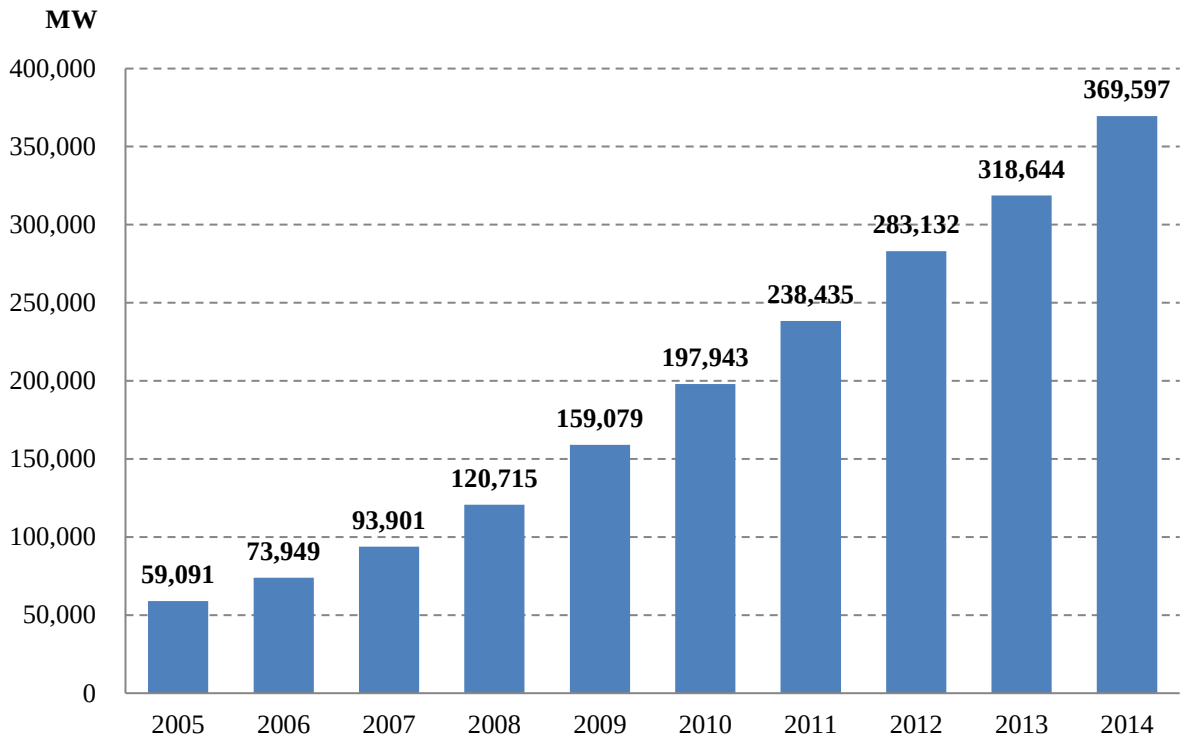

Figure 1.1: Global wind power capacity in 2005 - 2014 [12].

An omni-flow wind energy system has been introduced for urban areas [13]. The term of omni-flow can be defined as the flow of air in omni direction. The omni-flow energy system can accept the omni-directional wind for a downstream wind turbine. Figure 1.2 shows a 3D view of this wind energy system. The wind energy system can receive and effectively transmit wind to a downstream wind turbine. The omni-flow wind energy system can cater for a wide variety of wind conditions without a yaw mechanism. The aerodynamics of such a wind energy system has been studied by Zhang *et al*. [14, 15]. Zhang [15] suggested that this system could be used in the urban areas where wind speed was always low. However, it has been found that the flow velocity distribution is not uniform inside the omni-flow wind

energy system [14, 15]. Blades of a wind turbine have to operate under a non-uniform wind condition, which can result in different aerodynamic loads during one operation cycle.

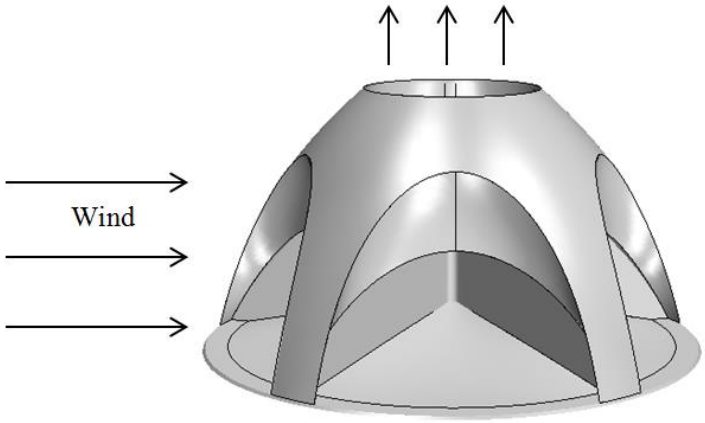

Figure 1.2: Omni-flow wind energy system [15].

Thin blades of current wind turbines are difficult to accommodate the non-uniform flow condition. In this PhD project a new wind turbine is proposed for the omni-flow wind energy system. The proposed wind turbine has a new geometry and no research has been carried out on this new geometry [16]. Much of research about wind turbines is performed under the uniform flow condition [17]. This PhD project studies the aerodynamics of the proposed wind turbine under the non-uniform condition caused by the omni-flow system. Recently, the employment of wind turbines in an urban environment has been receiving increased attention in both academia and industry. This work will contribute to the use of wind turbines in the urban areas, such as the omni-flow wind energy system.

1.2 Project Aim and Objectives

It has been reported that the omni-flow wind energy system can guide the omni wind to a downstream wind turbine and has the potential to be employed in an urban environment [14, 15].

This PhD project proposes a new wind turbine for the omni-flow wind energy system. The project aims to investigate aerodynamics of the proposed wind turbine.

The project has the following objectives:

- A literature review about current small urban wind turbines, impulse turbines and the omni-flow wind energy system.
- Study two common research methods: computational fluid dynamics (CFD) simulation and wind tunnel testing.
- Presentation of the geometry for the proposed wind turbine.
- Test the power output performance and starting capability of the proposed wind turbine in a wind tunnel and validate the numerical approach by a comparison between numerical and experimental results.
- Investigate aerodynamics of the proposed wind turbine under the non-uniform flow condition by the validated numerical approach.
- Study influences of geometrical parameters on the aerodynamic performances of the proposed wind turbine.

1.3 Thesis Layout

There are nine chapters in this thesis. Brief summaries for Chapters 2-9 are shown as follows:

Chapter 2 contains the literature review about current wind turbines, small urban wind turbines, wind characteristics in urban areas, aerodynamic features of the omni-flow wind energy system and the impulse turbine technology.

Chapter 3 reviews two methods, CFD simulation and wind tunnel testing, for aerodynamic investigation of the wind turbine.

Chapter 4 presents the geometry of a novel wind turbine based upon the impulse turbine technology.

Chapter 5 provides aerodynamic analyses of the proposed wind turbine by numerical and experimental methods. The numerical approach is validated by the comparison between numerical results and experiment data.

Chapter 6 addresses aerodynamic performance of the proposed wind turbine under the non-uniform flow condition.

Chapter 7 presents influences of geometrical parameters, such as hub-to-tip ratios, numbers of blades, aerofoils and numbers of guide vanes, on aerodynamics of the proposed wind turbine.

Chapter 8 discusses aerodynamics of the proposed wind turbine by comparing with conventional wind turbines. Performances of the wind turbine under uniform and non-uniform flow conditions and influences of geometrical parameteries are also discussed.

Chapter 9 lists the highlighted foundings of this project. Future work is also suggested.

Chapter 2 Overview of Existing Wind Turbines

This chapter introduces features of conventional wind turbines and wind characters founded in an urban environment. Aerodynamics of the omni-flow wind energy system is addressed. Technologies about impulse turbines are also reviewed.

2.1 Conventional Wind Turbines

Conventional wind turbines can be categorised into two types by the axial direction of a wind turbine: horizontal axis wind turbines (HAWTs) and vertical axis wind turbines (VAWTs). Characteristics, advantages and disadvantages of HAWTs and VAWTs are reviewed in this section.

2.1.1 Horizontal Axis Wind Turbines

A HAWT is a wind turbine whose rotor axis is horizontal and parallel to the wind direction. Employing HAWTs for electricity can be traced back to the late nineteenth century in the USA [18]. The HAWT has been the most common type of wind turbines [18, 19]. A classic structure of a general HAWT is shown in Figure 2.1(a). A high tower is used to place a nacelle and a rotor with long blades. The generator, gear box, brake system and yaw mechanism are placed inside the nacelle. The rotor always consists of two or three blades and a supporting hub. The rotor of a HAWT can be oriented upwind and downwind of the tower. Aerodynamic forces generated on blades rotate the rotor and the generator to produce electricity. In order to obtain a good efficiency, a yaw mechanism is needed to adjust the rotor axis against the wind direction instantly [18]. Recently, HAWTs are always gathered in wild and offshore wind farms, where there is good quality wind, as shown in Figure 2.1(b), and produce electricity for grids.

The power coefficient is an important dimensionless term for all wind turbines to estimate the capability of power generation. The power coefficient is defined as a ratio between the generated power from the wind turbine and the available power from wind [19]. For a modern large HAWT, the peak power coefficient is in a range of 0.4-0.5 [18].

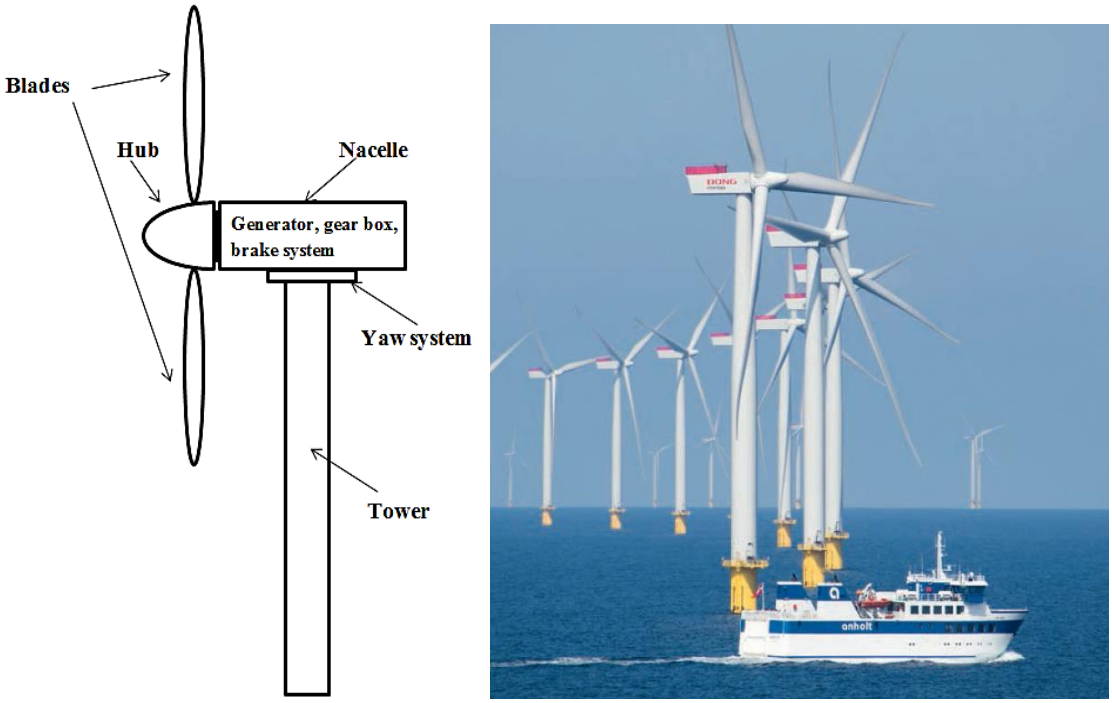

Figure 2.1: HAWTs: (a) schematic view; (b) offshore wind farm [20].

To achieve high power output, long blade radii and high towers are required [19]. Over the last 25 years, the largest rotor diameter of commercial wind turbines has increased from 20 m to 140 m with improving the capability from 50 kW to 7 MW, as shown in Figure 2.2 [21]. But the large rotor diameter causes difficulty and high cost in manufacturing. The installation and maintenance of key components, such as blades, the generator and the control system, on the top of a high tower are also difficult and expensive, especially for offshore applications.

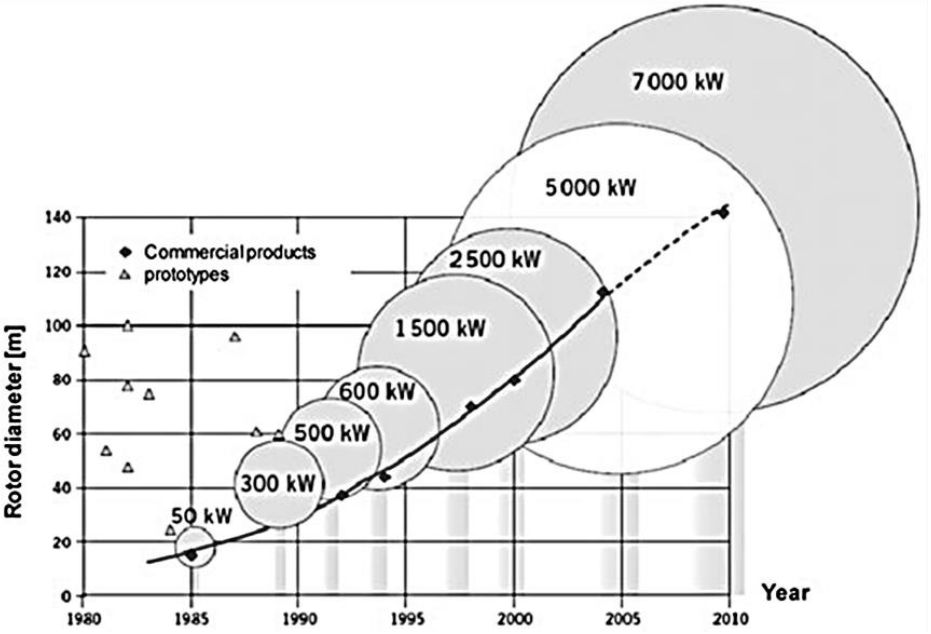

Figure 2.2: Development of the rotor diameter and capability [21].

2.1.2 Vertical Axis Wind Turbines

A VAWT is a wind turbine whose rotor axis is perpendicular to the wind direction and the ground. VAWTs can be divided into two types, the lift driven device and the drag driven device. Savonius wind turbine is a classical drag driven VAWT that was presented by S.J. Savonius in 1920s [22]. A classical structure of a Savonius turbine is shown in Figure 2.3(a). It consists of "S-shape" blades fixed on a vertical axis shaft. The maximum power coefficient of a Savonius wind turbine is approximately 0.2 [23]. The Savonius wind turbine has good starting capability, which is an advantage for working under low velocity wind [24].

The Darrieus wind turbine is a lift driven VAWT that was originally patented by G.J. Darrieus in 1931 [25]. There are two major types of Darrieus wind turbines: the wind turbine with curved "edge beater" blades and the wind turbine with straight blades, as shown in Figures 2.3(b, c). The Darrieus wind turbine can achieve a peak power coefficient of

approximately 0.3 [26]. However, the Darrieus wind turbine has no ability to start up by itself [24].

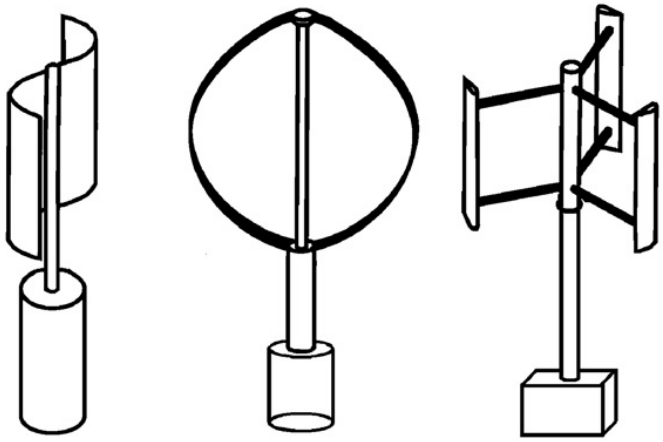

(a) (b) (c)

Figure 2.3: VAWTs: (a) Savonius turbine; (b) classical Darrieus turbine; (c) Darrieus turbine with straight blades [24].

Although VAWTs were firstly used in wind energy utilisation, the interest in VAWTs was lost due to the low power coefficient in the mid-twentieth century [19]. Recently, the research about VAWTs has become popular since it is found that VAWTs are more suitable for low velocity wind and turbulent wind when compared with HAWTs [23]. VAWTs have a number of substantial advantages over HAWTs [24, 27]:

- There is no need of a yaw mechanism because the rotor axis of a VAWT is perpendicular to wind directions at all times.
- The noise level of a VAWT is typically lower than that of a HAWT since the tangential speed at the blade tip of a VAWT is always smaller than that of a HAWT.
- Due to simpler profiles of blades, the manufacturing cost of blades of a VAWT can be lower than that of a HAWT.

- VAWTs have an advantage on safe operation during a gust due to the stalling.

Additionally, key components, such as the gear box, generator system and brake system, can be installed near to the ground. Thus VAWTs are easier to be accessed for installation and maintenance than HAWTs.

However, VAWTs also have disadvantages compared with HAWTs [24]:

- The rotor of a VAWT is not always symmetric to wind direction and not all blades can face to wind. The blade generates negative or zero torque so that the overall torque on the rotor cannot be large enough to rotate the rotor at starting.
- The weight and stress are concentrated on the bottom bearing, which has a risk in structure.
- There is a periodic change of aerodynamic forces on a blade in one revolution, which may affect the structure service life.

2.1.3 Basic Aerodynamics of Aerofoils for Wind Turbines

The blade aerofoil affects performances of a wind turbine, such as power output and starting capability. Many wind turbine blades use existing aerofoils from aircrafts, such as the National Advisory Committee for Aeronautics (NACA) aerofoil family. Several special aerofoil families for wind turbines have been presented for more requirements in the wind turbine industry, such as the National Renewable Energy Laboratory (NREL) [28], Delft University [29], FFA [18] and Risø [30] aerofoil families.

A schematic view of an aerofoil is shown in Figure 2.4(a). A straight line connecting the leading edge and the trailing edge is the chord with a length of *c*. The angle between the wind direction and the chord line is called angle of attack, α. A camber line is the mid-line between

the upper and lower surfaces. The maximum height between the camber line and the chord line is presented as δ and the quantity $\frac{\delta}{c} \times 100\%$ is called the percentage camber of an aerofoil. The percentage camber of an aerofoil is always in the range of 0% - 5% [18]. The percentage camber of a symmetrical aerofoil is 0%.

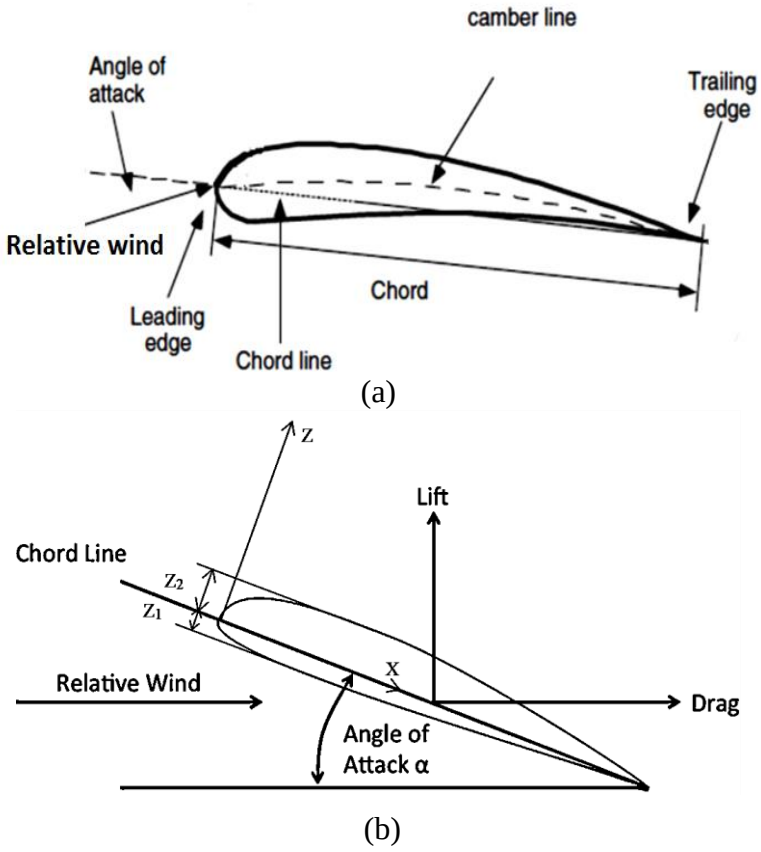

Figure 2.4: An aerofoil: (a) profile [19]; (b) aerodynamic forces [31].

An aerofoil can provide an aerodynamic force to rotate the blade. The aerodynamic force on an aerofoil is defined as follows:

$$C_F = \frac{F}{\frac{1}{2}\rho A U^2} \tag{2.1}$$

where F is the aerodynamic force, ρ is the air density, A is the projected area of the aerofoil and U is the velocity of free stream wind. There are two types of force coefficients of an

aerofoil: lift coefficient and drag coefficient. Lift, F_L, is the force component on the aerofoil perpendicular to the relative approaching wind. Drag, F_D, is the force component parallel to the direction of relative approaching wind. The aerodynamic force diagram on an aerofoil is shown in Figure 2.4(b). Lift coefficient and drag coefficient are defined by [18]:

Lift coefficient: $$C_L = \frac{F_L}{\frac{1}{2}\rho A U^2} \quad (2.2)$$

Drag coefficient: $$C_D = \frac{F_D}{\frac{1}{2}\rho A U^2} \quad (2.3)$$

Values of lift and drag depend on the pressure distribution on the aerofoil. Level of the pressure can be estimated by a dimensionless term, pressure coefficient, which is defined as [31],

$$C_{Pressure} = \frac{p - p_o}{\frac{1}{2}\rho U^2} \quad (2.4)$$

where p is the pressure on an element of the aerofoil surface and p_o is the reference pressure.

Lift coefficient and drag coefficient can be expressed as [31]

$$C_L = cos\alpha \int_0^1 \left(C_{Pressure,lower} - C_{Pressure,upper}\right) d\left(\frac{x}{c}\right) - sin\alpha \int_{Z_1/C}^{Z_2/C} \Delta C_{Pressure,x} d\left(\frac{x}{c}\right) \quad (2.5)$$

$$C_D = sin\alpha \int_0^1 \left(C_{Pressure,lower} - C_{Pressure,upper}\right) d\left(\frac{x}{c}\right) + cos\alpha \int_{Z_1/C}^{Z_2/C} \Delta C_{Pressure,x}\, d\left(\frac{x}{c}\right) \quad (2.6)$$

where $C_{Pressure,lower}$ and $C_{Pressure,upper}$ represent the pressure coefficient on the lower surface and upper surface respectively, $(C_{Pressure,lower} - C_{Pressure,upper})$ is the pressure coefficient difference between the lower surface and upper surface, $\Delta C_{Pressure,x}$ is pressure coefficient difference in the x-axis, c is the blade chord and α is the angle of attack, z_1 and z_2 denote the lowest and highest positions on the aerofoil in the z-axis as shown in Figure 2.4(b).

Figure 2.5 shows the pressure coefficient distribution on an aerofoil. The top curve represents pressure coefficient on the upper surface of an aerofoil and the bottom curve means pressure coefficient on the lower surface. The area enclosed by two pressure coefficient curves represents the pressure coefficient difference. Equation 2.5 shows that a high lift coefficient requires a large pressure difference that means a large area enclosed by the two pressure coefficient curves.

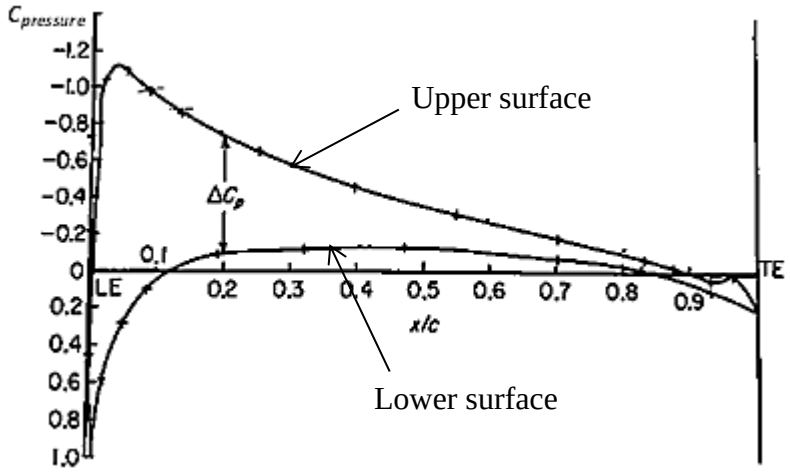

Figure 2.5: Pressure coefficient distribution on the lower and upper surfaces of an aerofoil [31].

2.2 Requirements and Development of Urban Wind Turbines

Wind turbines can be placed in urban areas to provide renewable energy directly for buildings. Employing wind turbines in urban areas is limited by complex wind conditions and wind turbine technologies. Wind characteristics, noise level requirement and development of current urban wind turbines are reviewed in this section.

2.2.1 Wind Characteristics in Urban Areas

Wind is air in motion and generated by atmospheric pressure difference. In urban areas, wind is influenced by various buildings, which results in the low velocity, frequently changed direction and high turbulence intensity [32]. These characteristics cause complexities in efficient utilisation of wind energy.

Wind in urban areas always has low velocities due to influences of various buildings. Drew *et al*. [33] estimated the variability of annual mean wind speeds for typically installing current wind turbines in the Greater London, UK. They found that the wind speed across the Greater London was very low and the wind speed exceeded 4 m/s only at 27% of the neighbourhoods in the city [33]. Millward-Hopkins *et al*. [34] predicted that the long-term mean wind speed in the urban area of Leeds, UK, and found that the wind speed was mostly in a range of 1 m/s to 6 m/s at a height of 3m above a mean building height. It was also reported that there were 2000 – 9500 locations to building-mount wind turbines when the minimum assuming wind speed was 4 m/s and only 10 – 80 locations when the assuming wind speed was larger than 6 m/s in Leeds [34]. In order to produce an efficient power output in urban areas, a wind turbine should start up and capture energy under low velocity wind. Therefore, good starting capability is important for an urban wind turbine.

Balduzzi *et al.* [35] pointed out that the potential of wind energy was dependent on building heights, widths and distances between buildings. If a wind turbine is located in a wrong place in urban areas, it is possible that the power output decreases greatly even wind has high velocity [35, 36]. Investigations about influences of building heights have shown that a chosen building for installing a wind turbine should be higher than surround buildings [37]. In addition to the heights of buildings, the potential of wind energy is also strongly dependant on

the shape profiles of building roofs. Flow characteristics around three roof profiles, namely: pitched roof, pyramidal roof and flat roof, were compared by Led *et al.* [38]. It was reported that a wind turbine mounted on a flat roof had more potential on power generation. A suitable roof has an advantage of accelerating wind speeds so more wind energy can be captured. Abohela *et al.* [37] studied wind features around six types of roofs as shown in Figure 2.6. They found that wind on the vaulted roof had the highest velocity and 56.1% more electricity could be achieved.

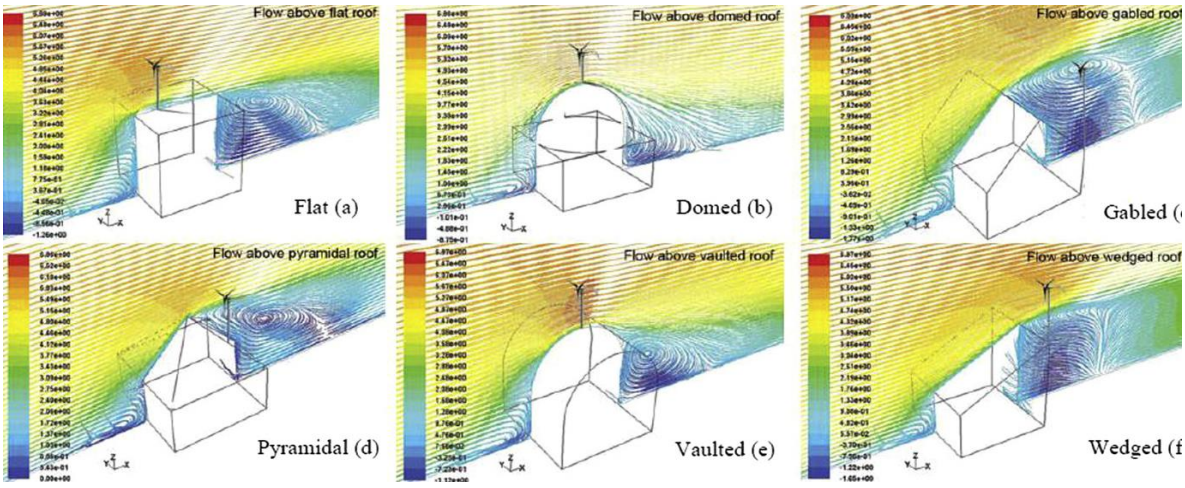

Figure 2.6: Wind velocity fields on different roof shapes [37].

The frequently changed wind direction and high flow turbulence intensity are unavoidable in urban areas. The reason for such complex wind is vortexes around buildings. Figure 2.7 shows the generated vortexes around a block building. It can be seen that there are vortexes on the roof and behind the building. Other presented results show that there can be five vortexes around a building when wind passing [37]. Kotb *et al.* [39] theoretically investigated power output performances of a HAWT under the flow with a swirl. It was reported that the power coefficient under the flow with a swirl was lower by 40% than that under a steady flow [39]. Therefore, an urban wind turbine has to suit the turbulent wind. As mentioned in Section

2.1.2, VAWTs have advantages on operation with turbulent flows in urban areas when compared with HAWTs.

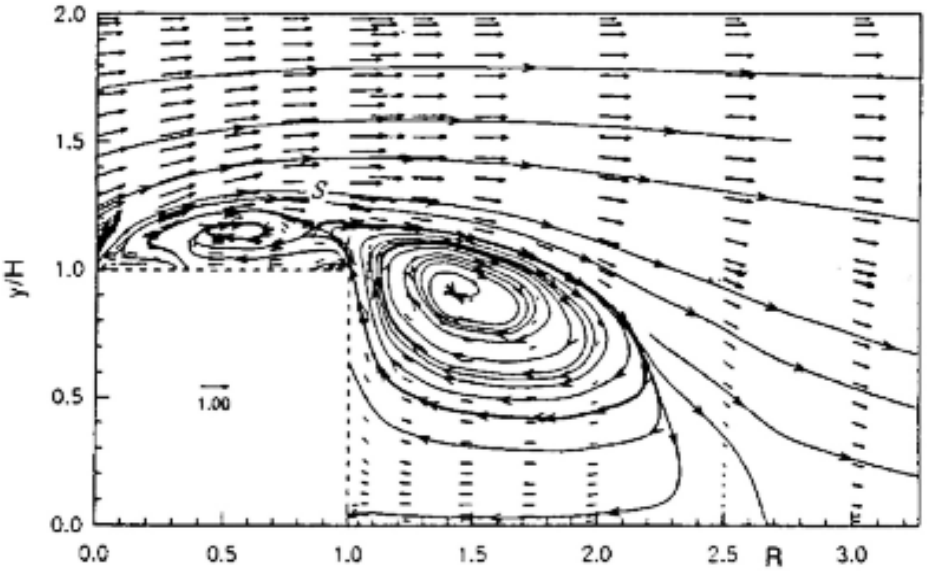

Figure 2.7: Flow velocity field around a block building [40].

2.2.2 Noise

In addition to operation under complex flow conditions, urban wind turbines have to meet requirements about noise. Many countries have noise regulations for public areas and residential areas. However, noise from wind turbines is unavoidable due to aerodynamic interactions of blades, mechanical components and flow passing holes or slits [41]. It was reported that noise from wind turbines could be annoying and associated with some health effects [42]. Compared with other community noise sources, perception and annoyance caused by wind turbine noise are higher at the same sound level due to visual interference and noise characteristics [43]. Noise from small wind turbines in urban areas has been realised as one of the most important sitting constraints.

Sources of noise from wind turbines can be divided into two types: (a) mechanical noise generated from interaction of components, such as gearboxes and generators; (b)

aerodynamic noise produced by wind passing blades [44]. Mechanical noise has been almost solved, thus reducing the aerodynamic noise level is a topic of considerable research in the wind energy field [44].

Since aerodynamic noise generation is very sensitive to the rotational speed, an efficient way to decrease aerodynamic noise is to reduce the rotational speed [41, 44]. Vick *et al.* [45] tested the noise level of a 3m-diameter three-blade HAWT under different rotational speeds. They found that the wind turbine achieved the maximum noise level of approximately 90 dB at the maximum rotational speed of 900 rpm. By reducing the rotational speed to 600 rpm, the measured noise level was less than 60 dB.

In addition to the good performance under complex wind conditions and the low working noise level, some other features needed for an urban wind turbine can be considered as follows [46]:

- Safe operation
- Minimised cost in maintenance
- Simple, rugged design and appearance

2.2.3 Existing Urban Wind Turbines

Wind turbines that function as distributed electricity generators can provide electricity directly for buildings, which can reduce the power losses in electricity transmission over long distances and cost on grids. The utilisation of wind turbines in urban areas is also an efficient method to reduce the building carbon emission. Wind turbines can be divided into four types by the rotor diameter [47]: i) micro-scale (rotor diameter < 0.1 m); ii) small-scale (0.1 m < rotor diameter < 1 m); iii) middle-scale (1 m <rotor diameter < 5 m) and iv) large-scale (rotor diameter > 5 m). Micro-scale wind turbines cannot generate enough electricity to satisfy the

electric requirement of buildings. Both middle-scale and large-scale wind turbines have high requirements for space and installation of such a wind turbine may influence structures of buildings. Therefore, small-scale wind turbines are suitable to be used for buildings. Small-scale wind turbines can be categorised into three types: small-scale conventional wind turbines; small-scale conventional wind turbines with added shrouds; re-designed small-scale wind turbines. Three types of urban wind turbines are reviewed in following subsections.

2.2.3.1 Small-scale Conventional Wind Turbines

A small-scale wind turbine has lower efficiency than a large-scale wind turbine due to low Reynolds numbers (Re < 500,000) [48]. With low Reynolds numbers, laminar separation and laminar separation bubbles are generated on the blade of a small wind turbine [49]. The laminar separation and laminar separation bubbles affect the aerodynamics of blades and result in the poor power generation and start-up capability [50]. Statistics show that 97% of all micro/small wind turbines are HAWTs in the UK [51]. Kishore and Priya [52] summarised performances of fourteen small HAWTs as shown in Table 2.1. It can be found that the minimum and maximum values of the overall efficiency are 12% and 26%.

Table 2.1: Efficiency of several current small-to-middle scale HAWTs [52].

Number	Description	Rotor diameter (cm)	Rated wind speed (m/s)	Overall efficiency
1	NE-100S	120	10	14%
2	NE-200S	130	11	18%
3	NE-300S	130	13	17%
4	Energy Ball V100	110	10	17%
5	Micro Wind Turbine	23.4	2-7	18% *
6	TAOS 600	180	12.5	20%
7	Chinook 200	100	12.5	21%
8	EP-220	137	12.5	12%
9	Bornay 600	200	11	23%
10	AC 120	120	9	24%
11	AC 240	165	9	25%
12	µF500	50	12	25%
13	Alladin 400	130	12.5	25%
14	Superwind 350	120	12.5	26%

*power coefficient

There are several methods to enhance the low efficiency of a small-scale wind turbine, such as aerofoils designed for low Reynolds numbers and optimised blades.

The blade aerofoils working under low Reynolds numbers have been developed. Singh *et al.* [48] designed an AF300 aerofoil and studied its aerodynamic features by experimental and numerical approaches under low Reynolds numbers. Compared with the other eight aerofoils,

the optimised AF300 aerofoil has both a high lift coefficient and a high lift-to-drag ratio with low Reynolds numbers. Moreover, a blade with this aerofoil can have low cut-in wind speed and fast start-up [48]. Selig and McGranahan [53] studied six aerofoils of E387, FX63-137, S822, S834, SD2030 and SH3055 for small HAWTs with a wind tunnel and investigated aerodynamic characteristics of each aerofoil under the Reynolds number range from 100, 000 to 500,000. Gieuere *et al.* [54] compared fifteen aerofoils for an optimal operation with low Reynolds numbers. They suggested that an aerofoil with a high lift-to-drag ratio was suitable for variable-speed HAWTs, an aerofoil with a wide lift range was suitable for variable-pitch HAWTs and an aerofoil for stall regulated HAWTs should be insensitive to roughness. Henriques *et al.* [55] proposed a pressure-load inverse approach to design an aerofoil of small wind turbines for the urban environment and found that an aerofoil designed by this approach could reduce the leading edge suction peak, control the soft-stall behaviour and increase the maximum lift.

In addition to development of low Reynolds number aerofoils, other geometrical parameters of blades also can be optimized to suit the urban environment. Singh and Ahmed [49] investigated influences of blade pitch angles of a two-blade small HAWT with an aerofoil of AF300. They found that with an optimal pitch angle of 18^{o}, the instantaneous cut-in wind speed was reduced from 3.58 m/s to 2.34 m/s and the peak power coefficient was increased from 0.15 to 0.255 under a wind speed of 6 m/s [49].

A start-up capability is important for wind turbines in urban areas [56]. Multiplying blades can achieve a greater value of torque and improve the start-up behaviour of a wind turbine [18]. Typically, a HAWT with five blades has the better start-up capability than that with two blades [18]. Duquette and Visser [57] studied relationships between power coefficient and

solidity of a HAWT. The solidity represents the blade number of a wind turbine and is defined as total blade area divided by the rotor disc area [18]

$$\sigma = \frac{B}{2\pi}\frac{c}{R} \tag{2.7}$$

where B is number of blades, c is the blade chord and R is the radius of blades. They found that the wind turbine with a solidity of 15% – 25% had the highest maximum power coefficient. The lower cut-in wind speed, the less blade erosion and lower noise were also found as additional advantages [57].

Several small wind turbines can be installed on the top of a building as a wind farm, as shown in Figure 2.8. This method increases the total generated power output greatly. Sixteen small wind turbines were installed on a top of a building in Manchester, which may be one of the first mini wind farms on a building in the UK [58]. The layout of wind turbines on a roof should be considered because wakes behind wind turbines can diminish the power generation of downstream wind turbines [59].

Figure 2.8: HAWTs placed multiply on a roof [58].

Howell *et al.* [27] studied a 0.6m-diameter Darrieus wind turbine with straight blades and the wind turbine obtained the maximum power coefficient of 0.2. Pope *et al.* [60] predicted that a Savonius VAWT with a rotor diameter of 2 m could achieve the maximum power coefficient

of 0.18. Akwa *et al.* [61] reviewed the effects of geometrical parameters, such as end plates, aspect ratios, overlap, number of buckets, buckets spacing and rotor shapes, on the performance of a Savonius wind turbine. The maximum averaged power coefficient of Savonius wind turbines is in a range of 0.05 - 0.3 [61]. Although the power coefficient of a small VAWT is always lower than that of a small HAWT, VAWTs have advantages under turbulent wind in an urban environment when compared with HAWTs [23, 27].

2.2.3.2 Small-scale Wind Turbines with Added Shrouds

Adding shrouds on small-scale wind turbines is a remarkable approach to accelerate the speed of the passing wind so that a wind turbine can start up easily and produce more power output. There are two popular types of shrouds: shrouds for small HAWTs, such as diffusers and ducts; shrouds for small VAWTs, such as guide vanes.

A schematic view of general diffuser shrouds is shown in Figure 2.9. A wind turbine is placed inside the shroud and near the flow inlet. Concentration of wind energy by a diffuser was proposed around 1980 [62-64]. The diffuser can cause a larger flow pressure difference between front and behind of a wind turbine to increase the flow speed [65]. Because the wind power is proportional to the wind velocity cubed, a slight increment on the wind velocity can provide a large increment of the wind power [18]. Kishore *et al*. [47] found that with an aid of the diffuser as shown in Figure 2.9, the power output was increased by 40% - 60%, when compared with a bare one.

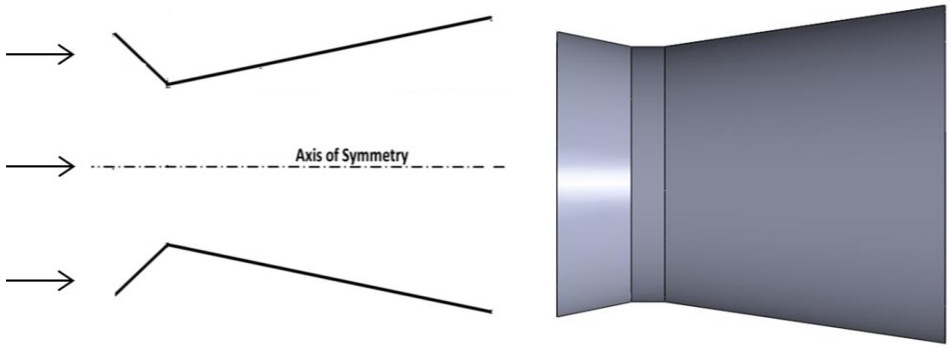

Figure 2.9: Schematic views of the diffuser for HAWTs [47].

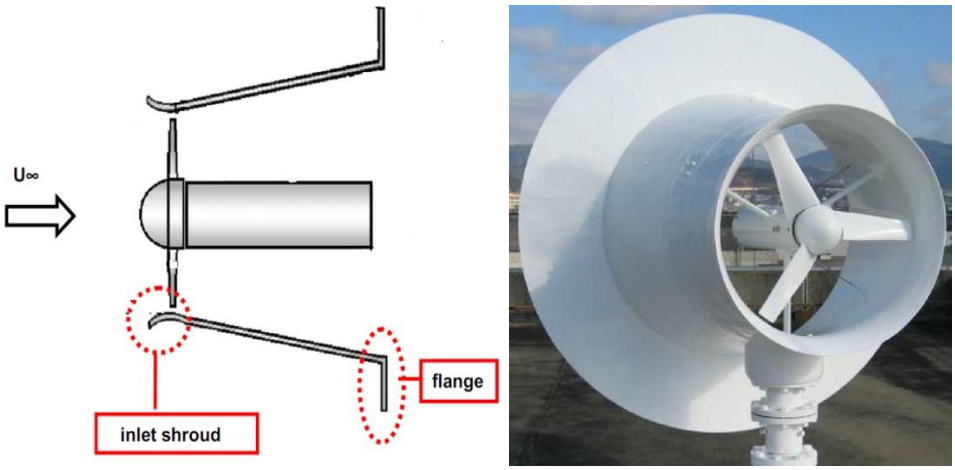

(a) (b)

Figure 2.10: HAWT with the flanged diffuser: (a) schematic view; (b) prototype [66].

A flanged diffuser is an improved type. Figure 2.10 shows the geometry of a flanged diffuser. The flange can produce a large flow separation behind the diffuser and attract more wind entrancing [65]. Ohya *et al.* [66] found that the power output of a HAWT was improved 4-5 times when the flanged diffuser was used. Their results showed that the achieved maximum power coefficient of 1.4 had exceeded the Betz limit of 0.59 [66]. However, it should be noted that employing a diffuser has to add more weight and stresses on the tower of a HAWT.

In addition to the diffuser, a duct is another type of shrouds designed for HAWTs. Figure 2.11(a) shows the duct geometry. The duct can change wind direction from horizontal to

vertical. Moreover, experiments have shown that this duct can accelerate the wind velocity up to 30% [67]. As an advantage, it is possible that installing several ducted wind turbines in a row along the roof and wall edges of a building for more power output. But it should be noted that a drawback for the duct is the restriction to the angle of incident wind. It was reported that the ducted wind turbine only operated well in a range of incident wind angle of $\pm 60^{o}$ [67]. Hu and Cheng [68] designed a duct with a nozzle outlet as shown in Figure 2.11(b). The nozzle outlet can increase the passing flow velocity. They found that the maximum flow velocity was increased by 60% inside the duct, but the performance of the wind turbine was also limited by the angle of incident wind [68].

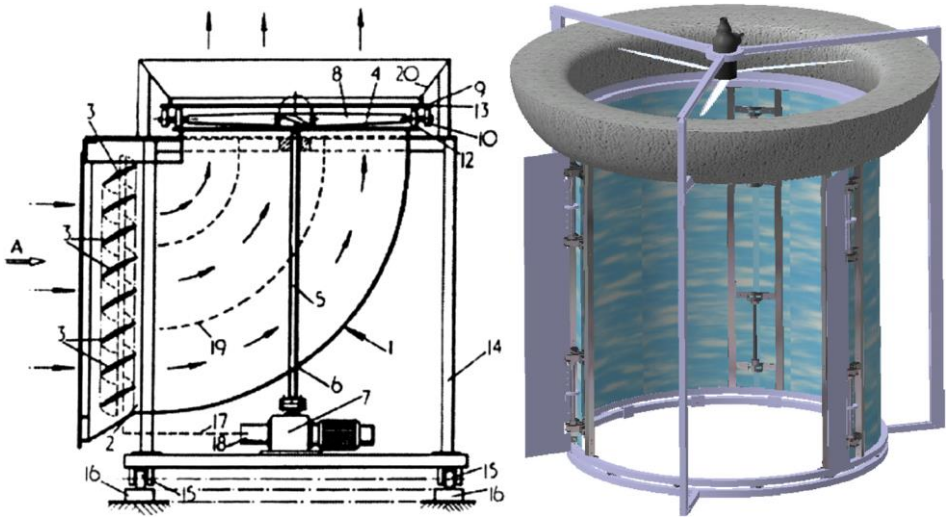

(a) (b)

Figure 2.11: Ducted wind turbines: (a) original type [69]; (b) a bucket-shape duct with a nozzle [68].

Ahmed [70] proposed a duct with a group of guide vanes which could lead air flow downwards as shown in Figure 2.12. This duct combines some features of diffusers and ducts. This device can capture wind and lead wind to the vertical direction inside the shroud. The maximum flow speed inside the shroud was increased by 20-30% [70]. This wind turbine

type is easy for maintenance since the generator can be placed near ground. But a drawback is the restriction to the angle of incident wind because of the guide vanes.

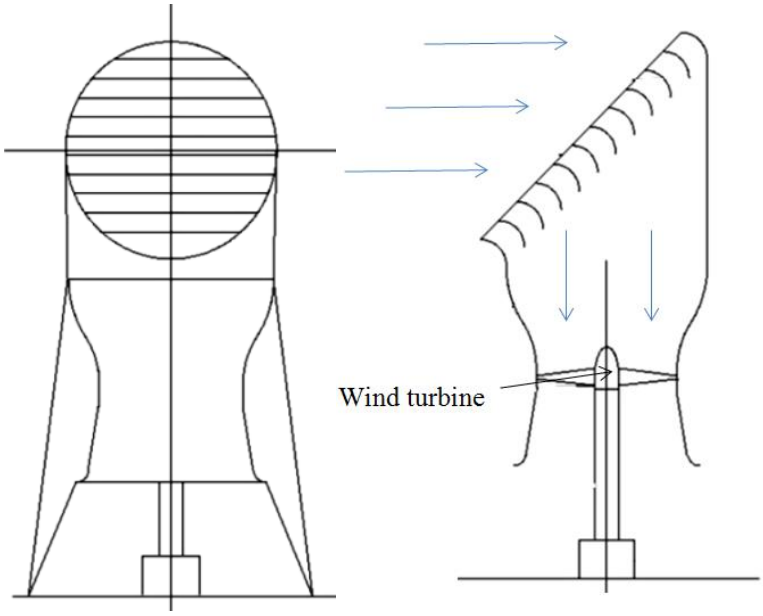

Figure 2.12: A shroud present by Ahmed [70].

Chong *et al.* [9] presented a 5-blade Darrieus wind turbine with surrounded guide vanes. As shown in Figure 2.13, the guide vanes have simple plate geometry and are installed with a setting angle. These guide vanes can lead wind from any direction to an optimum direction for downstream blades. They found that the maximum rotational speed was increased by 182% with the aid of guide vanes [9]. The power output of the wind turbine with guide vanes was 3.48 times as much as that of a bare one [9]. The passing wind speed was accelerated and the cut-in wind speed was reduced. So this wind turbine can start at a low wind speed and have more working hours [9].

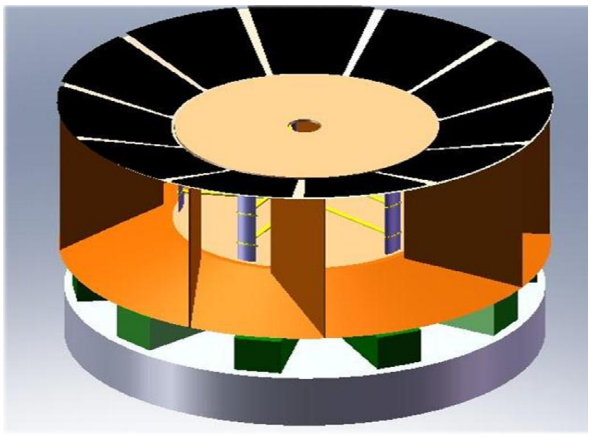

Figure 2.13: An urban VAWT with guide vanes [9].

Employment of shrouds is also available for Savonius wind turbines. Current types of shrouds include obstacles, curtain arrangements and guide-box tunnels. Mohamed *et al*. [71] presented a simple obstacle for shielding the returning blade of a Savonius wind turbine as shown in Figure 2.14(a), and found that the power coefficient of this Savonius wind turbine was improved by more than 27% [71]. Altan and Atılgan [72] introduced a curtain arrangement to improve aerodynamic features of a Savonius wind turbine. As shown in Figure 2.14(b), the curtain arrangement is placed in front of a rotor to concentrate wind energy for the rotor. Compared with the obstacle, the curtain arrangement is more complex but has the better performance. It was reported that the curtain arrangement prevented a negative torque opposite to the rotor rotation and the maximum power coefficient increased from about 0.16 to 0.39 [72]. Irabu and Roy [73] designed a rectangular guide-box tunnel as shown in Figure 2.14(c), and reported that the maximum power coefficient was improved by 23% for a two-blade Savonius rotor with this guide-box tunnel and 50% for a three-blade one with this tunnel [73]. The above three types of added devices have significant improvements on power output. However, it should be pointed out that the performances of these added devices greatly depend on wind directions [71-73].

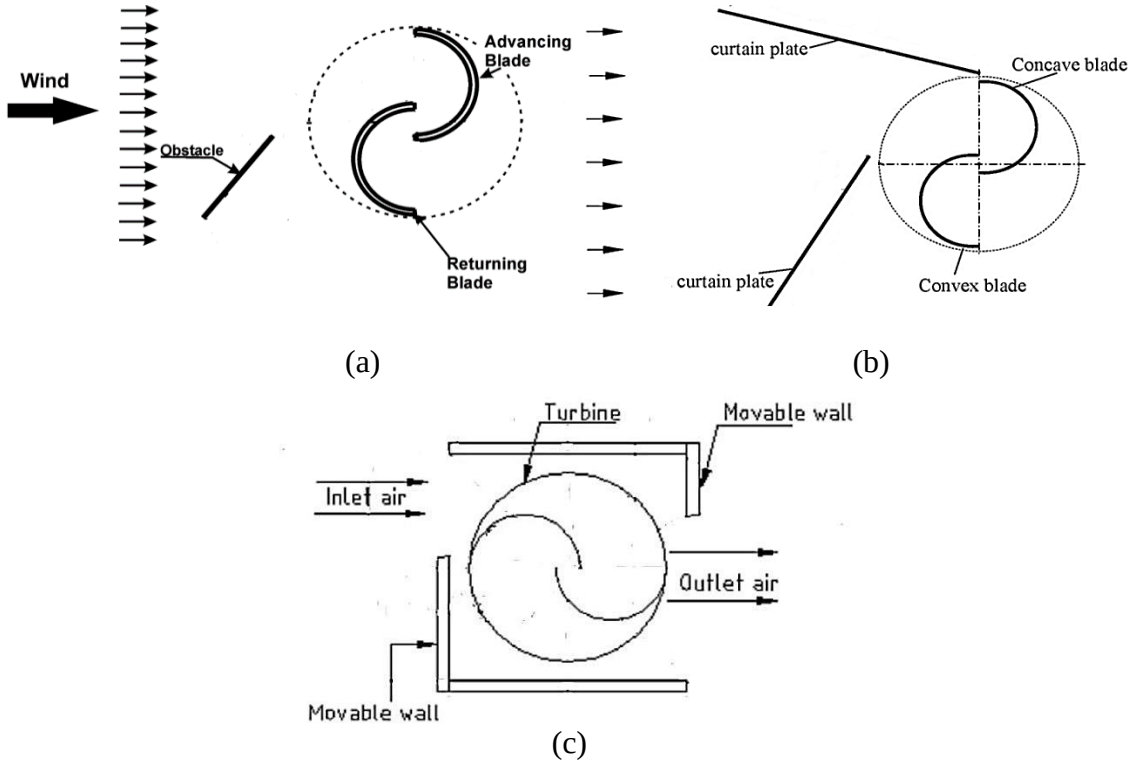

Figure 2.14: Three types of shrouds for a Savonius wind turbine: (a) obstacle [71]; (b) curtain arrangement [72]; (c) guide-box tunnel [73].

Different types of shrouds for HAWTs and VAWTs have been reviewed in this subsection. These shrouds can significantly improve power output and starting capability. However, there are some drawbacks of these devices, such as additional weight on structures and performances depending on wind direction.

2.2.3.3 Re-designed Wind Turbines

In addition to the optimisation of conventional wind turbines or utilisation of shrouds on them, several different wind turbine designs are introduced in this section.

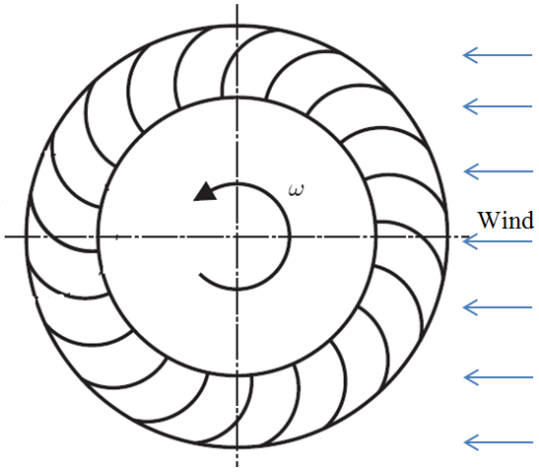

Figure 2.15: A turbine with a crossflow runner [74].

A wind turbine with a crossflow runner was designed by Dragomirescu [74] for good starting behaviour and high power coefficient, even under poor wind conditions. As shwon in Figure 2.15, the simple geometry makes it easier to be manufactured. Numerical results showed that the wind turbine obtained a large value of power coefficient of 0.45, when compared with other VAWTs [74]. The starting torque coeffcient for this wind turbine was 3.6, which means the turbine could start fast even under low velocity wind. However, this wind turbine had a great narrow range of tip speed ratios, which could result in high sensitivity of power coefficient to wind speed. Condsidering the large torque coeffcient and the ability about operating under the 360^{o} flow direction, this wind turbine has the potentional to be utilised in urban areas, but further performance validations are required.

The Sistan wind turbine was employed in the Greater Khorasan and Sistan Basin in the AD 9th century [75]. One of the advantages of Sistan wind turbines is the simplicity of its blades, compared with Darrieus wind turbines and HAWTs. A Sistan wind turbine with guide vanes was present to be used on tops of buildings by Chong *et al.* [76, 77]. Figure 2.16(a) shows the 0.54m-diameter three-blade Sistan wind turbine with a group of guide vanes. It can be seen

that every guide vane has a different shape that may increase manufacturing cost. Results showed that the maximum rotational speed was increased by 75.16% and the increment of power output was 5.8 times under a wind speed of 3 m/s [76]. But it should be noted that its performances were dependent on wind directions. Müller *et al.* [75] also presented a 0.6m-diameter Sistan wind turbine with a shroud for building integration as shown in Figure 2.16(b) and found that the peak efficiency was increased by 48%. The shroud has a simpler profile than others [76, 77]. However, one drawback is the sensitivity of the wind turbine performance to the wind direction.

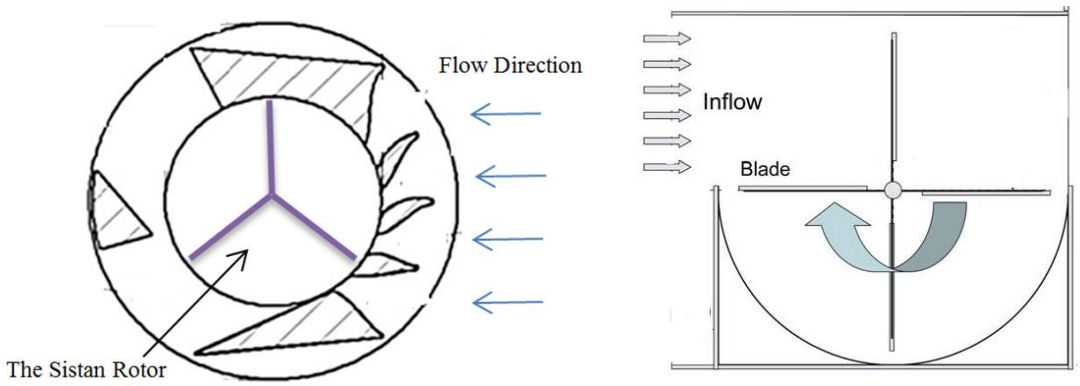

Figure 2.16: Sistan wind turbine: (a) with guide vanes [76] ; (b) with a shroud [75].

Zephyr wind turbine is a vertical axis wind turbine that employs a Savonius wind turbine shape and guide vanes with reverse winglets to optimise approaching wind [78]. Figure 2.17 shows its schematic views. Wind properties were affected by guide vanes for a higher pressure on the pressure surface of the rotor blade [78]. One of advantages of this wind turbine is that it can capture wind from all directions (360^{o}). It was found that the maximum power coefficient of the zephyr wind turbine was 0.12 [78]. The structure of this wind turbine can work with high turbulence wind in urban areas and its performance is independent on

wind directions, therefore Pope *et al.* [78] suggested that this wind turbine could be used in urban areas.

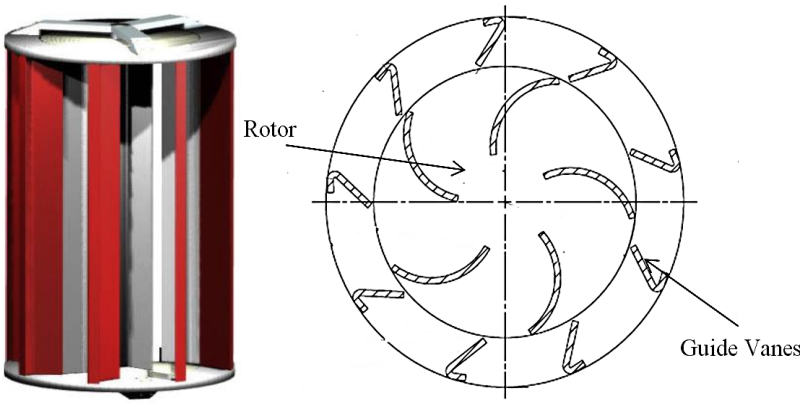

(a) (b)

Figure 2.17: Zephyr wind turbine: (a) 3D view; (b) schematic view [78].

(a) (b)

Figure 2.18: Crossflow wind turbine: (a) concept; (b) architectural integration with ridge [79].

Sharpe and Proven [79] presented a conceptual crossflex wind turbine. Figure 2.18(a) shows that the wind turbine has a Darrieus turbine shape and is placed on a frame with a shaft. They reported that this wind turbine had the low solidity and the low inertial mass design, and predicted that the produced noise would be low due to absence of blade tips [79]. Loads on structure mountings and vibration would be lower than those of small-scale HAWTs and

Darrieus VAWTs [79]. A significant advantage is that the crossflex wind turbine has a good integration with buildings. As shown in Figure 2.18(b), this wind turbine is suitable to be integrated with edges or corners of buildings.

Snaker and Tiryakioglu [80] presented a named Aeolum Harvester wind turbine as an alternative to Savonius wind turbines. Figure 2.19(a) shows the segment of this conceptal wind turbine. Each segament has an inlet where the speed of air flow can be increased. 3D view of the wind turbine is shown in Figure 2.19(b). Each segment has an angular offset from the next segment about the vertical axis. McTavish *et al.* [81] carried out static and dynamic analyses about the torque characteristcs and found that this wind turbine generated a comparable amount of static torque to a Savonius VAWT.

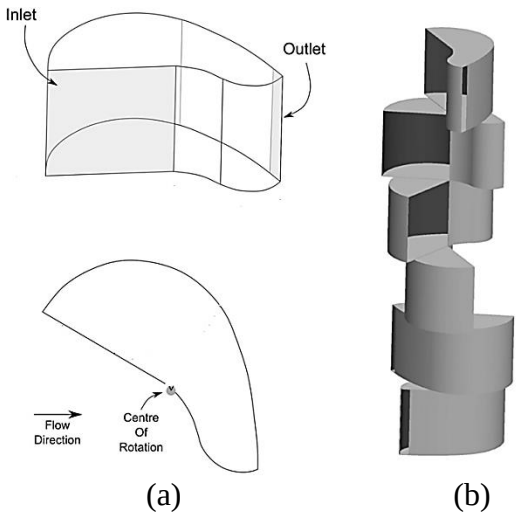

Figure 2.19: VAWT with segments: (a) wireframe view; (b) 3D model [81].

In this subsection, the literature review shows that several urban wind turbines have the potential for working in an urban environment, such as starting characteristics, integration with buildings and simple structures. However, it must be pointed out that there are only preliminary results about some urban wind turbines, such as the crossflow runner and the Aeolum Harvester wind turbine, so more investigations about them are needed.

2.2.3.4 Summary

In this section, various existing designs of wind turbines operating in urban areas have been discussed, such as conventional wind turbines, wind turbines with shrouds and re-designed wind turbines. The literature review shows that these wind turbines have drawbacks in the urban environment, such as the restriction to the wind direction. An omni-flow energy system has an advantage on accepting the omni-directional wind in the urban environment and its features are reviewed in the following section.

2.3 Omni-flow Wind Energy System

An omni-flow wind energy system has shown the potential to be used in the urban environment [14, 15]. The concept of an omni-flow wind energy system was patented by Sureshan in 2008 [13]. Zhang [15] developed the system by numerical and experimental studies. The omni-flow wind energy system can be installed on tops of high buildings in urban areas as shown in Figure 2.20. Rich wind energy can compensate electricity consumption of high buildings with this system for both economic and environmental protection purposes. In Zhang's study, the bottom diameter of the omni-flow wind energy system is 1 m [15]. Because some facilities like air conditioners on roofs may limit the space for installations, this omni-flow system has a small size. And the cost of the small size system can be low. This section reviews key findings about the omni-flow wind energy system from Zhang's research [15].

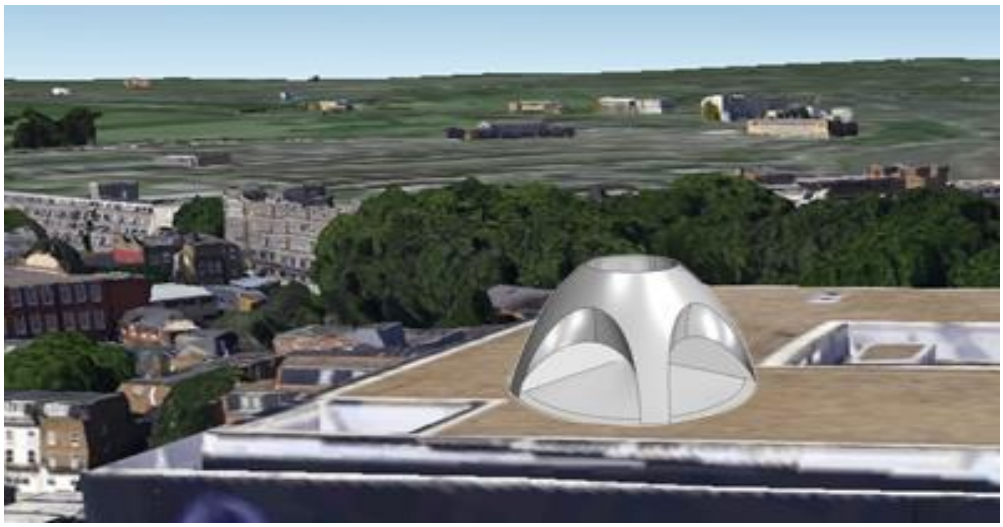

Figure 2.20: Illustrative view of the omni-flow wind energy system on the top of a building. The background is a modified view of London by Google Earth.

2.3.1 Geometry of Omni-flow Wind Energy System

Geometry of the omni-flow wind energy system is shown in Figure 2.21. The omni-flow wind energy system includes a shroud and five chambers. The five chambers are located along the circumference of a shroud to capture wind from any direction and lead wind to the vertical outlet through chambers. Thus, the wind energy system is suitable for the wind with frequent changes in urban areas [15]. A wind turbine can be located near the outlet inside the system. Key components of a wind turbine, such as turbine blades, can be placed inside the shroud for protection. The shroud and chambers form a nozzle structure to increase the velocity of the passing flow.

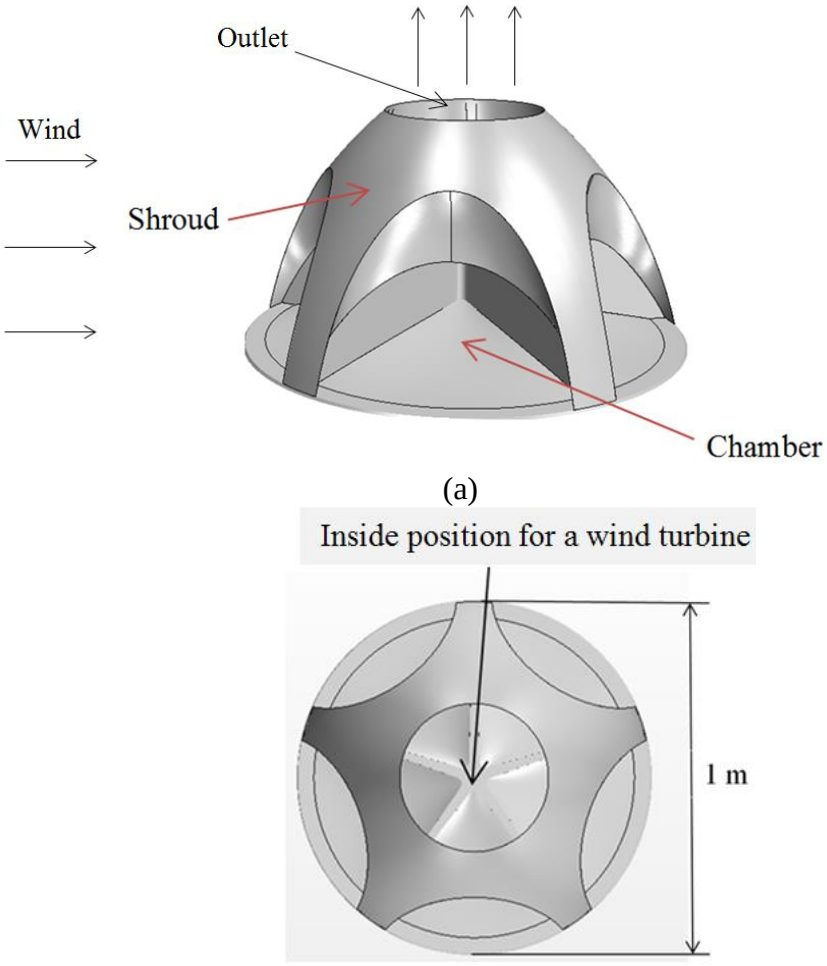

Figure 2.21: The omni-flow wind energy system: (a) left view; (b) top view.

2.3.2 Flow Characters inside Omni-flow Wind Energy System

Flow characters inside the omni-flow wind energy system have been studied by experiments and simulations [14, 15]. According to the angle between wind and a reference line, four wind directions, 0^o, 12^o, 24^o and 36^o, are categorised for investigating the omni-flow wind energy system as shown in Figure 2.22.

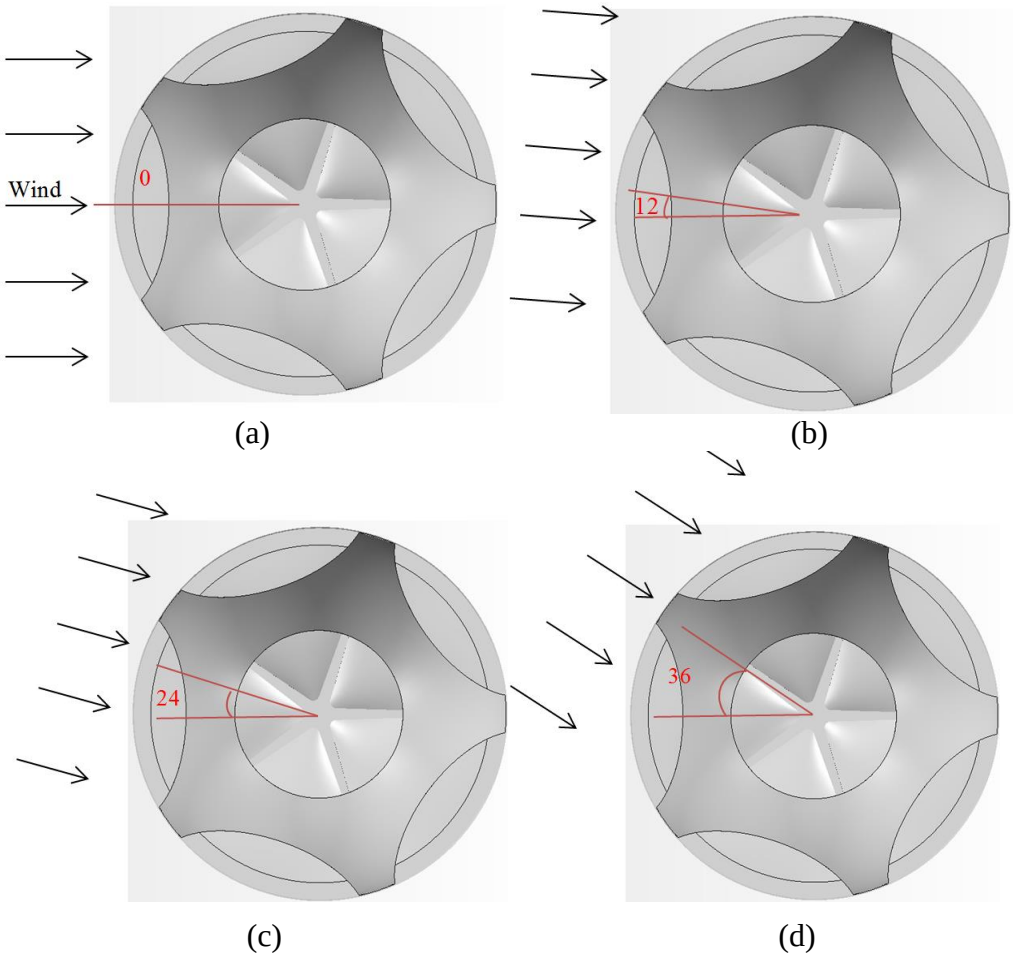

Figure 2.22: Four wind directions for the omni-flow wind energy system: (a) 0º; (b) 12º; (c) 24º; (d) 36º.

Distributions of flow velocity at the outlet of the shroud under four flow directions are shown in Figure 2.23, when the velocity of free stream is 10 m/s [15]. It can be seen that the distribution of flow velocity inside the shroud is non-uniform. The flow velocity field can be divided into two regions: a high velocity region and a low velocity region. The flow in the high velocity region comes from the chambers that are against to wind. When the wind direction is at 0º, only one chamber is against to wind, therefore the high velocity region occupies 1/5 of the outlet area as shown in Figure 2.23(a). Under the wind directions at 12º,

24° and 36°, the high velocity region is expanded up to 2/5 of the outlet area as shown in Figures 2.23(b-d).

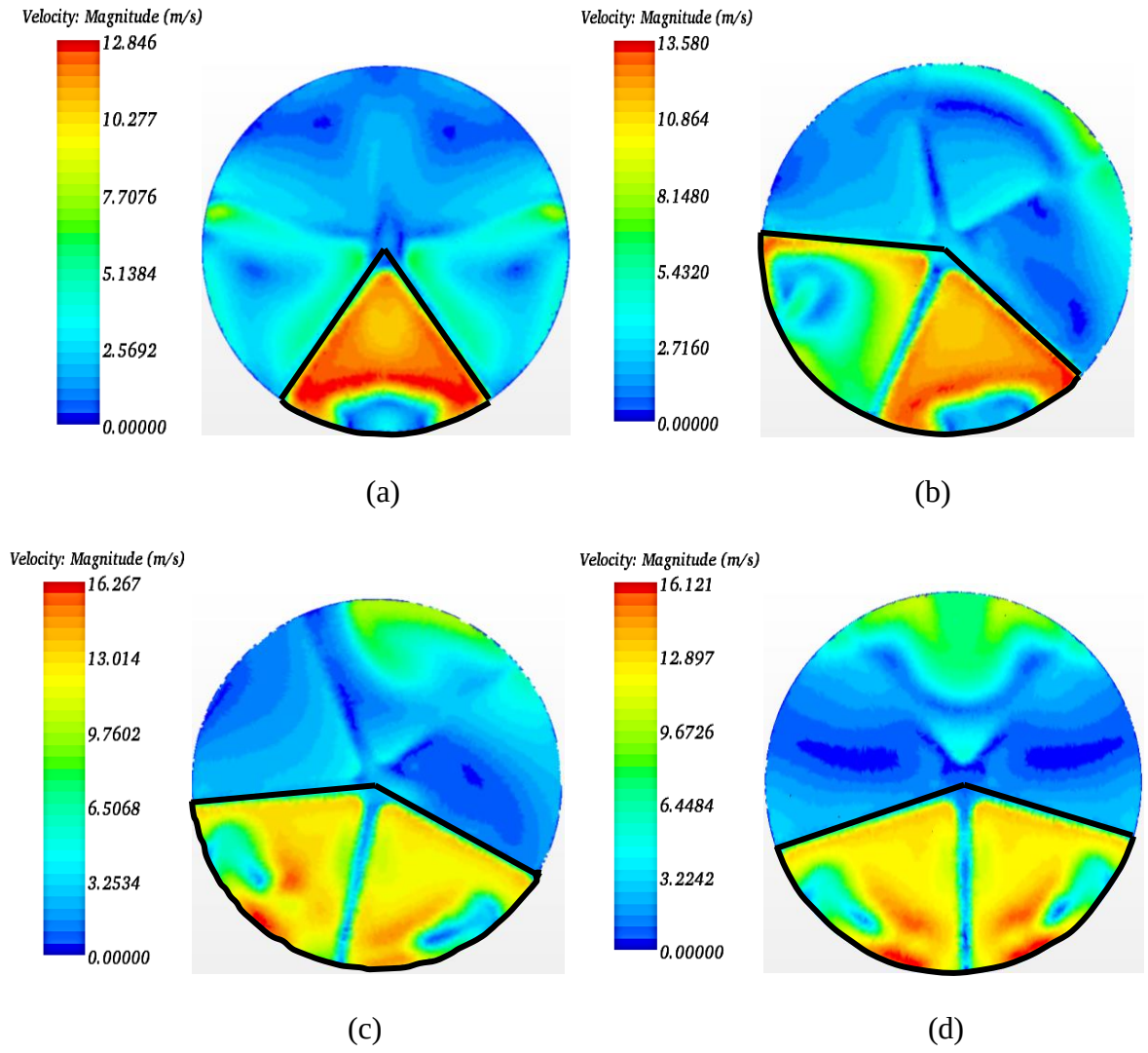

Figure 2.23: Velocity distributions at the outlet of the omni-flow system under four wind directions: (a) 0°; (b) 12°; (c) 24°; (d) 36° [15].

Due to structure features of the omni-flow system, the passing flow velocity can be increased. Values of the maximum and average flow velocities at the outlet are shown in Figure 2.24. With the free stream of 10 m/s, the maximum velocity at the outlet is increased by 46%, 50%, 59% and 69% under wind directions of 0°, 12°, 24° and 36°, respectively [15]. The maximum velocity of the passing flow has the highest value of 16.9 m/s at 36° and the lowest value of

14.6 m/s at 0°. The average velocities are increased by 3% – 12% compared with the free stream velocity [15]. Such an increment on the flow velocity can provide a large increment on the output power from the wind [65].

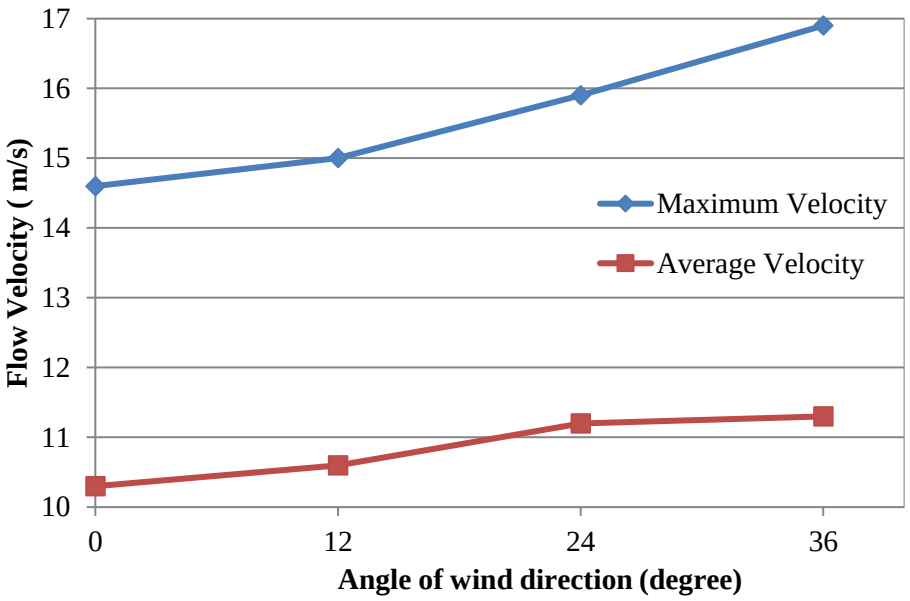

Figure 2.24: The maximum and average velocities at the outlet of the omni-flow system under four wind directions [15].

The omni-flow wind energy system also affects the flow direction greatly. A vector field on an axial section plane is shown in Figure 2.25. The vortex behind the system can influence the passing flow inside the shroud so that the passing flow direction inside the omni-flow system is not ideal vertical [15]. The vector field at a horizontal section plane inside the shroud is shown in Figure 2.26. Small vertexes can be seen inside the omni-flow system, which cause the flow direction non-uniform too.

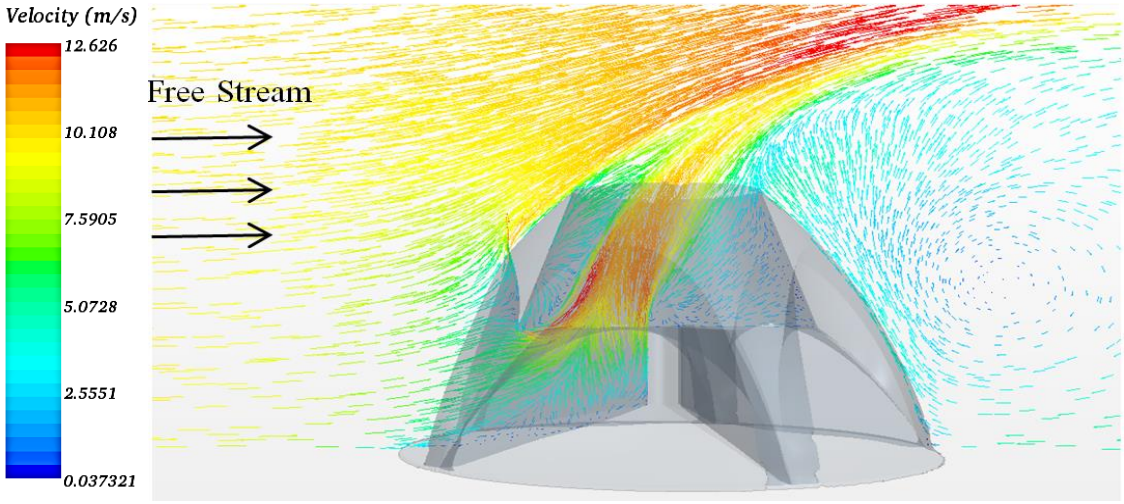

Figure 2.25: Flow velocity vector field through the omni-flow system [15].

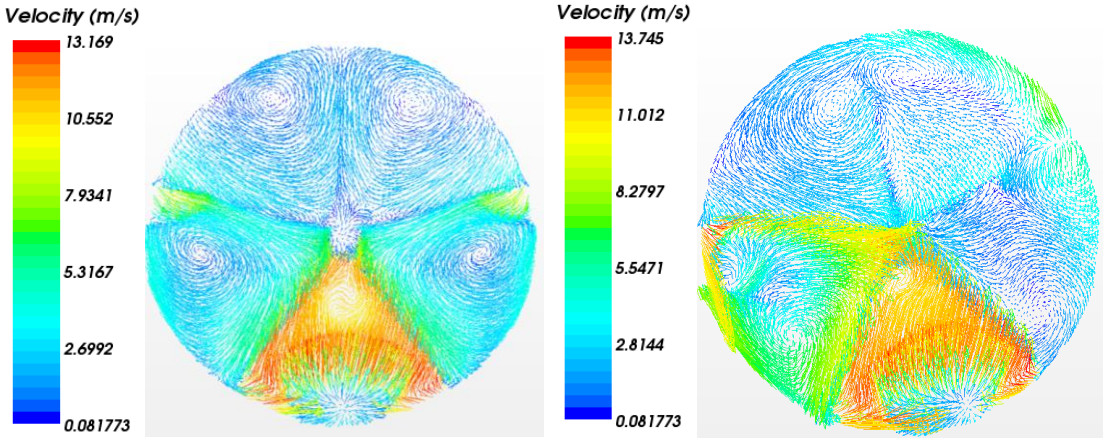

(a) (b)

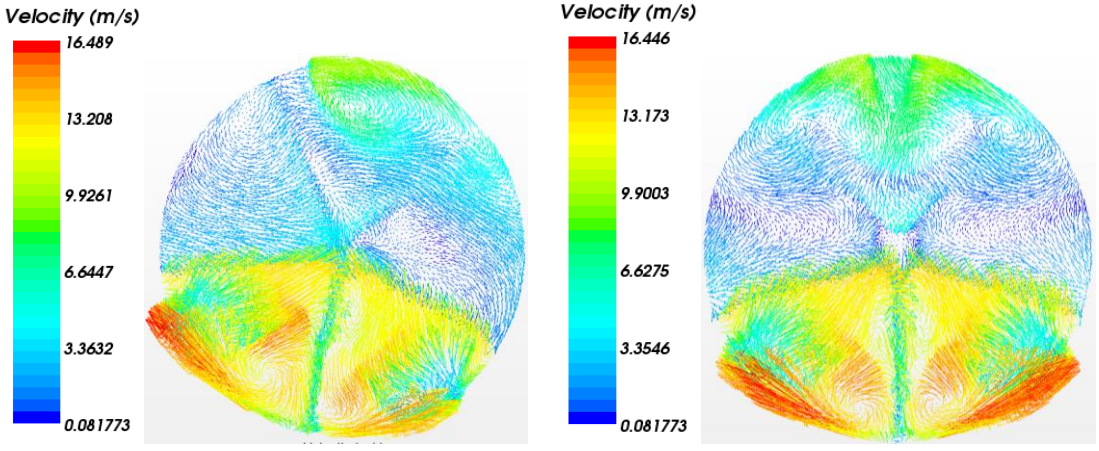

(c) (d)

Figure 2.26: Velocity vector field at the outlet under four wind directions: (a) 0º; (b) 12º; (c) 24º; (d) 36º [15].

The passing flow inside the omni-flow wind energy system is non-uniform in both the velocity and direction, which can affect aerodynamic forces on blades and the performances of a wind turbine. Due to the high velocity region and low velocity region, a blade has to undergo different aerodynamic forces in each revolution. And the change of aerodynamic forces on a rotating blade is frequent. Because of such complex wind conditions, the conventional thin blades of current wind turbines are difficult to work properly. A type of air turbines, named impulse turbine, could have the potential to work under such complex wind conditions. In the wave energy field, impulse turbines have shown good performances under the flow with frequent changes of the wind directions and speeds. Therefore, it is considered to employ the impulse turbine technology in this project.

2.4 Impulse Turbines in Wave Energy Field

Impulse, also called impulse stage, is defined that there is no pressure drop when flow passing through the rotor of a turbine [82]. The impulse turbine is a turbine which has the impulse stage [82]. Typical geometries of impulse turbines can be found in the Pelton wheel and first stages of steam turbines [82]. In wave energy field, the impulse turbine has been one of most widely used turbines for converting air flow energy into mechanical energy. A Wells turbine is another type of turbines used in wave energy field [83]. Compared with Wells turbines, the impulse turbine has high efficiency, low working noise and good starting characteristics [84, 85]. Therefore, technologies about impulse turbines are reviewed in this section. Characteristics of air flow in wave energy, geometry features and performances of impulse turbines in wave energy field are included.

2.4.1 Flow Characteristics

An impulse turbine works inside an Oscillating Water Column (OWC) plant for wave energy conversion [86]. Features of the air flow for an impulse turbine are affected by the OWC plant and waves. The OWC device has a partly submerged structure and opens below the water surface, inside which air is trapped above the water free surface as shown in Figure 2.27 [87]. Oscillating motions of the water surface caused by incident waves can push air to flow through an impulse turbine. The OWC converts wave energy into pneumatic energy in a form of bi-directional air flow [84]. The impulse turbine converts energy from air flow into mechanical energy and drives a generator to produce electricity.

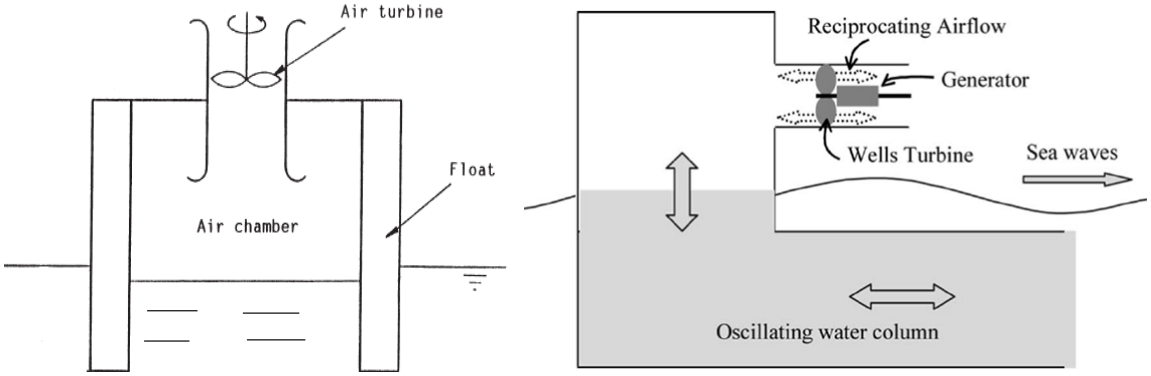

Figure 2.27: Two types of OWCs: (a) vertical type; (b) horizontal type [84, 86].

Due to the motion of water wave, there are much more demanding conditions for an impulse turbine inside an OWC than air turbines in other applications, such as wind turbines [87]. Figure 2.28 shows extremely large variations from wave to wave over a few seconds. Flow properties are varied frequently by the irregular wave motion. Velocity of the air flow oscillates with waves inside an OWC. The air flow direction is reversed several times in few seconds, which is more frequent than changes of nature wind direction.

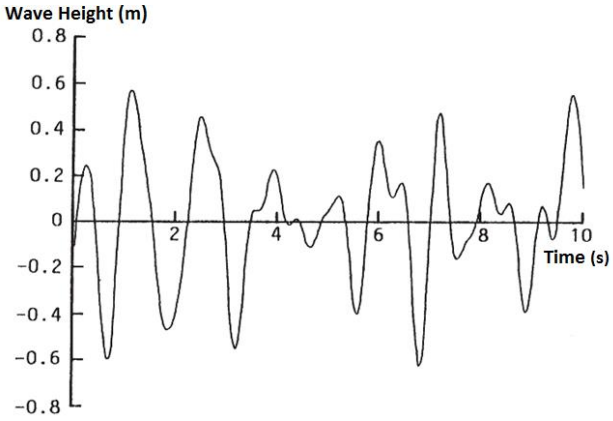

Figure 2.28: Height change of the irregular wave in a short time inside an OWC [84].

There are two similar features between the omni-flow wind energy system and OWC. Firstly, a wind turbine has to work inside the shroud of the omni-flow wind energy system. The shroud may affect the performance of a wind turbine. An impulse turbine also has to operate inside the shroud of an OWC [88]. Secondly, air flow produced by the OWC is greatly unsteady. Blades of an impulse turbine have to suffer the frequently changed flow speed and direction in one revolution. This feature is similar to that a wind turbine working inside the omni-flow system. These two features indicate the possibility to use the impulse turbine technology in a wind turbine for the omni-flow wind energy system.

It should be noted that air flow inside the OWC is a type of internal flow, but wind for a wind turbine is a type of external flow. With the internal flow, there is a high pressure on front of an impulse turbine, which can result in high power output. Hence an impulse turbine inside the OWC can generate more power than a same scale wind turbine. It was reported that an impulse turbine with a rotor diameter of 1.6 m could produce a maximum power ouput of 400 kW at a flow speed of 20 m/s [89]. But the ideal power output for a wind turbine is only 5.7 kW under the same condition.

2.4.2 Geometrical Features of Impulse Turbines

The impulse turbine for wave energy was patented by I.A. Babinsten in 1975 [87]. The rotor of the impulse turbine is basically identical to the rotor of an axial-flow impulse type of signal-stage steam turbines [87]. 3D view of a classic impulse turbine is shown in Figure 2.29. In order to suit the bi-directional air flow in an OWC, blades of impulse turbines use symmetry geometry. In order to optimise the approaching flow, guide vanes are installed in front of blades. Because air flow is bi-directional in an OWC, guide vanes are placed in both upstream and downstream of the rotor. Impulse turbines with fixed guide vanes (IFGVs) and impulse turbines with self-pith-controlled guide vanes (ISGVs) are two major types as shown in Figure 2.30. Guide vanes of IFGVs are fixed with the chamber walls of OWCs. The ISGVs use the same rotors as the IFGVs, but ISGVs have self-pith-controlled guide vanes to suit the change of flow direction [84]. It should be noted that the ISGVs and IFGVs are designed to suit the bi-directional flow condition.

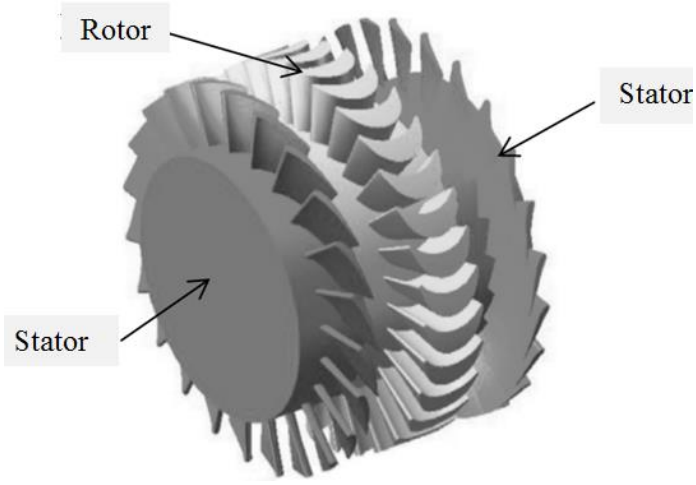

Figure 2.29: 3D view of an impulse turbine [90].

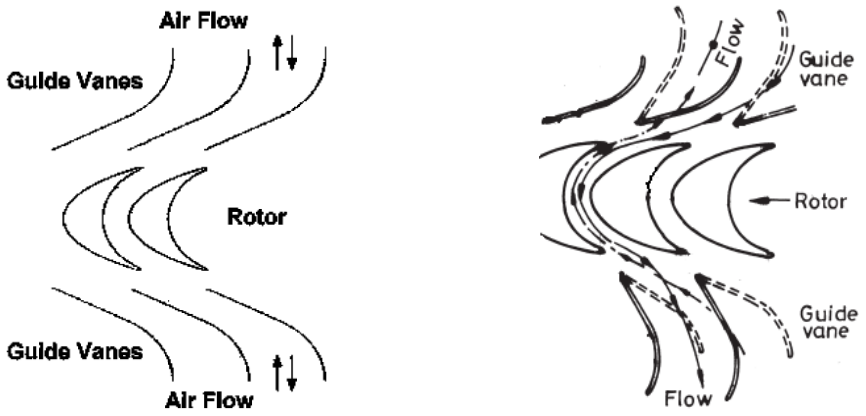

(a) (b)

Figure 2.30: Schematics of two types of impulse turbines: (a) IFGV; (b) ISGV [84].

There are two types of guide vane profiles: aerofoil and plate, as shown in Figure 2.31. Efficiency of an impulse turbine with the aerofoil guide vanes is very close to that with the plate guide vanes [84]. Considered the manufacturing cost, the plate guide vanes have been widely used. Due to geometrical features of guide vanes, there is a nozzle effect on the passing flow to increase the passing flow speed [84].

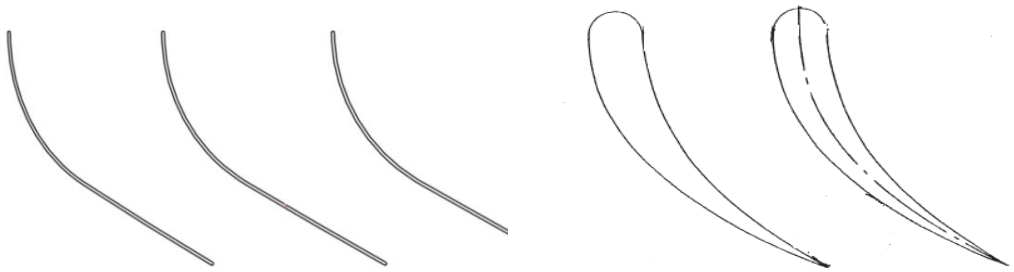

(a) (b)

Figure 2.31: Two profiles of guide vanes: (a) plate; (b) aerofoil [84].

Figure 2.32 shows two typical blade profiles of impulse turbines. These two types of blade aerofoils are both symmetric about the centre axis. The simple profile consists of two circular arcs at mid-chord portion as shown in Figure 2.32(a). In Figure 2.32(b) the elliptic one has a rounded shape [84]. A comparison about mean efficiency of both types of blade aerofoils shows that the elliptic blade profile is superior to the simple one [84].

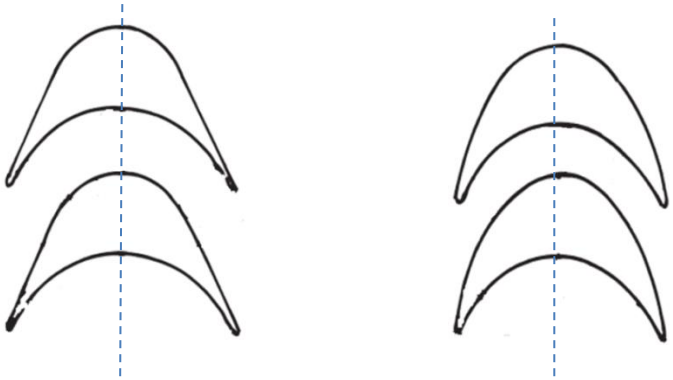

(a) (b)

Figure 2.32: Two blade profiles: (a) simple; (b) elliptic.

Other key geometrical parameters of an impulse turbine include the hub-to-tip ratio and the tip clearance. The hub-to-tip ratio, which is defined as a dimensionless ratio between the hub diameter and rotor diameter, is used to represent the hub size [84]. The hub-to-tip ratio of 0.7 was firstly used in impulse turbines [84, 91]. Then the hub-to-tip ratio of 0.6 was suggested by Thakker *et al.* [92]. Tip clearance is the gap between the blade tip and the chamber inner surface of an OWC. The tip clearance is set for easy installation and maintenance of an impulse turbine inside an OWC. Thakker *et al.* [88] investigated influences of the tip clearance on efficiency of an impulse turbine. Their results showed that the impulse turbine with a tip clearance that takes 1% of the rotor radius performed the similar efficiency to that without tip clearance. Additionally, the tip clearance of 1% can reduce the difficulty in installation of the impulse turbine inside an OWC.

Maeda *et al.* [93] presented an unidirectional impulse turbine which can work under an unidirectional flow condition. The unidirectional impulse turbine has the asymmetrical blade geometry as shown in Figure 2.33(a). It can be seen that the leading edge of the aerofoil is optimised to suit one fixed flow direction, when compared with the classic impulse turbine blade. Because the blade aerofoil is asymmetrical, only upstream guide vanes are needed as shown in Figure 2.33(b). A wave energy system with two unidirectional impulse turbines has

been presented by Jayashankar *et al.* [94, 95]. It should be noted that the unidirectional impulse turbine is designed only for the unidirectional flow, which is the same as a wind turbine. Therefore, it provides more possibility to employ the impulse turbine technology in this omni-flow wind energy system.

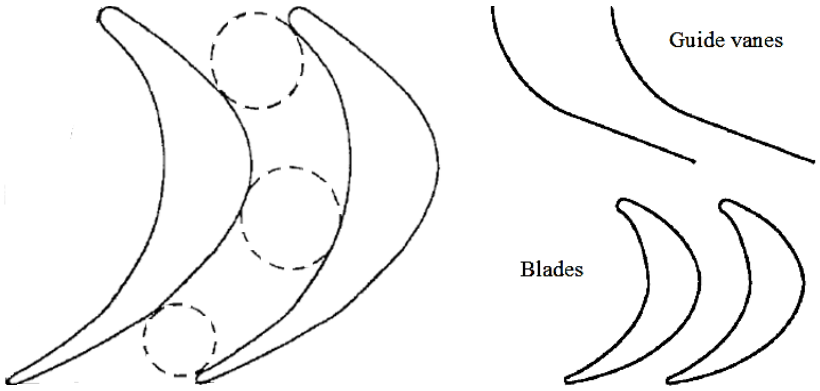

(a) (b)

Figure 2.33: Unidirectional impulse turbine: (a) asymmetric blade aerofoil; (b) upstream plate guide vanes and blades [93].

It should be noted that because there are differences about flow conditions between impulse turbines and wind turbines, the recommended geometrical parameters for an impulse turbine may not be optimal for a wind turbine and need to be investigated.

2.4.3 Performances of Impulse Turbines

Efficiency is the most important feature of an impulse turbine in the wave energy field. Efficiency of different impulse turbines is compared in Figure 2.34. It is clear that the unidirectional impulse turbine has the highest efficiency. Self-pitching guide vanes can improve flow conditions so the ISGVs have the higher efficiency than the IFGVs. But the ISGVs require extra machines for self-pith-controlled guide vanes, which results in higher cost in manufacturing and maintenance. It should be noted that efficiency of an impulse

turbine cannot be compared directly with power coefficient of a wind turbine since the efficiency definition of an impulse turbine is different from that of a wind turbine.

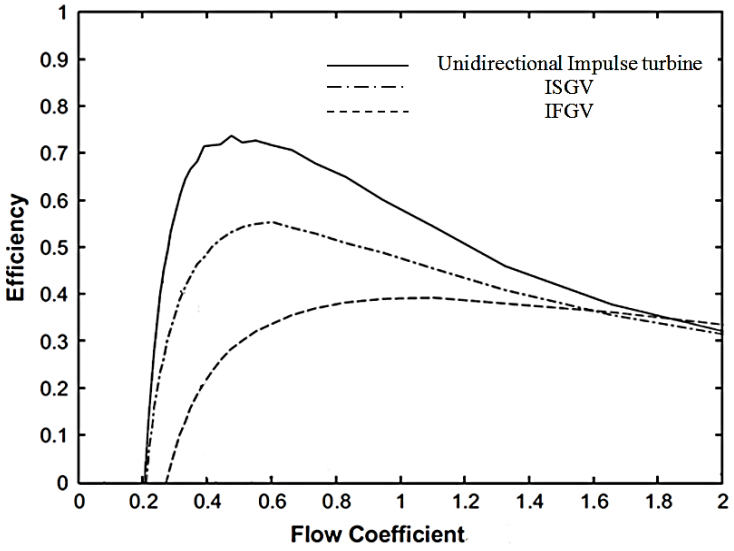

Figure 2.34: Efficiency comparison of three impulse turbines [94].

2.5 Summary

In this chapter, a critical review of existing wind turbines has been carried out. Wind characteristics, requirements from the urban environment and current urban wind turbines have been discussed. The literature review shows that an omni-flow wind energy system has the potential to be used in urban areas, but the non-uniform flow condition is difficult for conventional wind turbines. Based upon the literature review, an impulse turbine has the potential to work under the complex wind conditions caused by the omni-flow wind energy system. Therefore, this project proposes a new wind turbine configuration based upon the impulse turbine technology.

Chapter 3 Methods for Aerodynamic Investigation of Wind Turbines

Several methods have been employed to investigate the aerodynamics of a wind turbine, such as blade element momentum (BEM) theory, computational fluid dynamics (CFD) simulation and wind tunnel testing. BEM method can estimate aerodynamic performances of a wind turbine by lift coefficient, drag coefficient and other terms. However, BEM method is not suitable for the proposed wind turbine. Because the proposed wind turbine has much more blades than common wind turbines, the interferences among blades are unavoidable and complex. Another reason is that the upstream guide vanes of the proposed wind turbine have influences on the flow aerodynamics, which is difficult to be analysed by BEM method. Therefore, the proposed wind turbine is not studied by the BEM method in this project. In this chapter, two methods for aerodynamic analysis of wind turbines, CFD simulation and wind tunnel testing, are reviewed.

3.1 Computational Fluid Dynamics for Investigation of Wind Turbines

With the development of computing power, CFD method has entered into wide applications such as aircrafts, vehicles and turbomachinery. Generally speaking, CFD simulation can reduce a period of time and cost, when compared with experiments. Recently, CFD method has been one of major methods in the aerodynamic investigation of wind turbines. In this section, the employment of CFD method for investigation of wind turbines is reviewed.

3.1.1 Governing Equations

Governing equations consist of the continuity equation, momentum equation and energy equation. Continuity equation represents the physical principle that mass is conserved. Momentum equation is the resulting equation of Newton’s second law. Energy equation

represents that energy is conserved. Energy equation can be ignored in aerodynamic investigations of wind turbines since the temperature change is not always considered. Continuity equation and momentum equation for a compressible Newtonian fluid are shown as follows [96]:

Continuity equation

$$\frac{\partial \rho}{\partial t} + div\left(\rho \vec{U}\right) = 0 \tag{3.1}$$

where ρ is fluid density, t is time and $\vec{U}$ is velocity vector.

Momentum equation

$$\frac{\partial(\rho u)}{\partial \mathrm{t}} + \mathrm{div}\left(\rho u \vec{U}\right) = -\frac{\partial p}{\partial x} + \mathrm{div}(\mu\ \mathrm{grad}\ u) + S_{Mx} \tag{3.2}$$

$$\frac{\partial(\rho v)}{\partial \mathrm{t}} + \mathrm{div}\left(\rho v \vec{U}\right) = -\frac{\partial p}{\partial y} + \mathrm{div}(\mu\ \mathrm{grad}\ v) + S_{My} \tag{3.3}$$

$$\frac{\partial(\rho w)}{\partial \mathrm{t}} + \mathrm{div}\left(\rho w \vec{U}\right) = -\frac{\partial p}{\partial z} + \mathrm{div}(\mu\ \mathrm{grad}\ w) + S_{Mz} \tag{3.4}$$

where u, v and w are components of velocity $\vec{U}$ in x-axis, y-axis and z-axis, μ is dynamic viscosity, p is the pressure on a fluid element, S_{Mx}, S_{My} and S_{Mz} are momentum source terms for the viscous stress on a fluid element.

Governing equations need be transferred into discrete counterparts for numerical evaluation and implementation in calculation. There are three major discretization techniques: finite difference method, finite volume method and finite element method [97]. Finite difference method is easy to formulate and suitable for simple geometries and structured meshes [98]. Finite volume method is appropriate for complex geometries and unstructured meshes [98]. Solution with finite volume method needs less time than that with finite element method [97]. Finite volume method has been popularly used in CFD simulations of wind turbines [17]. The simulations in this project are also based on the finite volume method.

3.1.2 Mesh Strategies for Wind Turbines

The quality of meshing has significant influences on the rate of convergence, solving time and solution accuracy. There are two major types of cells in meshing: structured cell and unstructured cell. The structured cell is simpler than the unstructured cell. A disadvantage of the structured cell is that it is only suitable for simple geometries and primary for finite difference method, and the cell distribution is difficult to control [97, 98]. The unstructured cell is more suitable for complex geometries and is adapted to the finite volume method [97]. The 2D cell shape is always either triangular or quadrilateral. The 3D cell shape is always tetrahedral, hexahedral or polyhedral. Polyhedral cells used in this project are shown in Figure 3.1.

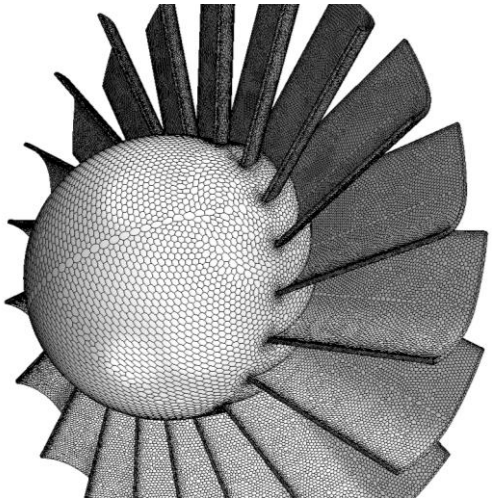

Figure 3.1: Polyhedral cells on the proposed wind turbine model in this project.

Unstructured cells are mainly employed on the blade meshing because they are suitable for the complex profiles of blades. Lanzafame *et al.* [99] used a large amount of tetrahedral cells for modelling a two-blade HAWT, and then replaced the tetrahedral cells by polyhedral cells in order to reduce the cell number and improve accuracy. Thumthae *et al.* [100] employed a hybrid mesh strategy including rectangular cells for the region near blade and triangular cells

for the reset region. They found that the numerical results were quite close to experimental data.

For a 2D straight-blade Darrieus wind turbine model, Danao *et al.* [101] used structured O-type cells as shown in Figure 3.2. They found that the O-type cell was better than the conventional C-type cell since the O-type cell was good at predicting wakes on the blade. For a similar Darrieus wind turbine model, Almohammadi *et al.* [102] employed the structured quadrilateral cells near the blade region and the unstructured cells in the region far from the blade in order to balance the computer source and accuracy.

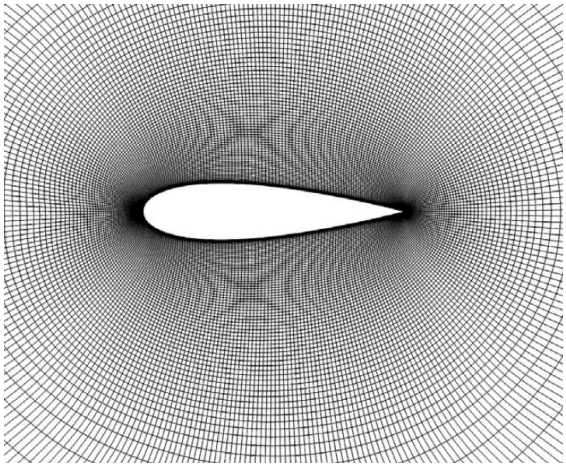

Figure 3.2: O-type cells for a blade aerofoil [101].

For an impulse turbine, Thakker *et al.* [103] used two mesh strategies: the hybrid unstructured mesh strategy including hexahedral, tetrahedral and pyramidal cells as shown in Figure 3.3, and the hexahedral structured mesh strategy. Numerical results produced by two mesh strategies were both close to experimental results. They found that the hybrid unstructured cells had the better mesh quality and somewhat were easier to be created than the hexahedral cells because the hybrid cells were more suitable for complex profiles than the hexahedral cells [103].

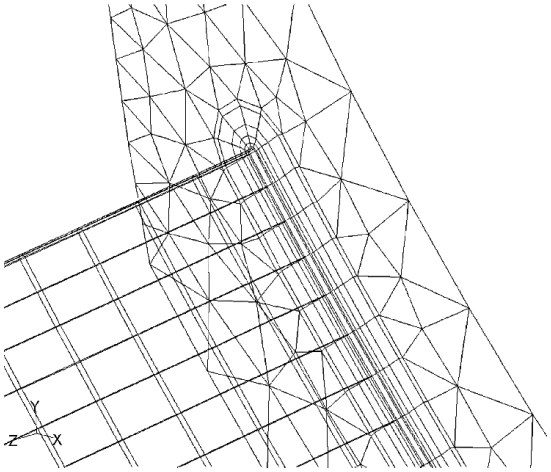

Figure 3.3: The hybrid mesh strategy for an impulse turbine [103].

3.1.3 Turbulence Models Used for Investigation of Wind Turbines

Turbulent flow is quite difficult to be solved because turbulent flow is highly unsteady and contains a great deal of vorticity [97]. Recently, turbulent flow can be solved by the solution with Reynolds-averaged Navier-Stokes (RANS) equations, large eddy simulations (LES) and direct numerical simulations (DNS) [98, 104]. The solution with RANS equations can provide results with acceptable levels of accuracy for many engineering purposes with less computing cost, when compared with LES and DNS [104-107]. The work in this project is based on the solution with RANS equations.

RANS equations for compressible flow are given as follows [96]:

Continuity equation:

$$\frac{\partial \bar{\rho}}{\partial t} + \mathrm{div}(\rho \bar{U}) = 0 \tag{3.5}$$

where $\bar{U}$ is mean velocity vector, $\bar{\rho}$ is mean fluid density and *t* is time.

Reynolds equations:

$$\frac{\partial(\bar{\rho}\bar{u})}{\partial \mathrm{t}} + \mathrm{div}(\bar{\rho}\bar{u}\bar{U}) = -\frac{\partial p}{\partial x} + \mathrm{div}(\mu\ \mathrm{grad}\ \bar{u}) + \left[-\frac{\partial(\bar{\rho}\overline{u'^2})}{\partial x} - \frac{\partial(\bar{\rho}\overline{u'v'})}{\partial y} - \frac{\partial(\bar{\rho}\overline{u'w'})}{\partial z}\right] + S_{Mx} \tag{3.6}$$

$$\frac{\partial(\bar{\rho}\bar{v})}{\partial \mathrm{t}} + \mathrm{div}(\bar{\rho}\bar{v}\bar{U}) = -\frac{\partial p}{\partial y} + \mathrm{div}(\mu\ \mathrm{grad}\ \bar{v}) + \left[-\frac{\partial(\bar{\rho}\overline{u'v'})}{\partial x} - \frac{\partial(\bar{\rho}\overline{v'^2})}{\partial y} - \frac{\partial(\bar{\rho}\overline{v'w'})}{\partial z}\right] + S_{My} \tag{3.7}$$

$$\frac{\partial(\bar{\rho}\bar{w})}{\partial \mathrm{t}} + \mathrm{div}(\bar{\rho}\bar{w}\bar{U}) = -\frac{\partial p}{\partial z} + \mathrm{div}(\mu\ \mathrm{grad}\ \bar{w}) + \left[-\frac{\partial(\bar{\rho}\overline{u'w'})}{\partial x} - \frac{\partial(\bar{\rho}\overline{v'w'})}{\partial y} - \frac{\partial(\bar{\rho}\overline{w'^2})}{\partial z}\right] + S_{Mz} \tag{3.8}$$

where $\bar{u}$, $\bar{v}$ and $\bar{w}$ are mean velocity components of u, v and w. u', v', and w' are fluctuating velocity components of u, v and w. S_{Mx}, S_{My} and S_{Mz} are momentum source terms for the viscous stress on a fluid element.

Several turbulence models have been used in simulations of wind turbines, such as Spalart–Allmaras model, two equation models (Algebraic stress model, k-ε and k-ω turbulence models) and Reynolds stress model. Spalart–Allmaras model can provide economical computations, but Benjanirat *et al*. [108] reported that Spalart–Allmaras model was poor on predictions of aerodynamic performances of wind turbines, when compared with two equation models. Reynolds stress model has a potential for being one of the most general turbulence models, but the model needs more computing cost than two equation models [109]. Algebraic stress model is an approach combining the generality of Reynolds stress model with the economy of k-ε models, but it has not been widely validated and used on wind turbines [96, 110]. Compared with other turbulence models, the families of k-ε and k-ω turbulence models are more popular in investigations of wind turbines with acceptable computer source requirements [17]. The employment of k-ε and k-ω turbulence models for aerodynamic analyses of wind turbines is reviewed in this subsection.

Launder and Spalding [111] have developed the standard k-ε turbulence model that consists of two transport equations for the turbulent kinetic energy, k and its dissipation rate, ε. The

standard k-ε turbulence model has been widely used but this model has some limitations related to low Reynolds number and flow separation [112]. Wolfe *et al*. [113] used the standard k-ε turbulence model to study a blade aerofoil and found that the numerical results agreed well with experimental data at low angles of attack. The standard k-ε turbulence model can predict performances of a HAWT with acceptable levels of accuracy [108]. Aresti *et al*. [114] analysed the flow separation and vortex behind a VAWT by the standard k-ε turbulence model. Thakker *et al*. [103, 115, 116] employed the standard k-ε model to study impulse turbines and found that the predicted efficiency agreed well with experimental data.

The realisable k-ε model contains a new transport equation for the turbulent dissipation rate and a new eddy viscosity formulation based on the realisability constraints, when compared with the standard k-ε model [117]. Because the eddy viscosity formulation includes a rotation rate, the realisable k-ε model is possible to yield a better performance than the standard k-ε model when the flow involves separation and rotation [117, 118]. Raciti Castelli *et al*. [119, 120] reported that the realisable k-ε model successfully predicted most flow features in a study of a Darrieus wind turbine. Dragomirescu [74] employed both the realisable k-ε model and the SST (shear stress transport) k-ω model for a wind turbine and found that only the realisable k-ε model assured convergence. Mohamed [121] used the realisable k-ε model to study the power output performance of a Darrieus wind turbine and found that the numerical results matched well with experimental data. Abohela *et al*. [37] suggested that the realisable k-ε model was preferred in simulations of flow around buildings for positioning wind turbines.

The standard k-ω model is prominent one of two-equation turbulence models. This model is characterized by the turbulent kinetic energy k and the frequency, $\omega = \frac{k}{\varepsilon}$. Wilcox [122]

pointed that the standard k-ω model could be integrated into the flow near walls without wall-damping functions. But Menter [123] pointed out that the standard k-ω model could fail for the flow with pressure induced separation. Yang *et al*. [124] studied a blade aerofoil by the standard k-ω model and found that the computational results like pressure coefficients had good agreement with the experimental ones. In a study of a VAWT, results from the standard k-ω model were closer to the experimental data than those from the standard k-ε model [125]. In studies of impulse turbines, Thakker *et al*. [103, 115] found that the numerical results from the standard k-ω model had a similar trend to the experimental results although the numerical approach over predicted results at high flow speeds.

Menter [126] found that the near-wall performance of the standard k - ω model was unsatisfactory for boundary layers with adverse pressure gradients and proposed a SST (shear stress transport) k-ω turbulence model. The SST k-ω model uses a transformation of the k-ε model into the k-ω model in the near wall region and keeps the standard k-ε model in the fully turbulent region far from the wall. The SST k-ω model has a good wall treatment and avoids shortcomings of the k-ε model and the standard k-ω model [110, 126]. Le Pape *et al*. [127] studied a HAWT by the standard k-ω turbulence model and SST k-ω turbulence model. They found that the SST k-ω turbulence model had better performances on prediction of the stall angle than the standard k-ω turbulence model. Chong *et al*. [76] investigated a Darrieus wind turbine with guide vanes by the SST k-ω model and found that the trend of numerical results was close to that of experimental data.

3.1.4 Applications of CFD Method

The current employment of CFD method in aerodynamic analyses of wind turbines is reviewed in this subsection. CFD method has been used to optimise the blade aerofoil design.

Yang *et al.* [128] and Wolfe *et al.* [129] both used CFD method to study aerodynamic characteristics of NERL aerofoils of wind turbine blades. Fuglsang *et al.* [130] and Bertagnolio *et al.* [131] analysed performances of the Risø airfoil family by CFD simulations.

CFD method has been employed in 3D aerodynamic analyses of wind turbines. Duque *et al.* [132] and Sørensen *et al.* [133] simulated the flow around 3D HAWT models and predicted power output. Since then, the CFD method has been widely used for various wind turbines. Howell *et al.* [27] presented a 3D simulation of a straight-blade Darrieus wind turbine. Features of other types of wind turbines were also studied by the CFD method before experiments [70, 74, 76, 81]. Moreover, the tower and the nacelle of a wind turbine have been analysed by simulations. Li *et al.* [134] simulated a NREL Phase VI wind turbine model that included blades, a nacelle and a tower. Lin *et al.* [135] studied the interference between the tower and blades. Because the rotor axis of a HAWT is parallel to wind direction, it can be regarded that the wind features are unchangeable in one revolution. Thus steady solutions are always used for HAWTs [99]. However, the rotor axis of a VAWT is perpendicular to wind direction, wind features depend on the position of blades in each revolution. Therefore, unsteady solutions are always employed for VAWTs [114].

The predicted aerodynamic forces by CFD method have been used in structural analyses of blade structures [136, 137]. Baxevanou *et al.* [138] presented a numerical model combining a Navier-Stokes CFD solver with an elastic model to study the aeroelastic features of wind turbine blades.

Using the CFD method in studies of wind turbines has shown advantages over experimental tests in time and costs. Present aerodynamic research of wind turbines has indicated that CFD approach can provide results with acceptable levels of accuracy. Recently, the CFD method

has been one of major approaches in aerodynamic investigations of wind turbines. Many studies of wind turbines have used commercial CFD software packages [139-142]. In this project the CFD method has been employed to study aerodynamic performances of the proposed wind turbine.

3.2 Wind Tunnel Testing

A wind tunnel is used to measure the characteristics of the air flow around an object positioned in a test section, such as flow velocity, flow pressure, aerodynamic force and moment. A wind tunnel consists of a flow passage, a test section, a fan system and a balance system. A wind tunnel produces air flow inside the test section with the aid of a powerful fan. The flow velocity in a wind tunnel is controlled by adjusting rotational speeds of the fan. Aerodynamic forces and moments on an object are measured by a balance system. Generally speaking, there are two types of wind tunnels: the open return wind tunnel and the closed return wind tunnel. There are also two types of test sections: the open test section and the closed test section.

Wind tunnel testing is one of major methods in aerodynamic research of wind turbines. A classical measurement system includes a torque transducer and a rotational speed sensor. Figure 3.4 shows a measure system for testing a HAWT. In tests, both torque and rotational speeds of a tested wind turbine are obtained from the sensor. As shown in Figure 3.4, a brake positioned behind the sensor applies loads on the shaft to control the rotational speed of the turbine.

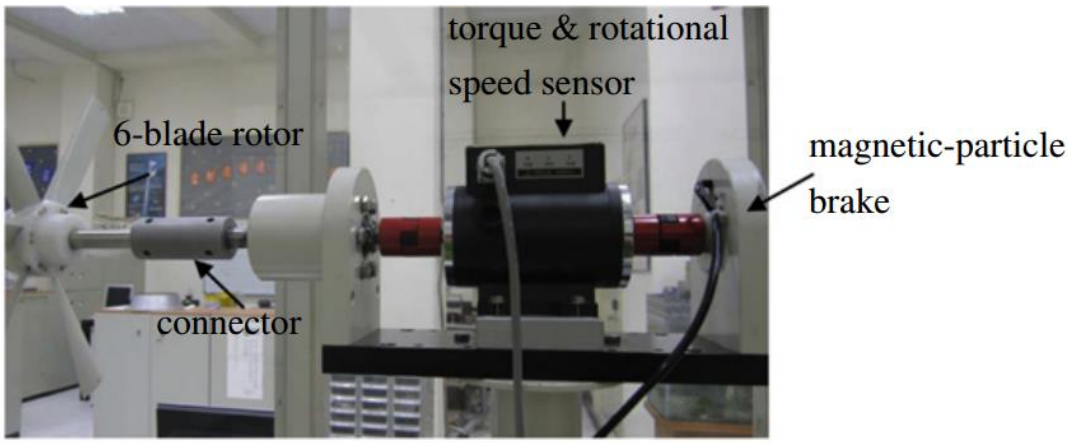

Figure 3.4: Measure system in wind tunnel testing [143].

In wind tunnel testing, the torque, rotational speed and power output of a wind turbine over a range of wind velocities can be measured. Figure 3.5 shows various wind turbines in wind tunnel tests. Kishore *et al.* [52] tested a small HAWT inside an open test section. Distributions of the power coefficient and torque coefficient under various wind velocities were achieved. Wind tunnel testing has also been used to investigate VAWTs. Danao *et al.* [144] studied a straight-blade Darrieus wind turbine inside a closed test section. They prepared an unsteady wind condition by controlling a shutter drive mechanism inside the wind tunnel. The power output and acceleration of rotational speeds of the VAWT under the unsteady condition were tested. Burlando *et al.* [145] employed a closed return wind tunnel with a closed test section to study the flow field around a Savonius wind turbine.

Wind tunnel testing has been used to validate the numerical approach by comparing experimental data with numerical results. Aresti *et al.* [114] studied performances of a wind turbine by different turbulent models and then compared the modelling results with data from wind tunnel testing. Rolland *et al.* [146] employed smoke as a flow visualisation method in wind tunnel testing to prove a prediction about a turbulent vortex pattern found in simulations.

Ahmed *et al.* [70] presented a shroud to accelerate the flow speed for a wind turbine and validated its performances in an open return wind tunnel.

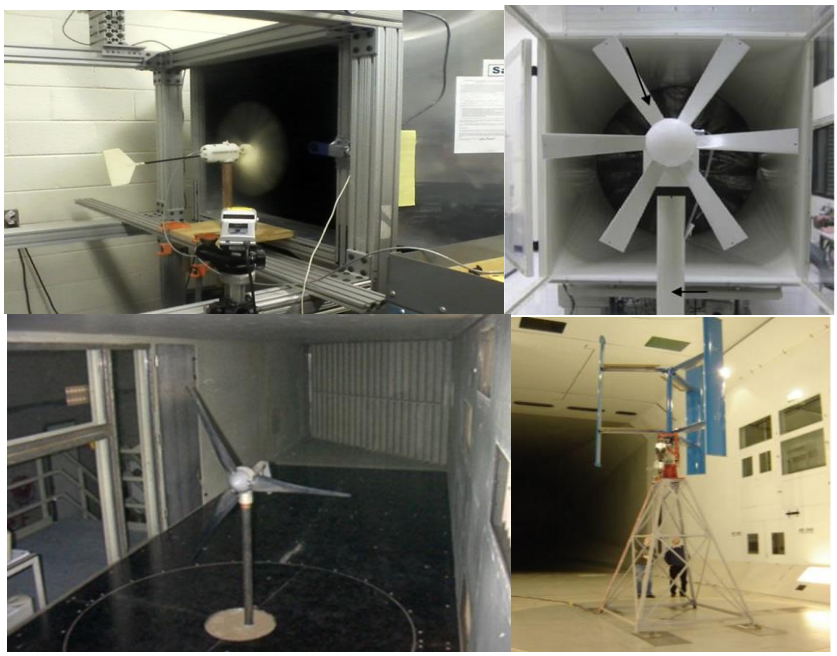

Figure 3.5: Wind turbines in wind tunnel tests [47, 143, 147].

Solid blockage is a common phenomenon existed in wind tunnel testing. Solid blockage is caused by a reduction in the cross area of the test section, when placing an object inside the wind tunnel. Due to the solid blockage, velocity of the flow inside the test section is increased, when compared with the free stream. The magnitude of solid blockage can be represented by a ratio between the front area of the object and the cross area of the test section. Solid blockage exists both in a closed test section and an open test section. A wind tunnel with a closed test section is more sensitive to solid blockage than that with an open test section, but the influence of solid blockage on the flow speed can be corrected [148]. Barlow *et al.* [148] suggested a blockage correction method for an unusual shape in a tunnel. The correction factor, C_B, can be expressed as:

$$C_B = \frac{1}{4}\frac{model\ frontal\ area}{test\ section\ area} \tag{3.9}$$

The corrected flow speed, $U_{\text{corrected}}$, can be given by

$$U_{corrected} = (1 + C_B) \cdot U_{measured} \tag{3.10}$$

A closed return wind tunnel has been used in this project since the quality of flow in a closed return wind tunnel is easy to be controlled [149]. A measurement system in wind tunnel testing can record the power output from the proposed wind turbine under various wind velocities. Meanwhile, the wind tunnel testing can be used to validate a numerical approach used in this project.

3.3 Summary

The CFD method and the wind tunnel testing for aerodynamic investigations of wind turbines have been reviewed in this chapter. BEM method is not considered to be used in this project because the proposed wind turbine has a large number of blades and a group of upstream guide vanes. Applications of the CFD method and the wind tunnel testing on studies of wind turbines have been discussed. From the literature review, both the CFD method and the wind tunnel testing can be used to study the proposed wind turbine. Considering the low cost, the CFD method is used to analyse flow characteristics near the blades and aerodynamic performances of the wind turbine in this project. The wind tunnel testing is used to validate the CFD modelling by comparing computational results with experimental data.

Chapter 4 Proposed Configuration of a Novel Wind Turbine

As discussed in Section 2.3, both velocity and direction of the flow are non-uniform inside the omni-flow wind turbine energy system and conventional wind turbines are difficult to suit. Therefore, a new concept of a wind turbine is needed for the system. This chapter introduces the configuration of a novel wind turbine based on the impulse turbines technology.

4.1 Introduction

This project proposes a new wind turbine configuration for an omni-flow wind energy system in urban areas. In Sections 2.2 and 2.3, the requirements of urban wind turbines and the flow features inside the omni-flow wind energy system have been summarised. The novel wind turbine configuration is based on the impulse turbine technology. The impulse turbine technology reviewed in Section 2.4 shows the potential to operate well under the non-uniform flow condition inside the omni-flow wind energy system. As reviewed in Section 2.4, the impulse turbine technology includes several characters as follows [84, 93]:

- Blades of impulse turbine utilise specific aerofoils as shown in Figures 2.32 - 2.33.
- Guide vanes placed ahead of blades are needed.
- The rotor has a large number of blades.
- The rotor hub has a significantly large size.

4.2 Geometry of a Novel Wind Turbine

The review from Section 2.4 shows that the unidirectional impulse turbine has good performances [94] therefore the proposed wind turbine uses a type of asymmetric blade profiles and only one group of upstream guide vanes. The wind turbine consists of two components: a stator and a rotor as shown in Figure 4.1(a). The diameter of the proposed wind turbine is 300 mm. This diameter is chosen due to the dimensions of the omni-flow

wind energy system presented by Zhang [15]. Considering the internal installation space of the system, the wind turbine diameter is 300 mm. Both the stator and the rotor have an identical hub diameter of 135 mm. Figure 4.1(b) shows the proposed wind turbine inside a cylindrical chamber. Guide vanes are fixed with the chamber, thus the stator is stationary when the turbine operating. Guide vanes can change the flow direction and speed. When air flow passing blades, the generated torque drives the rotor to rotate so that wind energy is converted into mechanical energy. Figure 4.1(b) also shows that there is a clearance of 2 mm between blades and the chamber wall. This small clearance has a negligible influence on the performance of an impulse turbine [88].

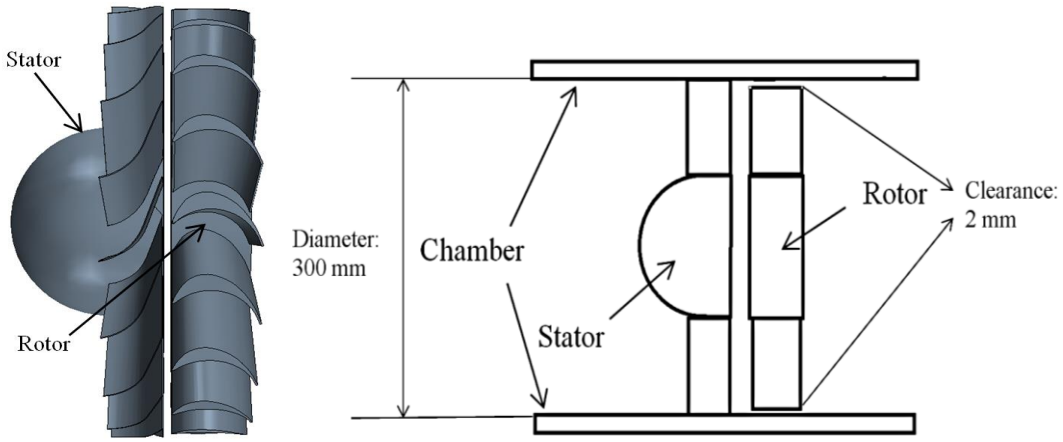

(a) (b)

Figure 4.1: The proposed wind turbine: (a) 3D view; (b) schematic view of the wind turbine inside a chamber.

The stator has 20 guide vanes and the profile of one guide vane is shown in Figure 4.2. The guide vane has a simple plate geometry that includes an arc front and a straight rear as shown in Figure 4.2(a). Such a plate geometry has been widely used in impulse turbines [84]. The straight rear of the guide vane has a setting angle of 20^{o} that is an optimal setting angle for guide vanes of an impulse turbine [93]. The arc part has a radius of 30.02 mm and the straight

part has a length of 31.52 mm. Setoguchi *et al.* [84] recommended ratios between the turbine diameter and dimensions of guide vanes for an impulse turbine. Dimensions of the proposed guide vanes are selected based upon the recommended ratios. Technical drawings of the guide vane and the stator hub are given in Appendices A and B.

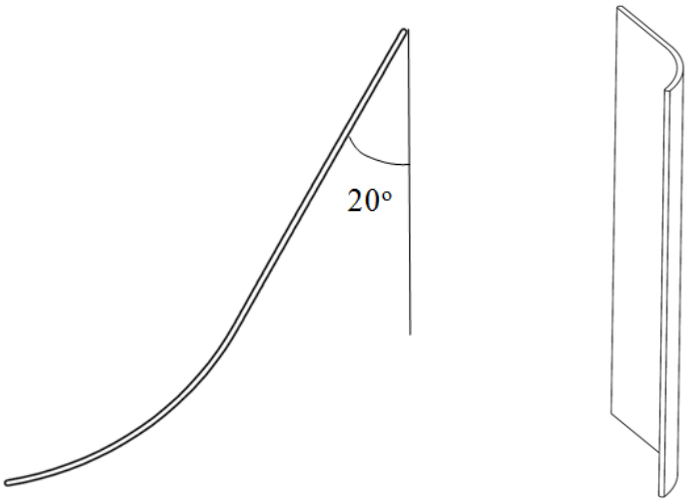

Figure 4.2: Guide vane: (a) section view; (b) 3D view.

Maeda *et al.*[93] suggested that the impulse turbine had good performances when the blade aerofoil was not asymmetric and the aerofoil trailing edge was thinner than the leading edge. This suggestion was considered when the configuration of the wind turbine was proposed. The blade profile is asymmetric as shown in Figure 4.3(a). This aerofoil is utilised on each blade section and the blade is not twisted as shown in Figure 4.3(b). This simple geometry can reduce difficulty and cost of manufacturing. The chord length is 49.51 mm which takes up 33% of the turbine radius. The amount of camber as a percentage of the chord length is 38%. The lengths of chord and camber are chosen due to the dimensional ratios recommended by Setoguchi *et al* [84]. There are 20 blades on the rotor. Technical drawing of

the rotor hub is given in Appendix C. This aerofoil is named as Type 1 aerofoil and its coordinates are listed in Appendix D.

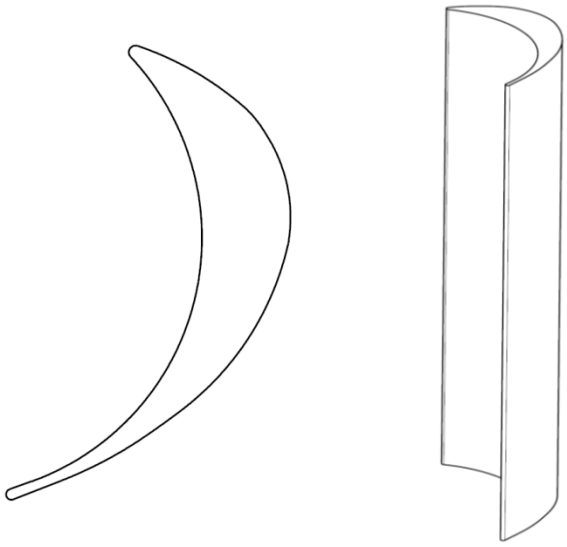

(a) (b)

Figure 4.3: Schematic views of the blade: (a) aerofoil; (b) 3D view.

4.3 Unique Geometrical Features

Compared with existing wind turbines, this novel wind turbine has several unique geometrical features as follows:

(1) Influences of the stator. This wind turbine has an extra stationary component – stator – compared with conventional wind turbines. Air flow passes through the stator firstly and then blades. Employing such a stator with guide vanes is to optimise the properties of the passing flow. It can be expected that the stator has influences on both flow direction and velocity.

(2) Blade number. This wind turbine has a blade number of 20 that is much greater than two or three blades of general wind turbines. Based upon the definition of solidity in Eq. (2.7), this novel wind turbine has a solidity of approximately 1 that is 10 times higher than 0.1 of a general wind turbine [18]. It is reported that the blade number has influences on the

power output and starting capability [57]. The effects of the blade number on aerodynamics of the proposed wind turbine are studied in following chapters.

(3) Aerofoil. The camber of the blade aerofoil takes 44% of the chord length. The percentage camber of this aerofoil is much larger than that 0% - 6% of general blade aerofoils. The ratio between the chord and the blade radius is 0.33 that is also higher than 0.04 - 0.2 of a general blade [18].

(4) Aspect ratio. The aspect ratio is defined as the blade length to the blade chord. The aspect ratio of the proposed wind turbine is approximately 3 that is much smaller than 5 - 10 of a general HAWT [18]. A blade with a smaller aspect ratio has a potential to support more load if an identical material is used.

(5) Large hub diameter. A hub-to-tip ratio, which is a non-dimensional term to represent the hub size, is defined as a ratio between the hub diameter and wind turbine diameter. A conventional wind turbine always has a hub-to-tip ratio of approximately 0.1 that has a tiny influence on the performance of a conventional wind turbine [18]. But this new wind turbine has a large hub-to-tip ratio of 0.45. It is suggested that the hub, as a component of the flow passing passage, can affect the properties of the passing flow.

(6) Working inside a shroud. The conventional wind turbines always work in an open environment. But the proposed wind turbine operates inside a shroud of the omni-flow system that can affect the speed and direction of the passing flow.

4.4 Summary

The configuration of a novel wind turbine for the omni-flow wind energy system is proposed in this chapter. The proposed wind turbine is based on the impulse turbine technology that has not been utilised in the wind turbine field. This novel wind turbine has different geometrical features compared with existing wind turbines, such as the blade profile, the number of blades,

guide vanes and the size of the hub. Aerodynamics of this proposed wind turbine is studied in following chapters.

Chapter 5 Aerodynamic Analysis of the Novel Wind Turbine

Chapter 3 has reviewed features of the CFD simulation and wind tunnel testing. This chapter presents aerodynamic analyses of the novel wind turbine by two methods. The test rig in wind tunnel and the setup of CFD simulation are also presented. The main focus of the chapter is on aerodynamic features of the proposed wind turbine such as power output, torque and starting capability, especially on the effect of the stator on flow characteristics.

5.1 Test Rig in Wind Tunnel Testing

5.1.1 Wind Tunnel and Test Rig

Experimental results obtained from wind tunnel testing have been used to validate numerical approach for the proposed wind turbine. All the wind tunnel tests were carried out in a closed return wind tunnel as shown in Figure 5.1 in the School of Engineering and Technology at the University of Hertfordshire. The quality of air flow inside a closed return wind tunnel is easy to be controlled [149]. The wind tunnel has a closed test section of 1.14 m (width) × 0.84 m (height), with a maximum operational flow velocity of 25 m/s. The flow uniformity is greater than 99% and the turbulence intensity is less than 1%.

Figure 5.1: The closed return wind tunnel used in this project.

In the tests, a prototype of the wind turbine installed on the test rig was positioned at the centre of the test section. Dimensions of the wind turbine have been given in Chapter 4. As shown in Figure 5.2, the prototype has 20 guide vanes and 20 blades. The wind turbine diameter is 300 mm and the hub diameter is 135 mm. Both the stator and the rotor have the same hub diameter. The stator and the rotor were produced by a Rapid Prototyping machine (Stratsys Dimension 3D Printer) with acrylonitrile butadiene styrene (ABS) plastic to have accurate geometries. Blades, guide vanes and hubs were produced separately and then assembled together. This wind turbine prototype was installed inside a 200 mm long cylindrical chamber. Figure 5.2(a) shows the stator inside the cylindrical chamber. The guide vanes were fixed to the chamber wall. Therefore, the stator was stationary when the wind turbine rotated. There was a clearance of 2 mm between the blade tip and chamber wall. This clearance is useful in the safe installation of the rotor inside the chamber. The 2 mm clearance is approximately 1% of the rotor radius, which has a negligible influence on the performance of an impulse turbine [88].

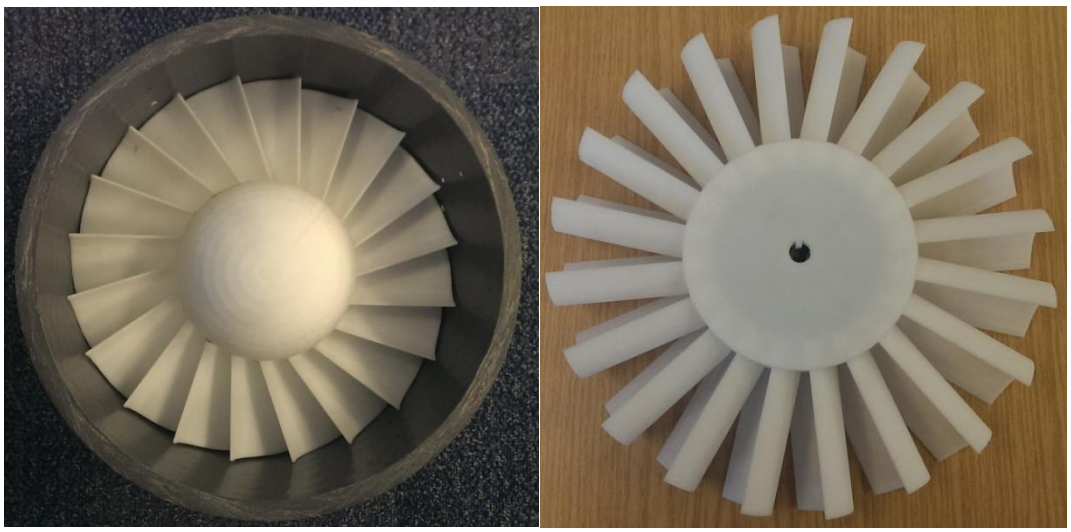

(a) (b)

Figure 5.2: Wind turbine prototype: (a) stator inside a cylindrical chamber; (b) rotor with blades.

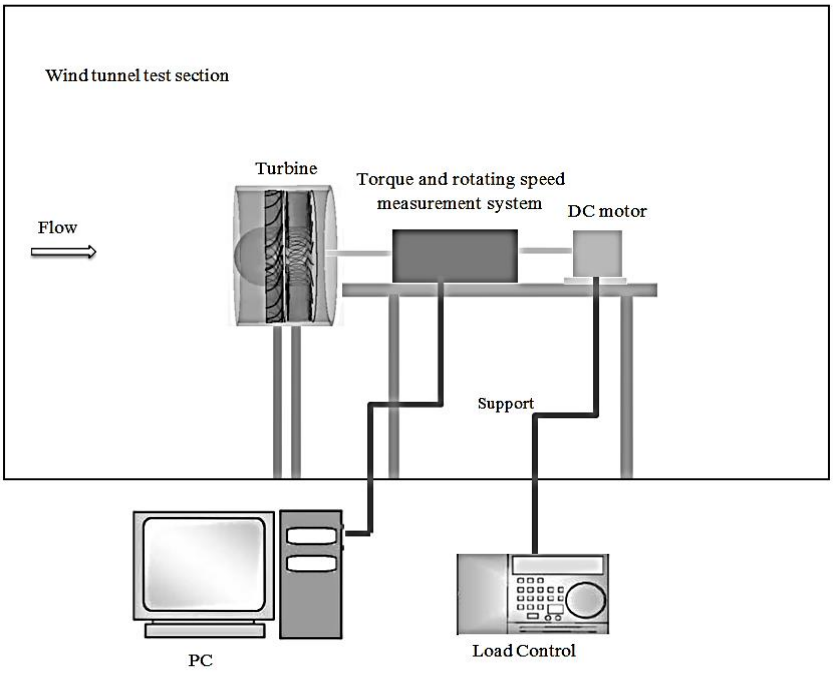

Figure 5.3: Schematic for the measurement system of the wind tunnel testing.

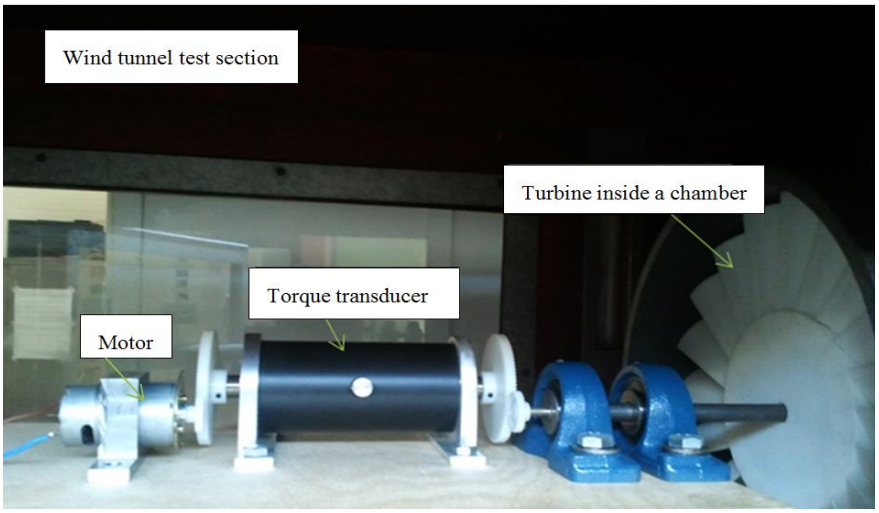

Figure 5.4: Test rig inside the wind tunnel test section.

The test rig was used to measure the torque and rotational speed of the proposed wind turbine. Figure 5.3 shows a schematic view of the measurement system and Figure 5.4 shows the test rig inside the test section. The review about wind tunnel testing in Chapter 3 has shown that this type of test rigs is typical and has been used for various wind turbine evaluations. As

shown in Figure 5.3, this test rig consists of a torque transducer, a DC motor, a power and supports. The torque transducer can measure the torque generated from the wind turbine. The torque transducer (Datum Electronics M420) has a test range from 0 to 10 Nm with an accuracy of 0.1% and maximum rotational speed of 5000 rpm. 100 sample data can be recorded in one second by this transducer. In the tests, data obtained from the transducer were collected by an interface (Datum Electronics, Part No. 400150) and a monitor software package TorqueLog (Datum Electronics, Version 1.8). A DC motor (Crouzet 8286201) applied a braking load on the wind turbine prototype to control rotational speeds. The load was adjusted by varying the current in the DC motor. The current for the DC motor came from a DC Power Supply (ISO-TECH IPS1820D, output current range: 0-20A). Two pairs of spur polyacetal gears (Davall MA08-30/90) were used in the tests. They have the same transmission ratio of 3:1 and the module number of 0.8. One pair was used to connect the wind turbine and the torque transducer to transmit a torque. Another pair was used to connect the torque transducer and the DC motor so that the load from the DC motor could be applied to the wind turbine for controlling the rotational speeds. The shaft of the wind turbine was constrained by house bearings. Both gears and bearings could cause a power loss, which will be discussed in Section 5.1.2.

Flow velocity in the wind tunnel was measured by a Pitot tube and a pressure meter (AIRFLOW-PVM100). The size of the Pitot tube used in this study is very small as shown in Figure 5.5, thus influence on the surrounding air flow can be ignored [15]. This Pitot tube was handheld to measure the flow velocity during the wind tunnel testing.

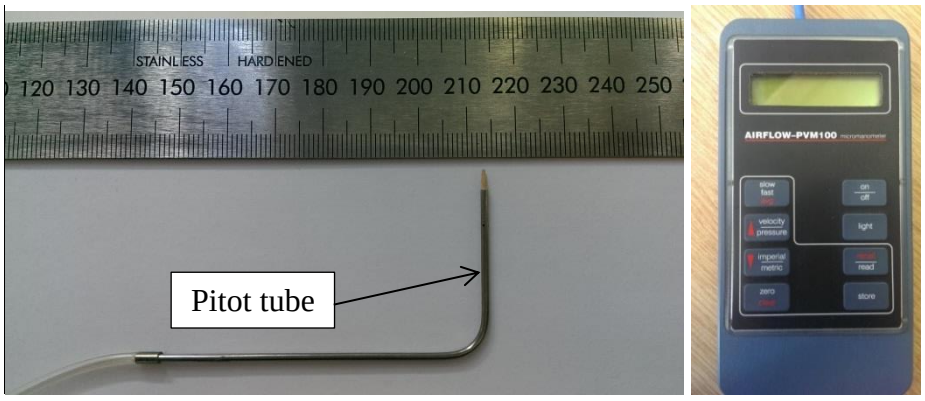

(a) (b)

Figure 5.5: Flow measurement: (a) tiny Pitot tube; (b) pressure meter

5.1.2 Blockage Correction and Error Analysis

As discussed in Chapter 3, when the wind turbine was tested in the closed test section, a correction for blockage effect should be introduced. Based on Eq. (3.9), the correction can be calculated as

$$C_B = \frac{1}{4}\frac{\pi \times 0.162^2 + 0.04}{1.14 \times 0.84} = 0.032$$

where $\pi \times 0.162^2$ m^2 represents the frontal area of the wind turbine and 0.04 m^2 is the frontal area of supports. Therefore, a flow velocity inside the test section can be corrected as

$$U_{corrected} = 1.032 U_{measured} \tag{5.1}$$

The flow velocity inside the wind tunnel test section was calibrated by the tiny Pitot tube. Error analysis of the tiny Pitot tube has been carried out by Zhang [15]. The average error in measuring flow velocity was 0.58%.

In wind tunnel testing, due to the friction between bearings and the shaft, a resistive torque was generated in the house bearing, which caused power loss. The resistive torque was measured before wind tunnel testing. As shown in Figure 5.4, a motor (Crouzet 8286201) with a known power-speed relationship produced an applied power (P_a) at one end of the

shaft. The shaft was supported by the house bearing that was used in wind tunnel testing. The transmitted power (P_t) was tested on another end of the shaft. The power loss can be obtained by comparing the applied power and the transmitted power. The resistive torque, T_r, is calculated by

$$T_r = \frac{P_a - P_t}{\omega} \tag{5.2}$$

where ω is the rotational speed of the rotor. The error (e) is calculated as follows [150]:

$$e = \left|\frac{P_{max} - P_{average}}{P_{average}}\right| \times 100\% \text{ or } e = -\left|\frac{P_{min} - P_{average}}{P_{average}}\right| \times 100\% \tag{5.3}$$

where P_{max} is the power with the maximum resistive torque, P_{min} is the power with the minimum resistive torque , and $P_{average}$ is the power from the wind turbine with the average resistive torque.

The minimum, maximum and average values of the resistive torque and errors are listed in Table 5.1. The power coefficient in Table 5.1 is based on the flow velocity of 8.2 m/s. The average resistive torque caused by the house bearing is in a range from 0.007 Nm to 0.0163 Nm. It can be seen that the maximum error in C_P is $\pm$2% under high rotational speeds and the average error is $\pm$1% over a range of rotational speeds from 0 rpm to 600 rpm.

Table 5.1: Errors caused by the house bearing on power coefficient.

Rotational speed, rpm	Min T_r	Max T_r	Average T_r	Error in C_P
0-150	0.0056	0.0084	0.007	$\pm$0.5%
150-300	0.009	0.0118	0.01	$\pm$0.8%
300-450	0.013	0.0147	0.0138	$\pm$0.9%
450-600	0.0155	0.017	0.0163	$\pm$2%
Average				$\pm$1%

In wind tunnel testing, the test flow velocity is in a range of 3.5 m/s - 8.2 m/s that represents a typical range of wind velocities in urban areas. With an increase of the flow velocity from 3.5 m/s to 8.2 m/s, the growth rate of the resistive torque is lower than the growth rate of the produced torque. Hence, the error of resistive torque decreases with the increase of the flow velocity. As shown in Table 5.2, the average error decreases from $\pm$11.36% to $\pm$1% when the wind speed increases from 3.5 m/s to 8.2 m/s. The error at the flow velocity of 8.2 m/s is the minimum one in Table 5.2, therefore the velocity of 8.2 m/s is chosen in subsequent aerodynamic analyses.

Table 5.2: Errors caused by the house bearing on power coefficient under different flow velocities.

Flow velocity, m/s	3.5	4.2	5	6.1	7.3	8.2
Average error in C_P	$\pm$11.36%	$\pm$5.33%	$\pm$5.42%	$\pm$3.25%	$\pm$1.56%	$\pm$1%

Magnitude of the power loss in transmission between gears can be represented by the transmission efficiency, η. The transmission efficiency is calculated by comparing the applied power, P_a, and the transmitted power through gears, P_t:

$$\eta = \frac{P_a}{P_t} \tag{5.4}$$

Table 5.3: Errors caused by gears on power coefficient.

Rotational speed, rpm	Max η	Min η	Average η	Error in C_P
0 – 300	0.92	0.88	0.9	$\pm$1%
300-600	0.92	0.88	0.9	$\pm$2.2%
Average				$\pm$1.6%

Table 5.3 lists errors and the maximum, minimum and average values of efficiency of the gears under different rotational speeds. It can be seen that the maximum error is 2.2% under

the high rotational speeds. During the rotational speed range of 0 rpm - 600 rpm, the average error is 1.6%.

The propagation of all errors in measured and derived variables has influences on estimating power coefficients of the wind turbine prototype in wind tunnel testing. Errors in flow speed, resistive torque and transmission efficiency are considered together in analysing experimental results. Considering the averaged error of $\pm 0.58\%$ in testing flow speed, $\pm 1\%$ caused by bearings and $\pm 1.6\%$ caused by gears, the maximum error in the overall power coefficient is calculated as

$$\text{Total error} = 0.58\% + 1\% + 1.6\% = 3.18\% \tag{5.5}$$

In this section, the test rig for wind tunnel testing in this project has been introduced. The test rig is used to measure the flow velocity, rotational speed and torque of the proposed wind turbine. Errors in experiments are not unavoidable and have been analysed. The calculated overall error of the test is 3.2% which is not significant and can be accepted.

5.2 CFD Modelling of the Proposed Wind Turbine

This section describes the setup of the CFD modelling including the computational domain, mesh strategy, boundary conditions and physical models. A three-dimensional (3D) model of the proposed wind turbine with a computational domain is created by a commercial CFD software package STAR-CCM+. While a two-dimensional (2D) model can save memory and CPU time, models are 3D in the study due to the fact that the flow development in the blade spanwise direction cannot be included in 2D simulations.

5.2.1 Computational Domain and Boundary Conditions

The computational domain for the proposed wind turbine model is shown in Figure 5.6. The domain is 16 times as long as the length (L) of the chamber in the axial direction. Both the domain width and height are 20 times as long as the rotor diameter (D) of the wind turbine. The domain is large enough to reduce the blockage effect of the domain walls [65]. In simulations, the inlet boundary condition was set as a uniform velocity inlet and the downstream boundary was set as a pressure outlet. Surrounding walls of the domain were specified as slip. Surfaces of the wind turbine and chamber were set as non-slip.

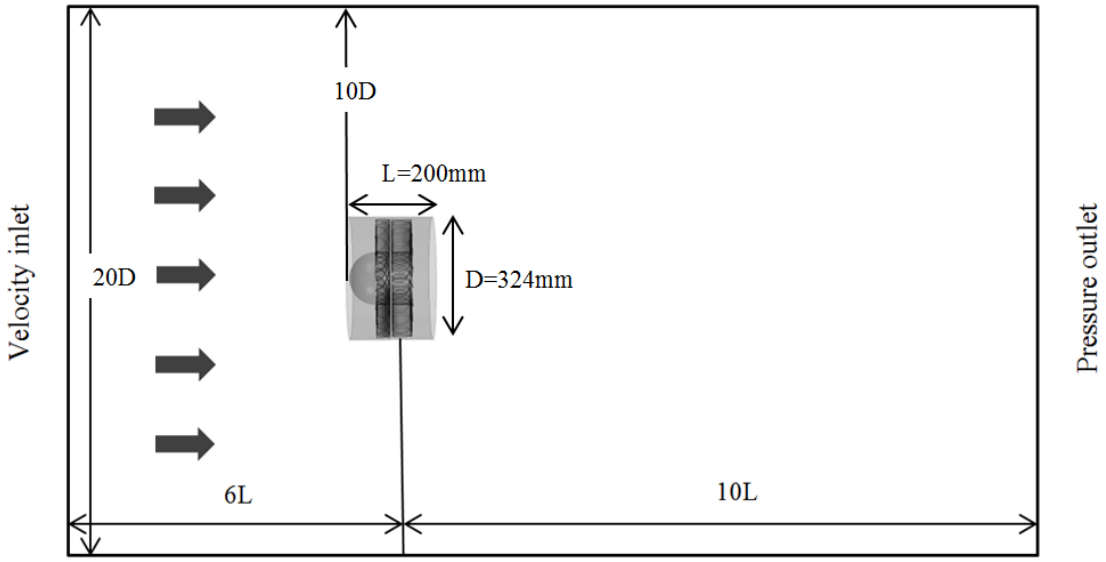

Figure 5.6: Schematic view of the computational domain setup in simulations.

5.2.2 Mesh Setup and Mesh Independence Test

Polyhedral cells were generated for the complex geometry of the proposed wind turbine. The polyhedral meshing can provide a balanced solution for complex mesh generation problems. A mesh independence test was conducted in a cell number range from 3,300,000 to more than 7,000,000. Results with different cell numbers are shown in Figure 5.7. When the cell number is increased from 3,300,000 to 5,800,000, there are significant differences about results and

computational time. Figure 5.7 also shows that when the cell number is increased from 5,800,000 to 7,180,000, the torque difference is less than 0.1%. But the computational time of 5,800,000 cells is 19% less than that of 6,800,000 cells and 27% less than that of 7,180,000 cells. Considered the balance of mesh independency and computational time, approximately 5,800,000 cells were produced in simulations in this project.

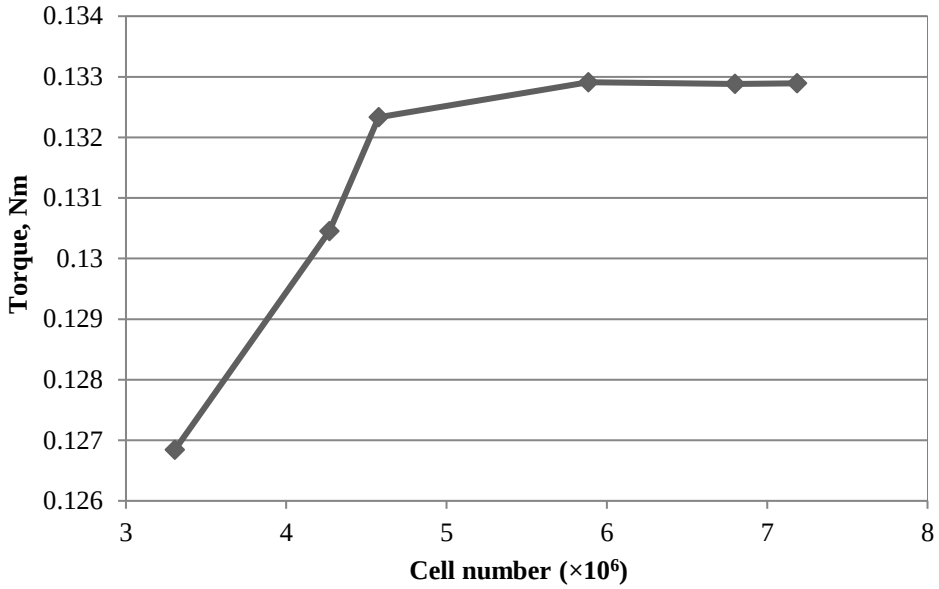

Figure 5.7: Torque values under different cell numbers.

The cell size on a surface can be controlled by a minimum size and a target size. The minimum and target sizes of all the surfaces under the cell number of 5,800,000 are shown in Table 5.4. Figure 5.8 shows the polyhedral cells employed in volume meshing. Surface curvature was set as 36 to create 36 cells around a 360^{o} cylindrical surface. The surface growth rate was set as 1.5 so that an edge of a triangle was 1.5 times its neighbour length when expanding from a shorter edge length to a longer one [151]. The value of 1.5 can have a good balance of the mesh quality and the total number of cells.

Table 5.4: Cell size control on different surfaces.

Surface	Min size (mm)	Target size (mm)
Domain wall	50	100
Chamber surface	2	5
Stator hub	1	3
Guide vane surfaces	1	1.5
Edges of guide vanes	0.5	1
Rotor hub	3	5
Blade surfaces	0.5	1
Edges of blades	0.4	0.8
Blade tips	0.4	0.6
Interfaces	1.5	2.5

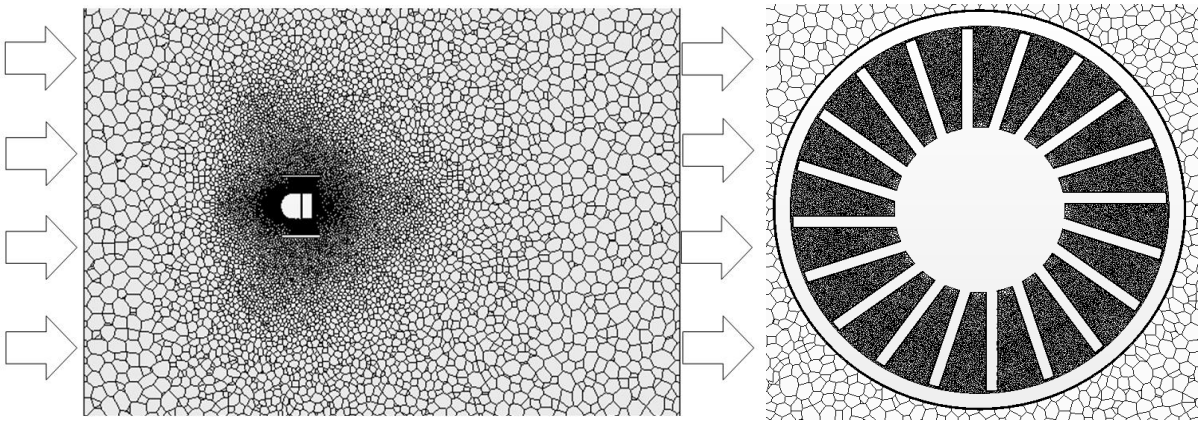

(a) (b)

Figure 5.8: Meshed model: (a) a section view in the flow direction; (b) an axial section view of the wind turbine model.

A boundary layer close to surfaces has complex aerodynamic characteristics caused by the viscosity [152]. In the boundary layer the flow velocity has a rapid change. Flow separation is

also related to the boundary layer, leading to wake formation [152, 153]. To capture the boundary layer correctly, thin prism layers were generated near surfaces. The mesh strategy with thin layers has been employed on studies of wind turbines [154].

The distance from the first layer cell to the body surface can be estimated by a dimensionless wall distance, y^+, which is defined as [99]

$$y^+ = \frac{yu_t}{\upsilon} \tag{5.6}$$

where y is the distance of the first grid layer from the model surface, u_t is the friction velocity and υ is the kinematic viscosity.

Values of y^+ represent three boundary layers close to the model surface: viscous sub-layer, log-law layer and outer layer [96]. The viscous sub-layer contacts with the model surface and is extremely thin ($y^+ < 5$). Flow properties in this layer are dominated by the viscous effect. In the sub-layer the shear stress is approximately constant and equals to the wall shear stress, τ_w. Outside the viscous sub-layer ($30 < y^+ < 500$) there is a log-law layer where both viscous and turbulent effects are important. When the value of y^+ is greater than 500, the outer layer exists where turbulent stresses dominate in this region.

It is known that [97]

$$u_t = \sqrt{\frac{\tau_w}{\rho}} \tag{5.7}$$

and [155]

$$\tau_w = \overline{C_f} \cdot \frac{\rho U^2}{2} \tag{5.8}$$

where u_t is the friction velocity, $\overline{C_f}$ is the friction coefficient and U is the free stream velocity.

The friction coefficient can be estimated from a correlation [156]:

$$\frac{\overline{C_f}}{2} = \frac{0.036}{Re^{1/5}} \tag{5.9}$$

In order to obtain $y^+ < 5$, the distance of the first layer from the blade was set as 0.15 mm. Eight layers were generated with a growth rate of 1.5. Generated cell layers around blades and guide vanes are shown in Figure 5.9.

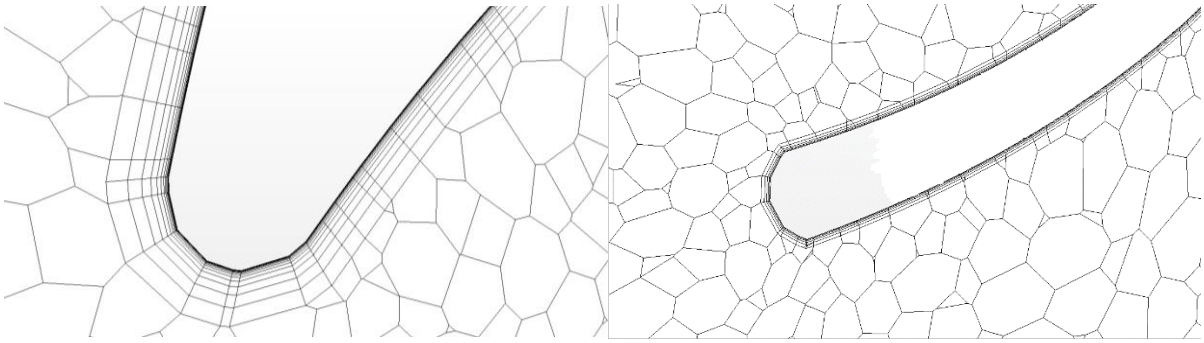

(a) (b)

Figure 5.9: Thin layers near surfaces: (a) cell layers near the blade leading edge; (b) cell layers near the guide vane edge.

5.2.3 Physical Conditions

Wind has low speeds in urban areas and therefore was assumed as incompressible in simulations [33, 34]. The rotor axis of the wind turbine was parallel to the wind direction and the flow properties in simulations were treated as constant in one revolution. Hence, steady solutions were used in this project. Segregated solver was chosen in the simulation as it required less memory and CPU time than the coupled solver [157].

In order to simulate the flow rotation, an individual rotating flow region for the rotor was created. The rotating region was separated from the whole free stream region by the upstream and downstream interfaces. Figure 5.10 shows the interfaces used in simulations. The

interfaces belonged to both the rotating region and the free stream region, and maintained the physics continuity between these two regions. The flow in the rotating region was computed in a Moving Reference Frame (MRF). The flow in the remaining region was computed in an inertial frame of reference. Investigations of impulse turbines and wind turbines with the MRF have produced results with good accuracy [99, 158].

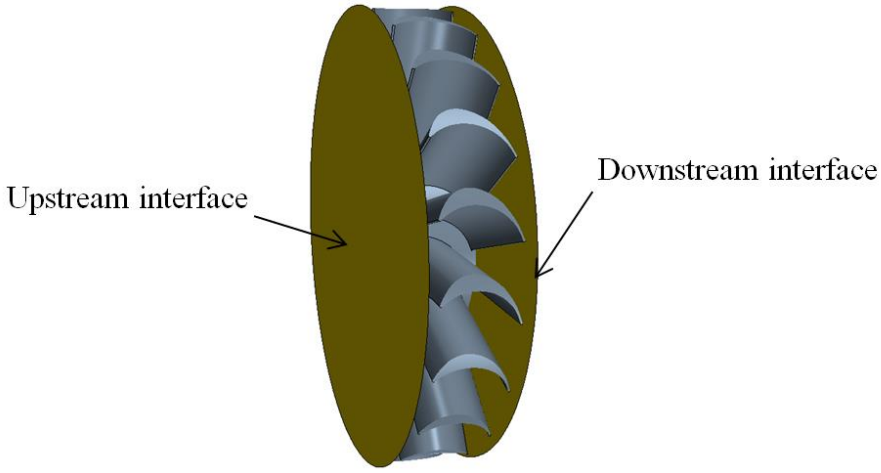

Figure 5.10: Positions of upstream interface and downstream interface in simulations.

A two-layer approach was employed on the k-ε turbulence models in simulations. The two-layer approach divides the flow into two layers. In the layer closer to surfaces, the turbulent dissipation rate, k, and the turbulent viscosity, ε are specified as functions of wall distances. Far from the wall, the transport equations of turbulence models are calculated. With the aid of the two-layer approach, the k-ε models have less mesh dependence and more numerical stability [96].

The review about turbulence models in Section 3.1.3 indicates that four turbulence models, namely the standard k-ε, realisable k-ε, standard k-ω and SST k-ω model, all have been used for investigations of wind turbines. These four turbulent models were employed in modelling

the performance of the proposed wind turbine. The suitable turbulence model for the proposed wind turbine can be identified through the experimental validation.

5.3 Aerodynamic Analysis of the Proposed Wind Turbine

This section presents the aerodynamic analyses of the proposed wind turbine model analysed by both the wind tunnel testing and the CFD simulations. The computational wind turbine model and the prototype for wind tunnel testing have the same dimensions as presented in Chapter 4. The power coefficient, torque coefficient and thrust coefficient are represented quantitatively to illustrate the power output, torque and thrust of the wind turbine.

The power coefficient (C_P) can evaluate the capability of power output generation for a wind turbine and is defined as the ratio of the shaft power output from a wind turbine to the power available from the wind [18]:

$$C_P = \frac{P}{0.5\rho U^3 \pi R^2} \tag{5.10}$$

where P is the power output from the wind turbine, ρ is the air density, U is the wind velocity and R is the blade radius.

Torque coefficient (C_T) has been used to assess the mechanical torque generated by a wind turbine. The wind turbine with high C_T can start and work under low velocity wind [52]. Torque coefficient is defined as [57]:

$$C_T = \frac{C_P}{\lambda} = \frac{\mathrm{T}}{0.5\rho U^2 \pi R^3} \tag{5.11}$$

where T is torque generated from the wind turbine.

A dimensionless parameter, thrust coefficient (C_N), can be used to estimate the thrust of a wind turbine and is determined as follows [19]:

$$C_N = \frac{F_N}{0.5\rho U^2 \pi R^2} \tag{5.12}$$

In aerodynamic analyses of wind turbines, wind velocity is normally represented by a dimensionless term, tip speed ratio (λ), as follows [18]:

$$\lambda = \frac{\omega R}{U} \tag{5.13}$$

where ω is the angular speed of a rotor.

5.3.1 Validation of Numerical Results with Experimental Results

Chapter 3 has reviewed features of turbulence models and their applications. To simulate the rotating flow around this wind turbine, the realisable k-ε model may be better on prediction of flow rotation than the standard k-ε model [117, 118]. When simulating the air flow around the blade, flow separation may appear near the blade surface that can affect the accuracy of results [152, 153]. As discussed in Section 3.1.3, the k-ω model family has an advantage in prediction of properties of the flow near the surface [122, 123]. Based on the literature review, it is difficult to draw a conclusion on which turbulence model is more suitable for this proposed wind turbine. In order to identify the most suitable numerical configuration, the performances of four turbulence models are compared and validated with experimental results.

Figure 5.11 shows a comparison about power coefficient between numerical results and experimental results. Based upon error analyses in Section 5.1.2, the free stream velocity is 8.2 m/s in simulations. The error bar on experimental data represents a scattering of ±3.18%. It can be seen that the numerical results from all four turbulence models have a similar trend of the $C_P - \lambda$ curves to that of the experimental results. Figure 5.11 also shows that the maximum power coefficient is obtained at λ = 0.66. It can be seen that except for the standard k-ε model, numerical results from the other three models agree well with the experimental results.

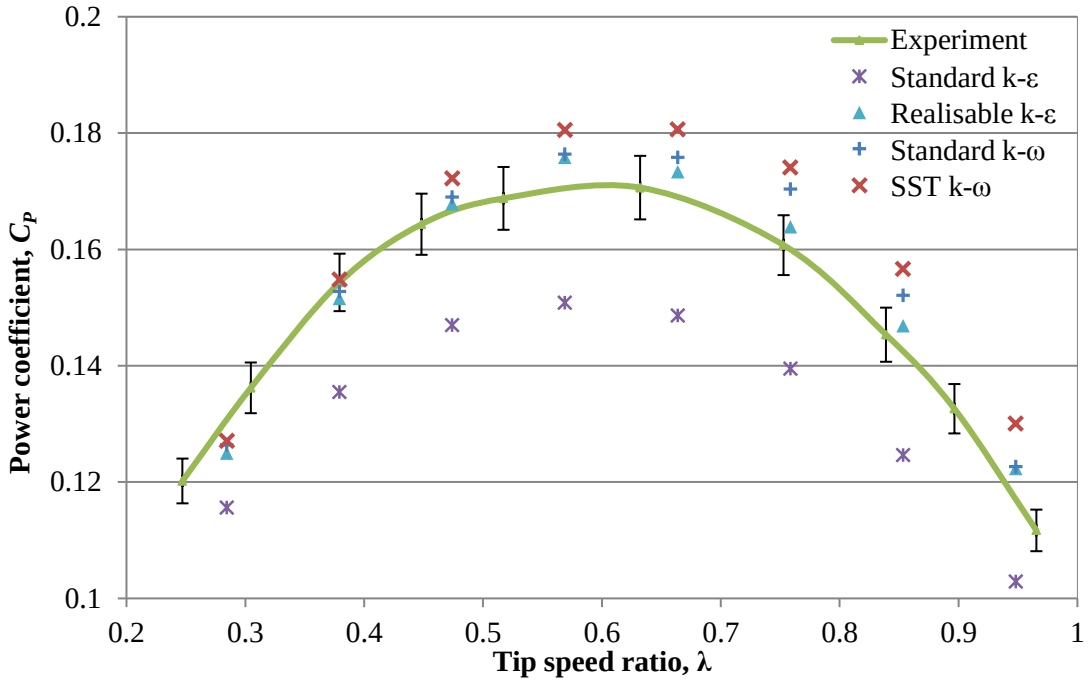

Figure 5.11: Comparison of power coefficient between numerical results and experimental data at U = 8.2m/s.

As shown in Figure 5.11, values of C_P from the standard *k-ε* model are lower than those from experiments, which is caused by the weakness of this model in predication of flow rotation. The eddy viscosity formulation in the standard *k-ε* model cannot describe the rotating flow well [117, 159]. Compared with the standard *k-ε* model, the realisable *k-ε* model has better capacity in predictions of flow rotation [117]. The eddy viscosity formulation of the realisable *k-ε* model consists of a mean rotation rate, which enables the model to simulate the rotating flow [118]. Figure 5.11 also shows that two *k*-ω models are also better than the standard *k-ε* model for this wind turbine. This can be because the *k*-ω model is integrated directly to the low Reynolds number flow near walls without the aid of wall-damping functions while the standard *k-ε* model has to use functions in solution of the flow near walls [112]. Moreover, the SST *k*-ω model is good at predicting the flow with adverse pressure gradients by avoiding over estimation of the turbulence length scale in turbulent properties [123]. It is worth nothing

that results from two k-ω turbulence models are always higher than the experimental data, which may be linked to the weakness in capturing effects of system rotation [160]. Based on the results shown in Figure 5.11, the realisable k-ε model has been employed in analyses of the proposed wind turbine.

Simulations with four turbulence models have predicted the pressure distribution on the blade aerofoil. Figure 5.12 shows the pressure distribution on a blade section selected at r = 140 mm where the blade section has the largest contribution to torque. It can be seen that four turbulence models have similar pressure distributions, such as the positions of the maximum pressure and the minimum pressure on the aerofoil. However, the pressure values are different among the four turbulence models.

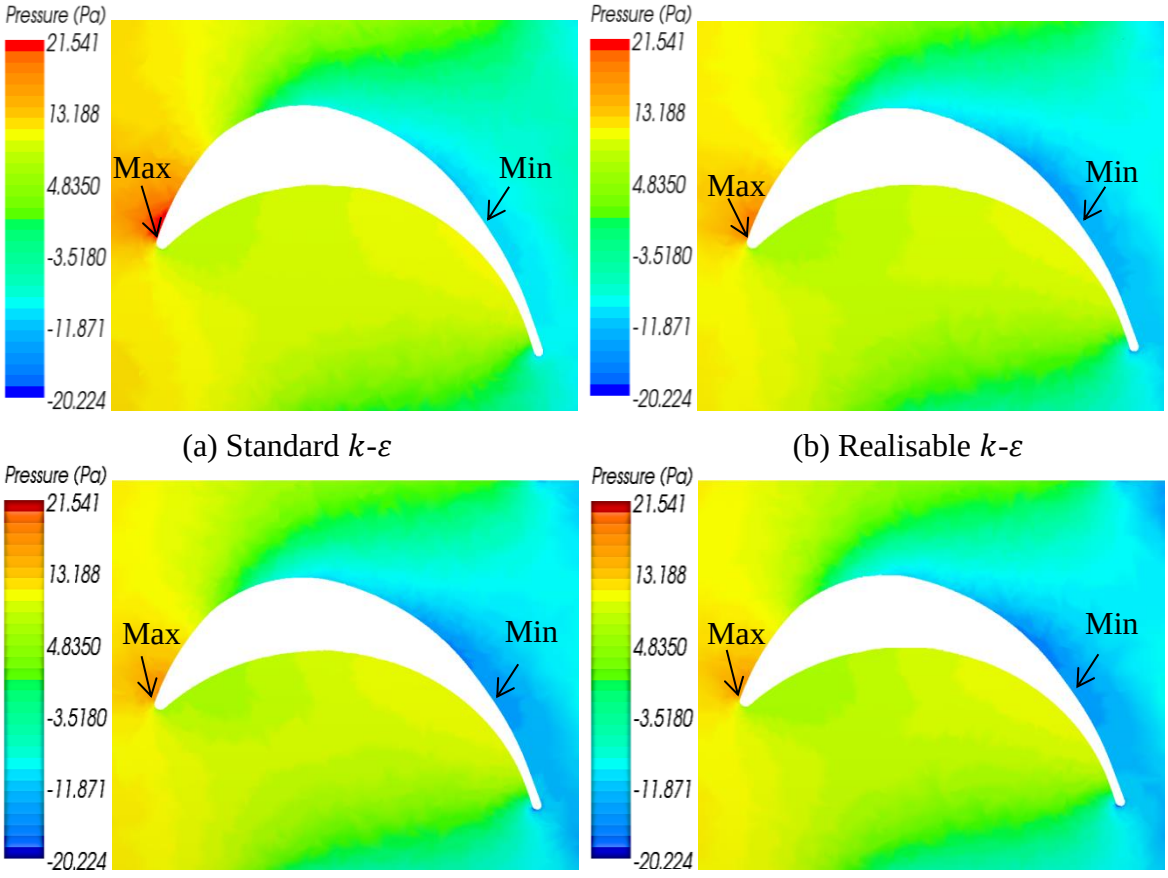

(a) Standard k-ε (b) Realisable k-ε

(c) Standard k-ω (d) SST k-ω

Figure 5.12: Pressure distributions on the aerofoil predicted by four turbulence models at r = 140 mm and λ = 0.76.

As shown in Figure 5.12, there is a pressure increment along the aerofoil surface from the minimum pressure position towards the trailing ledge, which causes an adverse pressure gradient. The adverse pressure gradient results in the flow separation near the trailing edge of the aerofoil. The flow separation on the blade was predicted by all turbulence models in simulations.

Pressure coefficient, a dimensionless term, represents the magnitude of pressure on the blade aerofoil. The pressure coefficient is calculated with Eq. (2.4) as given in Section 2.1.3. Figure 5.13(a) shows pressure coefficient distributions on the upper and lower surfaces of the blade aerofoil at r = 140 mm. The upper surface and the lower surface are separated by the leading edge and the trailing edge. Figure 5.13 shows that at $\lambda = 0.76$, the stagnation point just occurs on the leading edge where pressure coefficient has the maximum value. The enclosed areas of the pressure coefficient curves represent the magnitude of the normal force acting at a blade section. As shown in Figure 5.13(a), in the x/c range of 0 - 0.15 corresponding to the leading edge region of the aerofoil, the pressure coefficient on the upper surface is higher than that on the lower surface, which leads to a negative enclosed area (marked by $-$) representing a negative normal force. The negative normal force can hinder the rotation of a wind turbine. In the area marked by +, the pressure coefficient on the upper surface is lower than that on the lower surface, which provides a positive normal force that contributes to power generation. As shown in Figure 5.13(a), the positive area is much larger than the negative area. Therefore, the positive force is dominant and this blade section has contributed to the torque and power generation.

Figure 5.13(b) shows the comparison of pressure coefficients among the four turbulence models. It can be seen that the standard k-ε model has the smallest positive area (+) for

positive normal force and the largest negative area (-) for negative normal force. As a result, the standard *k-ε* model has produced the smallest power coefficient as shown in Figure 5.11.

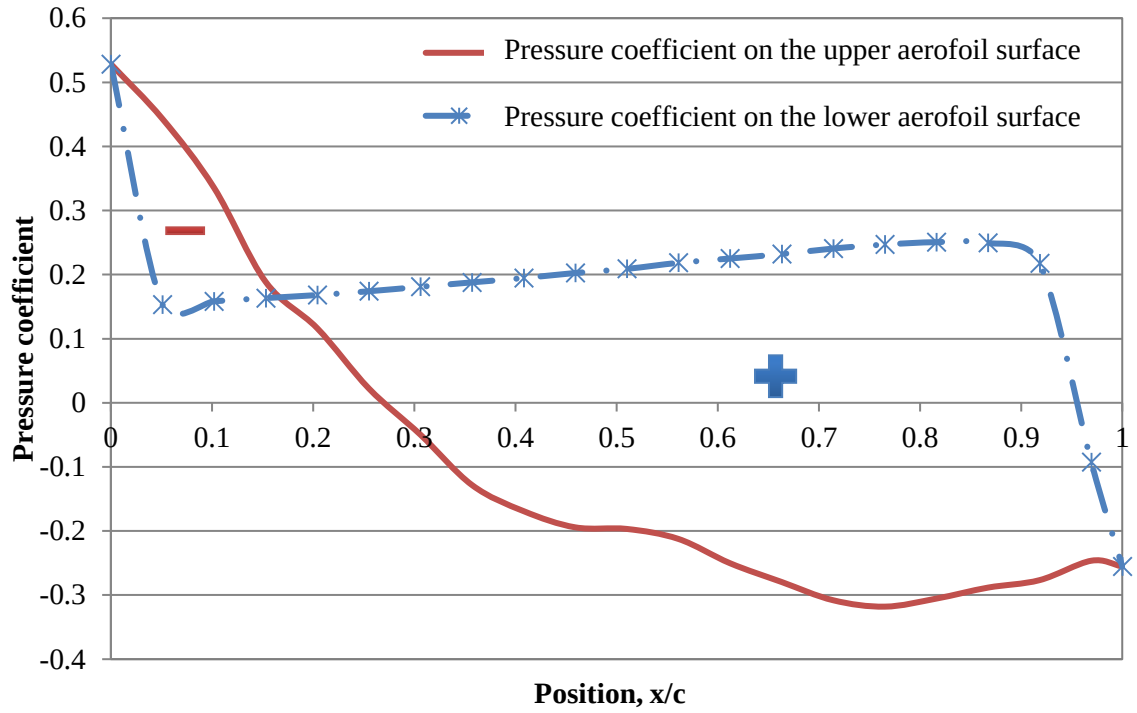

(a)

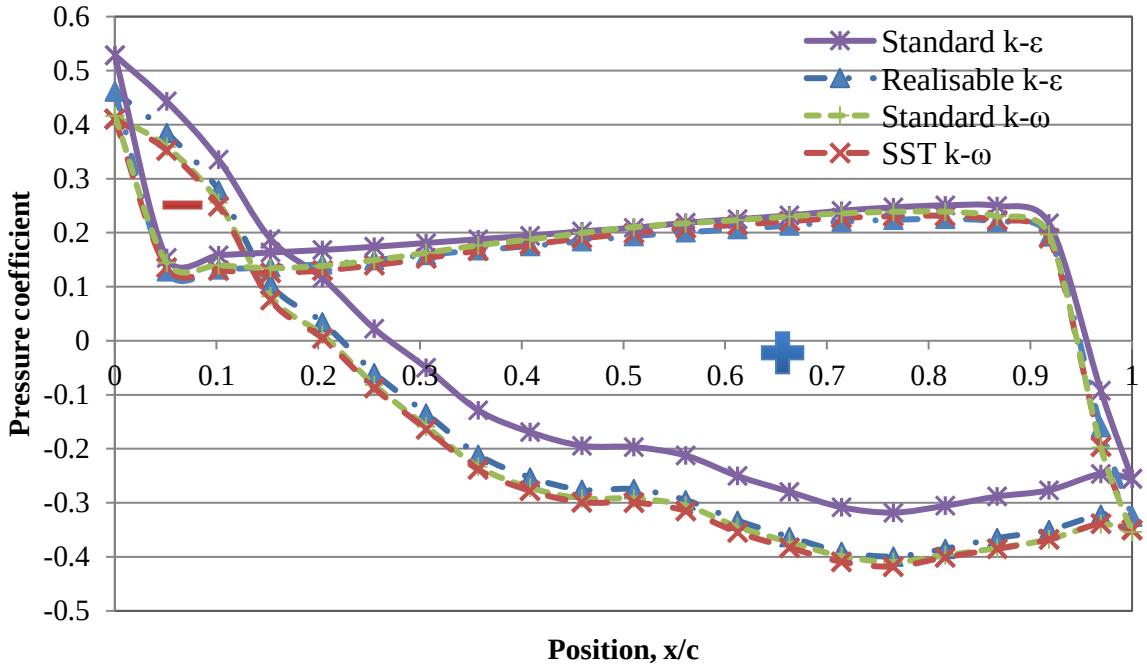

(b)

Figure 5.13: Pressure coefficients on the blade aerofoil at r = 140 mm and λ = 0.76: (a) by the standard *k-ε* model; (b) by four turbulence models.

Figure 5.14 shows the contributions of different blade sections to the normal forces at λ = 0.66 where the wind turbine has the maximum power coefficient. It can be seen that the normal force per unit length (*dF'*) achieves the maximum value at r = 135 mm. The blade sections in the range of r = 70 mm – 80 mm are close to the hub and have negative values of *dF'* as the pressure on the upper aerofoil surface is higher than that on the lower surface.

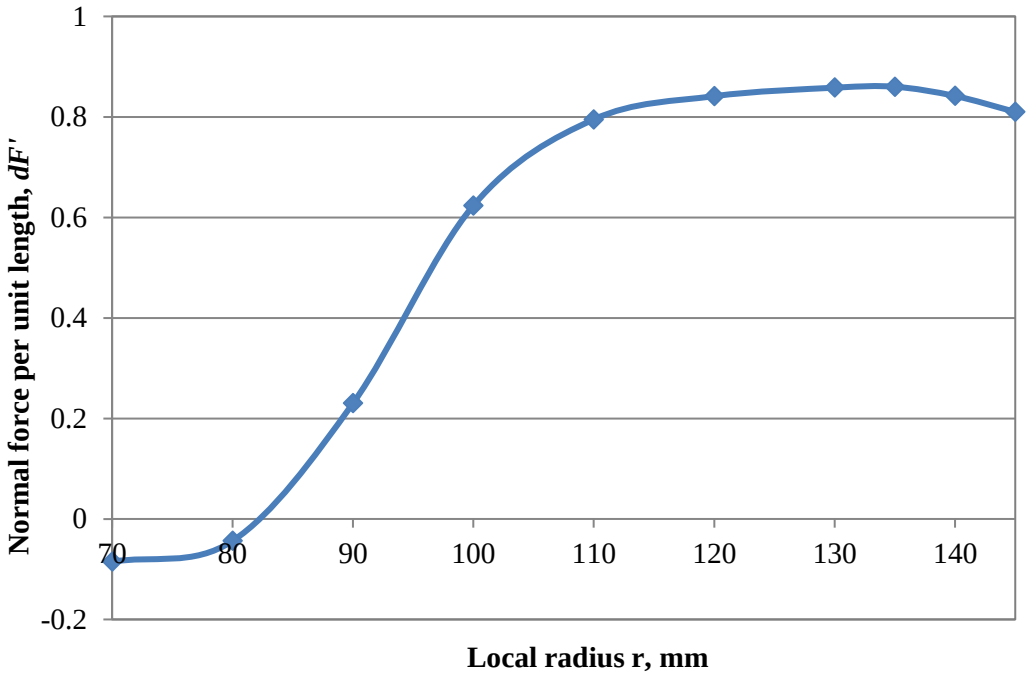

Figure 5.14: Contributions of blade sections to the normal force at λ = 0.66 by the realisable *k-ε* model.

Contributions of blade sections to torque can be obtained by multiplying the normal force per unit length (*dF'*) by local radius (r). Figure 5.15 shows values of *dT* along the blade. It can be seen that *dT* rises steadily against radius, r, and has a peak value at r = 140 mm. Hence, the blade section at r = 140 mm provides the largest contribution to torque and power generation. That is why the analyses about pressure and pressure coefficient were conducted on the blade section at r = 140 mm as shown in Figures 5.12 – 5.13.

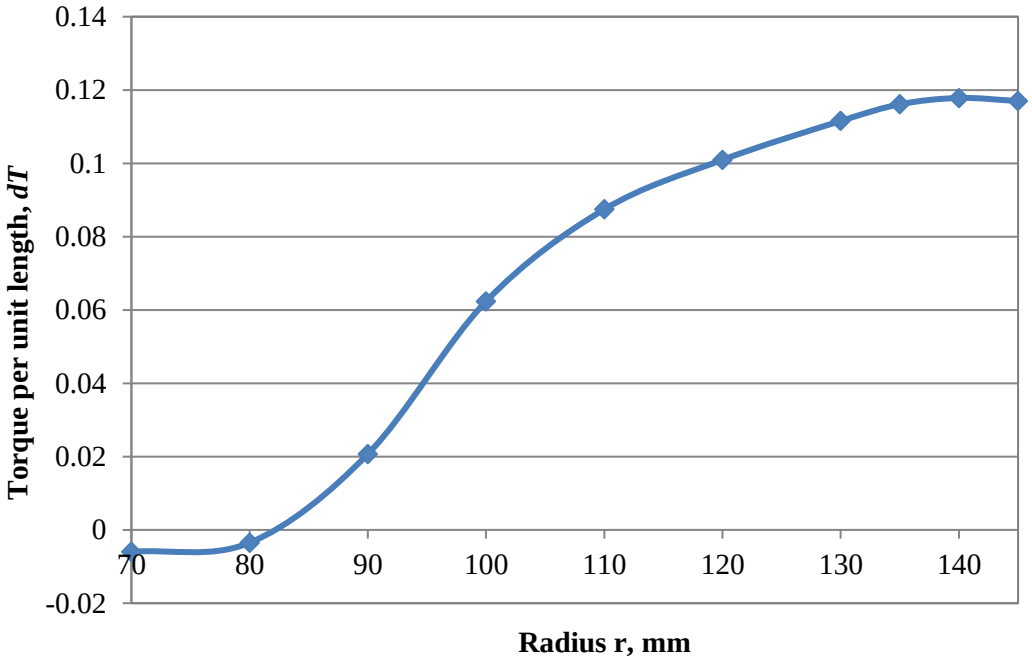

Figure 5.15: Contributions of blade sections to torque at λ = 0.66 by the realisable *k-ε* model.

5.3.2 Power Output and Power Coefficient

In wind tunnel testing, power output of the wind turbine prototype was obtained under a flow velocity range of 3.5 m/s - 8.2 m/s. This velocity range represents the typical wind condition in urban areas. The relationships between the power coefficient (C_P) and the tip speed ratio (λ) under different velocities are shown in Figure 5.16. The vertical bars represent the scattering of the experimental results. It can be seen that the power coefficient increases with the tip speed ratio to a maximum value at the middle tip speed ratio, then the power coefficient decreases. A curve fit in Figure 5.16 shows that the power coefficient increases with the wind speed. The maximum power coefficient is 0.174 at the wind speed of 8.2 m/s. The tip speed ratio corresponding to the maximum power coefficient is λ = 0.66.

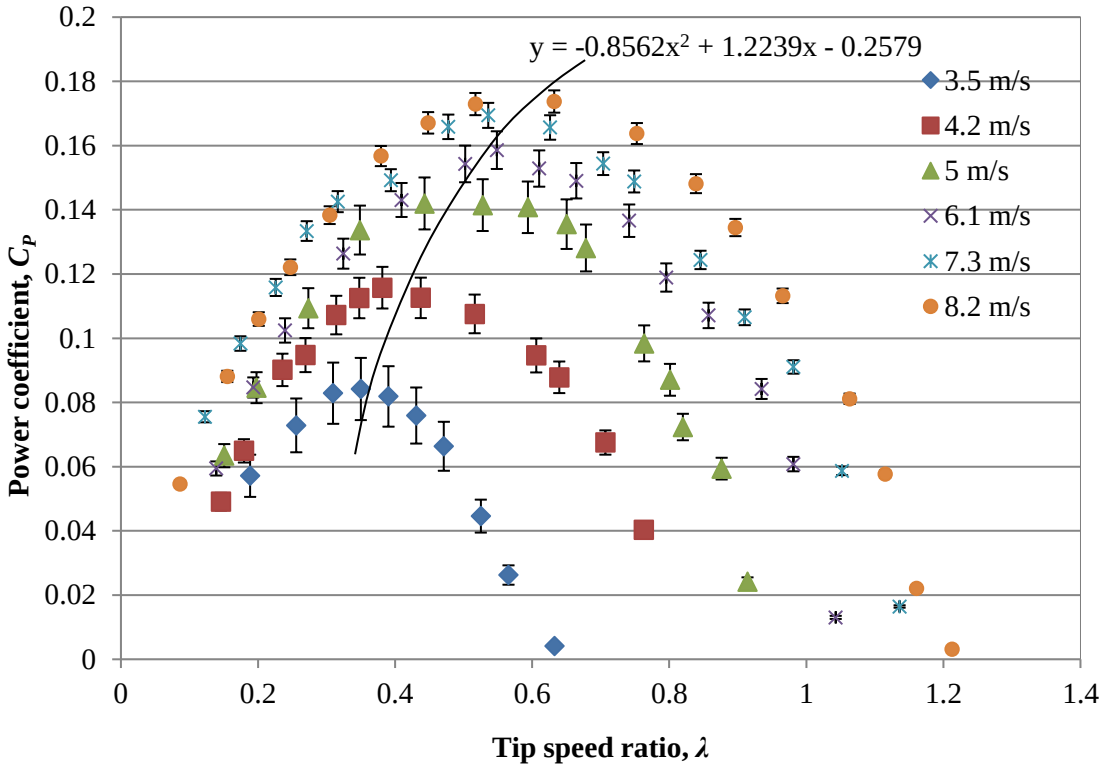

Figure 5.16: Distributions of experimental power coefficient of the proposed wind turbine under different wind velocities.

Figure 5.17 shows the relationships between the power output and rotational speed under different flow velocities. The curve fit shows that higher wind velocity results in greater power output. The wind turbine can produce power up to 4.5 W at the flow velocity of 8.2 m/s and the rotational speed corresponding to the maximum power output is approximately 350 rpm.

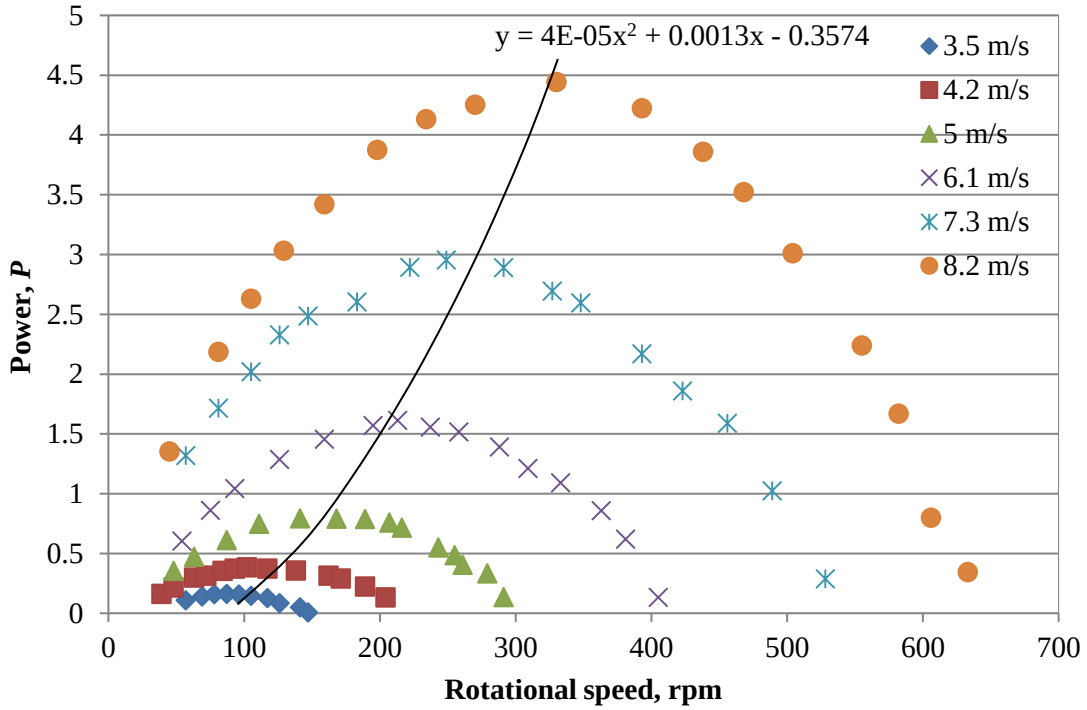

Figure 5.17: Distributions of experimental power output of the proposed wind turbine under various wind velocities.

Figure 5.18 shows the pressure coefficient distributions obtained from simulations in order to analyse aerodynamic performances of the proposed wind turbine. With different values of λ, positions of the stagnation point are also different. Pressure coefficient curves under different tip speed ratios (λ) are compared. The enclosed area marked by + represents the positive normal force and has a steady decline when λ is increased. Figure 5.18(d-f) shows that, at λ = 0.66 and beyond, the area (marked by −) represents the negative normal force and is increased significantly with an increment of λ. When λ exceeds 0.66, the increased negative normal force is the major reason for the low power coefficients shown in Figure 5.16. Figure 5.18 also shows that areas (marked by −) occur in the x/c range of 0 – 0.4 that represents the leading edge region of the aerofoil. It means that the negative normal force is always produced in the leading edge region of the aerofoil.

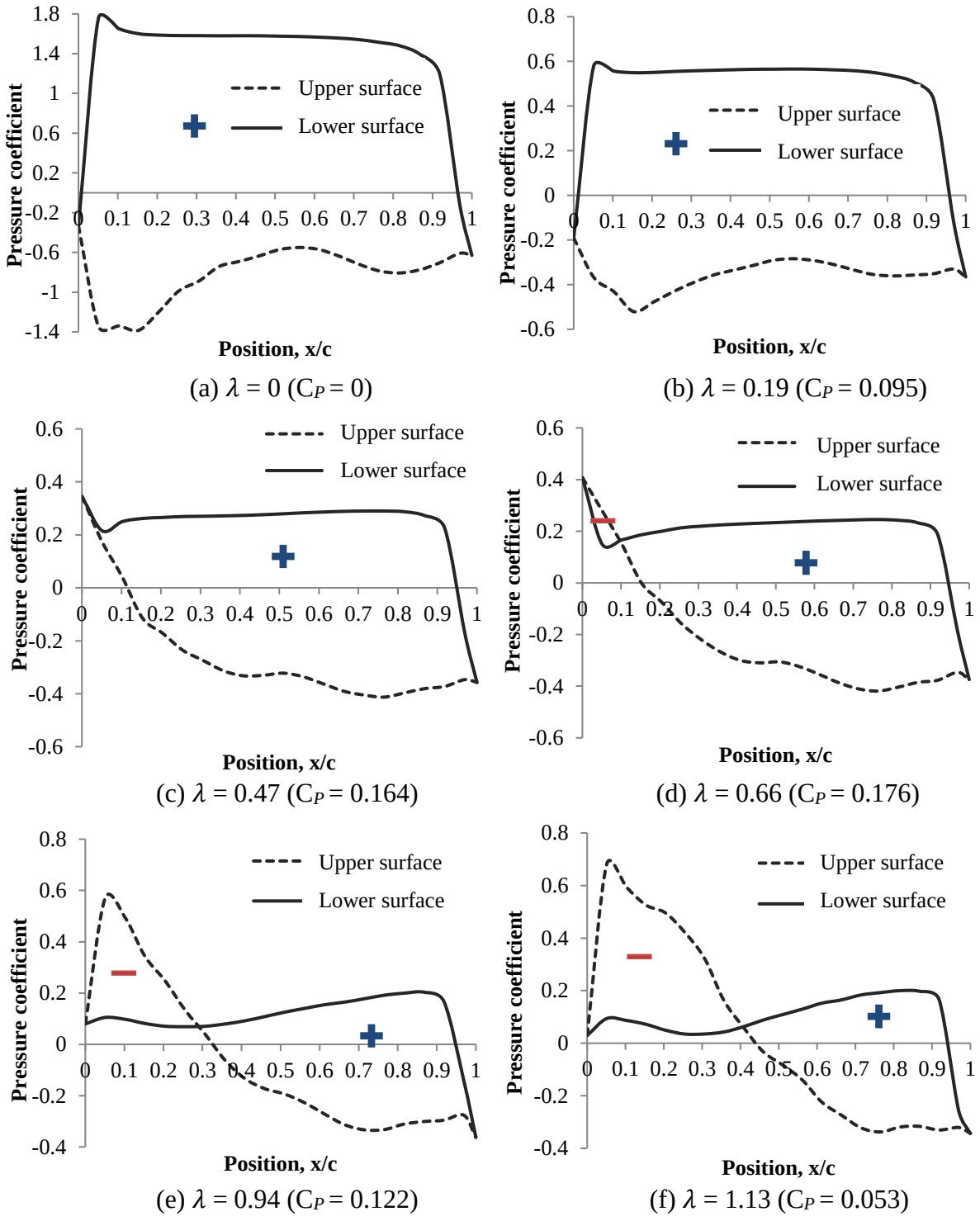

(a) $\lambda = 0$ ($C_P = 0$)

(b) $\lambda = 0.19$ ($C_P = 0.095$)

(c) $\lambda = 0.47$ ($C_P = 0.164$)

(d) $\lambda = 0.66$ ($C_P = 0.176$)

(e) $\lambda = 0.94$ ($C_P = 0.122$)

(f) $\lambda = 1.13$ ($C_P = 0.053$)

Figure 5.18: Pressure coefficient distributions on the blade section at r = 140 mm under the flow speed of 8.2 m/s.

5.3.3 Torque and Starting Wind Velocity

Figure 5.19 shows the torque coefficient distributions under different flow velocities. In wind tunnel testing, when the wind turbine was stationary (λ = 0), the wind turbine had the maximum torque coefficient. As shown in Figure 5.19, torque coefficient has the maximum value of around 0.7 at λ = 0. The maximum torque coefficient of 0.7 is greater than that of some HAWTs [18]. Results also show that the values of torque coefficient under different flow velocities are close when the tip speed ratio is below 0.2. In the range of high tip speed ratios (λ > 0.2), higher wind velocity can result in larger torque coefficient.

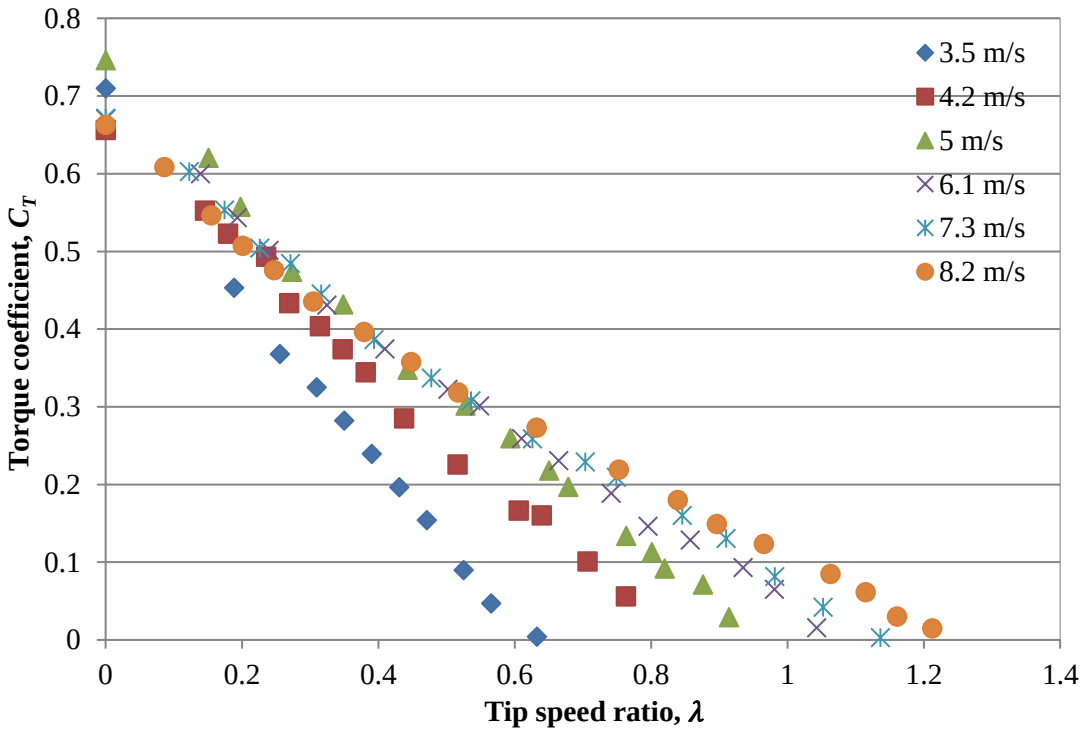

Figure 5.19: Distributions of experimental torque coefficient of the proposed wind turbine under various wind velocities.

A large torque coefficient can allow the wind turbine to start up under low-velocity wind [52]. The starting capability of the wind turbine was tested in the wind tunnel. Figure 5.20 shows the relationship between the starting wind velocity and the maximum rotational speed of this

wind turbine. There is a three-order regression analysis in Figure 5.20. The regression analysis shows that the maximum rotational speed rises quickly with wind speeds. The high wind speed causes high Reynolds number that can improve aerodynamic performances of the blades of this wind turbine [49, 50]. It can also be seen that this wind turbine can operate at the lowest wind velocity of 1.6 m/s. The wind velocity of 1.6 m/s is in the low end of the range of wind velocities in an urban environment. Hence, the proposed wind turbine has a good starting capability and can capture wind energy in an urban environment.

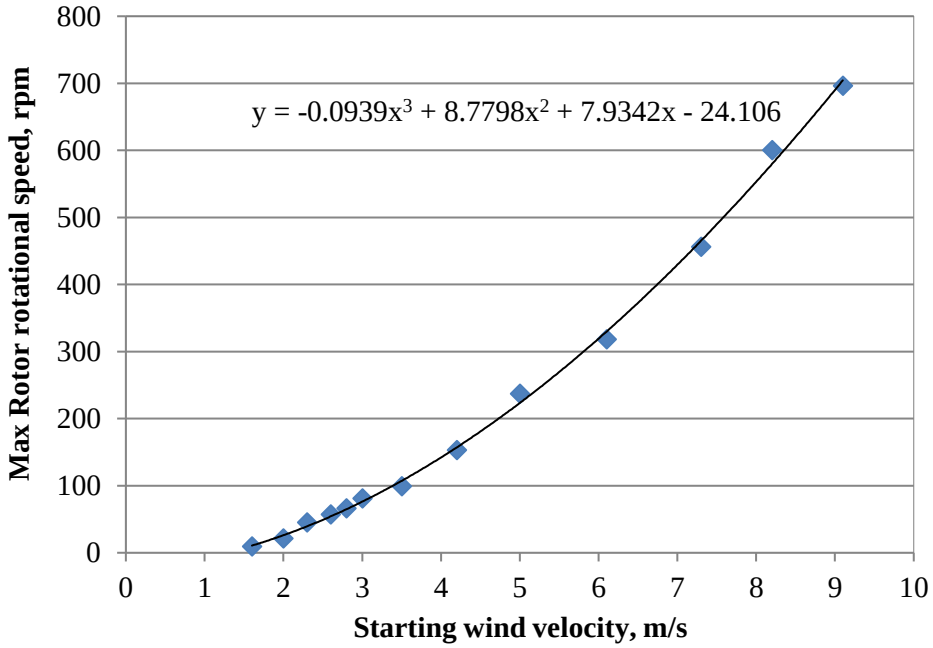

Figure 5.20: Starting wind velocities of the proposed wind turbine in wind tunnel tests.

5.4 Effects of the Stator on Passing Flow

As discussed in Section 4.3, the stator with guide vanes is a part of the presented wind turbine, based upon the impulse turbine technology. The air flow passes the stator firstly and then the rotor. Properties of the passing flow are affected by the stator. Hence, influences of the stator on flow properties are analysed in this section.

5.4.1 Effects of the Stator on Flow Velocity

In order to study the effects of the stator on the flow characteristics, the rotor was not considered in simulations and wind tunnel testing in this section. Figure 5.21(a) shows the stator model inside the cylindrical chamber. Figure 5.21(b) shows selected positions for testing flow velocity near the rear of the guide vane. The test position is defined by its local radius from the centre of the stator. In the wind tunnel testing, flow velocities were measured by a Pitot tube at these positions.

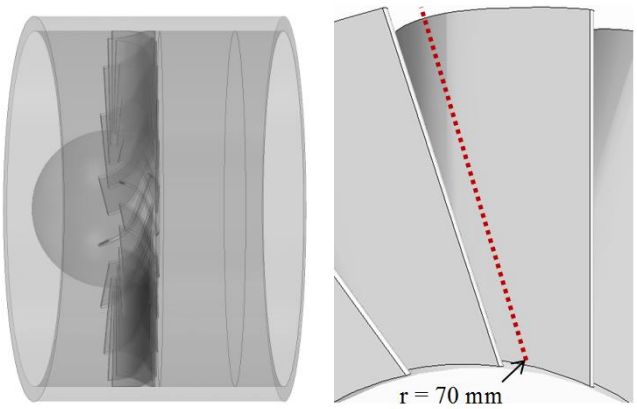

(a) (b)

Figure 5.21: Stator model in simulations: (a) stator inside the cylindrical chamber; (b) testing positions both in experiments and simulations.

Figure 5.22 presents the wind speed ratios at the selected positions when free stream velocity is 5 m/s. The velocity of 5 m/s is a medium value in the general range of wind speeds in urban areas and has been used in investigations of wind turbines [70]. Studying with the speed of 5 m/s can save both the cost and time of wind tunnel tests. As shown in Figure 5.22, the results from both the wind tunnel tests and computational simulations correlate well with each other. The small discrepancies could be caused by the roughness of the prototype surface. It can be seen that most wind speed ratios are greater than 1.0 except for the positions near the chamber wall. The maximum flow velocity ratio exceeds 1.2 from r = 82.5 mm to r = 100 mm. The

wind velocity ratio exceeds 1.0 on the positions from r = 70 mm to r = 132.5 mm that occupies 75.8% of the guide vane length. It shows that the stator can increase the velocity of the passing flow significantly in a wide range of the local radius.

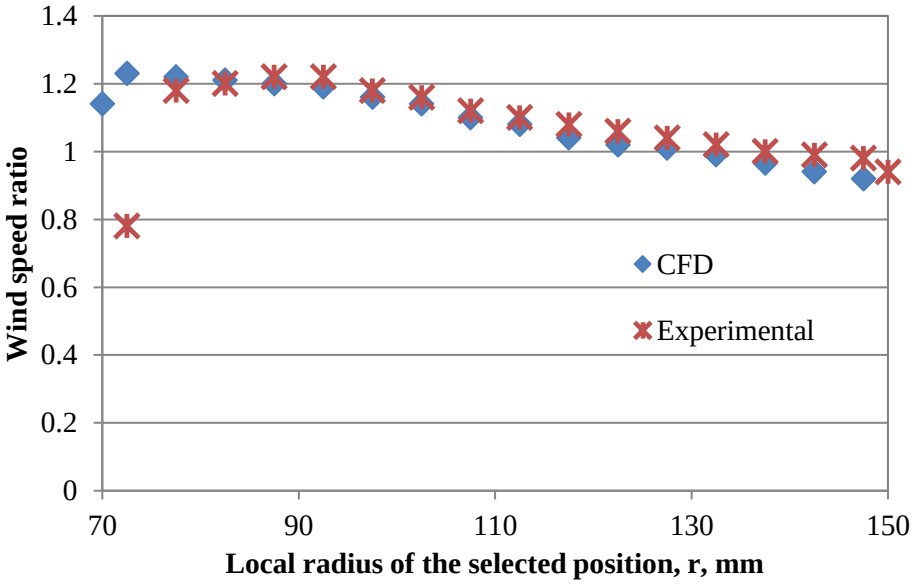

Figure 5.22: Comparison of wind velocity ratios between the experimental and numerical results at the selected positions.

It has been observed that changes of the flow characteristics are affected by the guide vane geometry. Figure 5.23(a) shows a schematic view of the flow passage between two guide vanes. From the entrance to the exit of the flow passage, the cross sectional area of the flow passage decreases continuously (the entrance area of flow passage, $A1 >$ the exit cross sectional area of flow passage, $A2$) and this feature acts as a nozzle cascade. The nozzle cascade can increase the speed of the passing flow.

Figure 5.23(b) shows the velocity and pressure of the passing flow at r = 100 mm where the wind speed has the maximum value. These data were obtained at the test points on the central line between two guide vanes as shown in Figure 5.23(a). Figure 5.23(b) shows that the air

flow has the highest pressure and lowest velocity at the entrance of the flow passage due to the influence of the nozzle cascade. When the distance is less than 15 mm from the entrance of the flow passage, the velocity and pressure change slowly. But both the velocity and pressure have changes with large slopes from a distance of x = 15 mm to x = 30 mm. This is caused by a sharp reduction of the cross sectional area of the flow passage after x = 15 mm. Distributions of the flow velocity and pressure at other local radii are shown in Appendix E and similar phenomenon can be found.

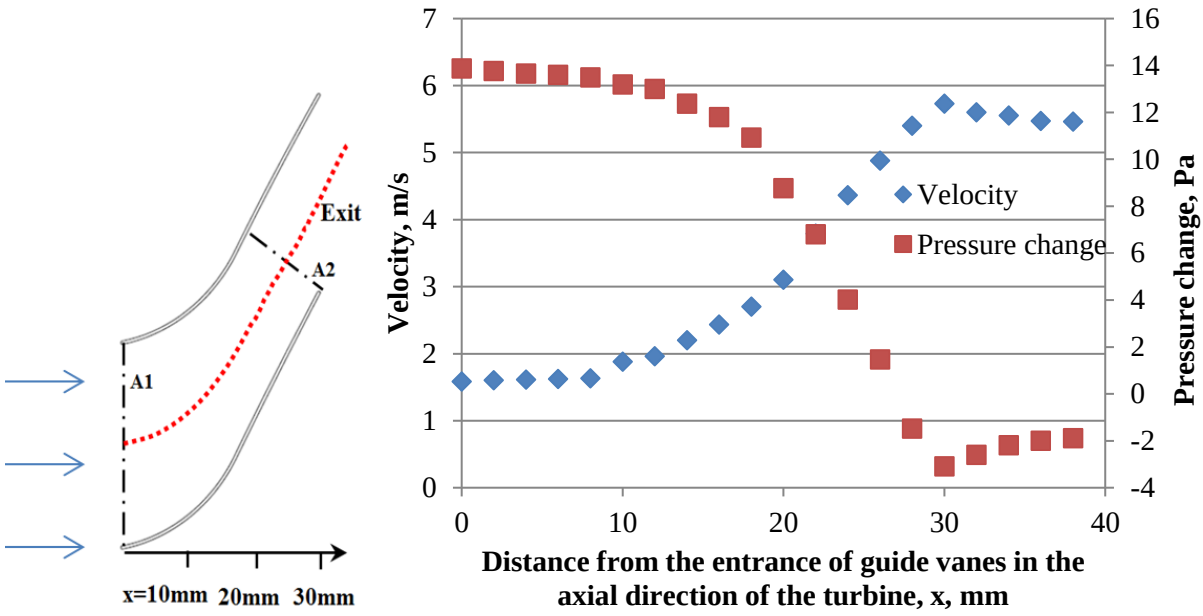

(a) (b)

Figure 5.23: Properties of the flow passing guide vanes: (a) flow passage between two guide vanes; (b) velocity and pressure along the centre line at r = 100 mm.

5.4.2 Effects of the Stator on Flow Direction

The stator with guide vanes can not only increase the passing flow velocity, but also affect the flow direction. The flow direction inside the omni-flow wind system with the stator has been compared with that without the stator. Simulations in this section employed the computational setup presented by Zhang [15]. Figure 5.24(a) shows the computational domain and Figure

5.24(b) shows the free stream direction for the omni-flow wind energy system model in simulations. Inside the omni-flow system, the flow direction was recorded by approximately 300 probes at a height of 260 mm as shown in Figure 5.25(a). At the height of 260 mm, the flow velocity achieved the highest speed [15]. In the study of flow direction inside the omni-flow system with the stator, the flow direction was recorded by approximately 300 probes at a height of 420 mm as shown in Figure 5.25(b). At the height of 420mm, the flow just leaves the stator.

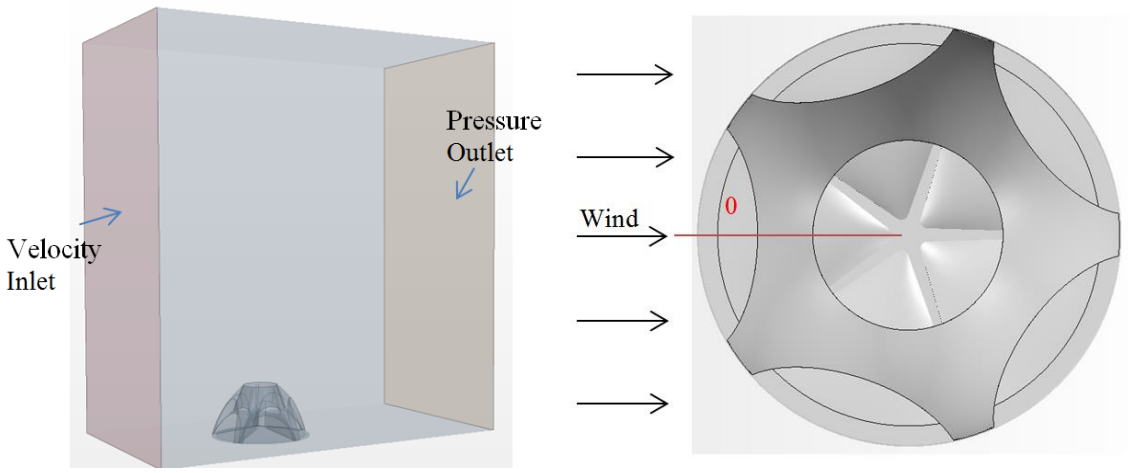

(a) (b)

Figure 5.24: Study of flow direction: (a) computational domain; (b) the direction of free stream in simulations [15].

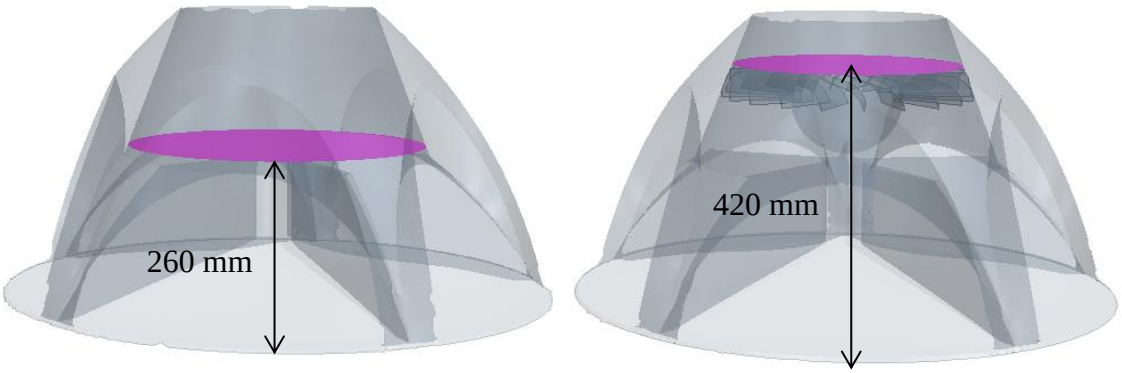

(a) (b)

Figure 5.25: Positions for recording flow directions: (a) the system model without a stator; (b) the system model with a stator.

The flow direction is represented by an angle, φ, referred to the horizontal axis. Figure 5.26 shows the angle φ between the flow direction and the horizontal axis. Inside the omni-flow system without the stator, the optimal flow direction is vertical so $\varphi_{optimal} = 90^o$. Figure 5.27 shows values of φ inside the omni-flow wind energy system without the stator. Results show that values of φ are in a range from -60^o to 80^o, which means the optimal flow direction $\varphi_{optimal} = 90^o$ is out of the range ($-60^o < \varphi < 80^o$). For best performances, a conventional wind turbine has to operate under the optimal flow direction. Therefore, conventional wind turbines are difficult to work well inside the omni-flow wind energy system.

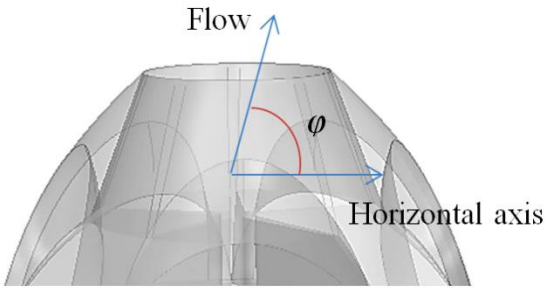

Figure 5.26: Angle of the flow direction, φ.

When the stator is installed inside the omni-flow system, the optimal flow direction is 20^o ($\varphi_{optimal} = 20^o$) as the guide vane has a setting angle of 20^o. Figure 5.28 shows the values of φ obtained inside the omni-flow system with the stator, which are in a range from -10^o to 30^o. It can be seen that the optimal flow direction $\varphi_{optimal} = 20^o$ is within the range ($-10^o < \varphi < 30^o$). Therefore, the proposed wind turbine has the potential to operate well inside the omni-flow system. Compared with the range ($-60^o < \varphi < 80^o$) shown in Figure 5.27, this range ($-10^o < \varphi < 30^o$) affected by the stator is reduced by 71%.

This section shows the analysis of the flow direction when the free stream is at 0^o to the omni-flow system as shown in Figure 5.24(b). Results indicate that the stator can optimise the flow direction and improve the flow quality inside the omni-flow system. When the free

stream is at 12°, 24° and 36° to the omni-flow system, values of φ are given in Appendix F. A similar conclusion can be drawn.

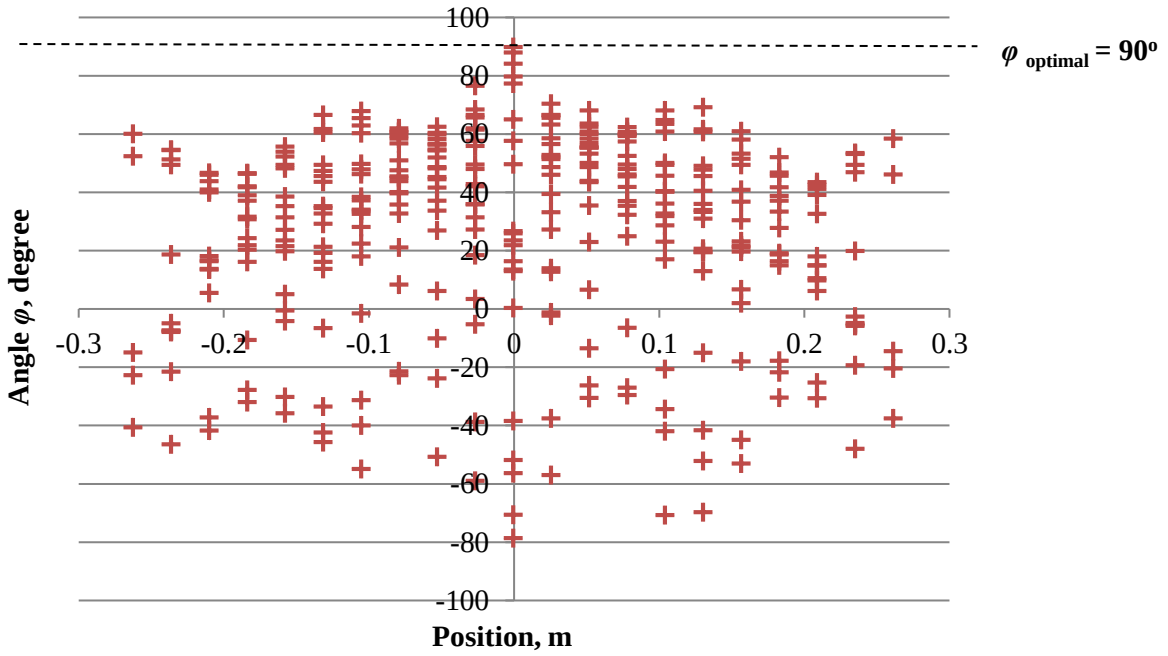

Figure 5.27: Angles of flow directions inside the omni-flow system without the stator.

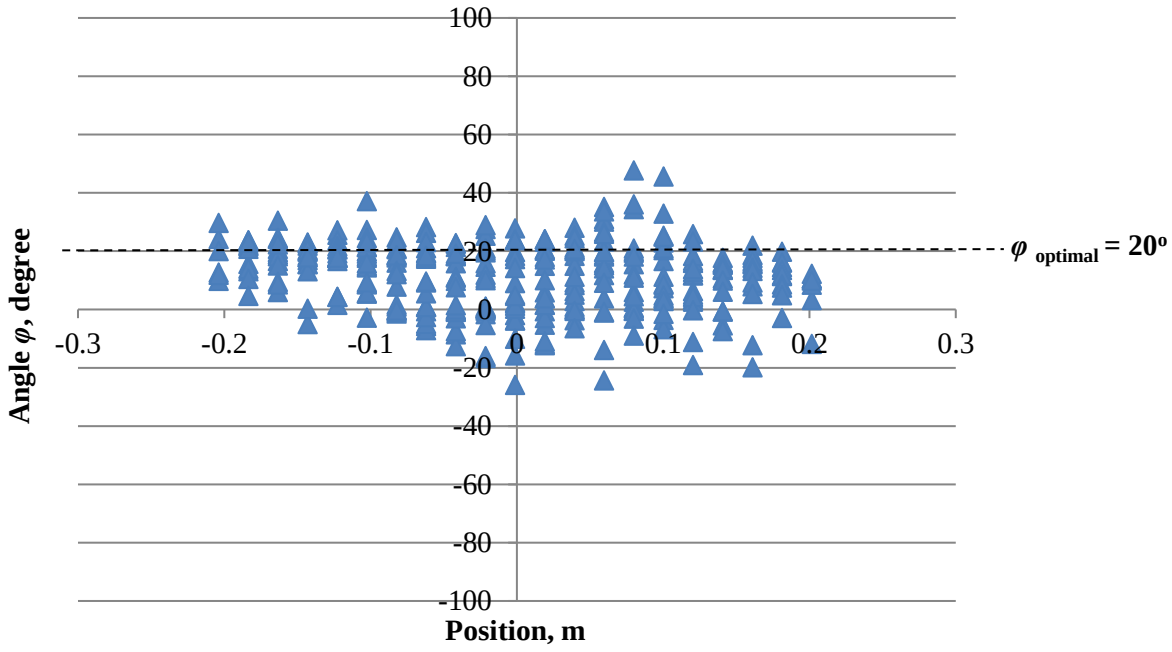

Figure 5.28: Angles of flow directions inside the omni-flow system with the stator.

5.5 Summary

In this chapter, aerodynamics of this wind turbine has been analysed by both the wind tunnel testing and CFD simulations. The CFD model was validated by comparing numerical results with experimental data. It is found that the realisable k-ε turbulence model can be used to study aerodynamics of the proposed wind turbine. Results show that the proposed wind turbine can achieve a maximum power coefficient of approximately 0.17. It is also found that this wind turbine has the good starting capability. In addition, the effects of the stator on the velocity and the direction of the flow have been studied. Results indicate that the stator can improve the flow quality inside the omni-flow system.

Chapter 6 Aerodynamic Features of the Wind Turbine under Non-uniform Flow

As shown in Section 2.3, the flow velocity field inside the omni-flow wind energy system is non-uniform. It is necessary to study aerodynamic features of the wind turbine under non-uniform flow. This chapter presents the aerodynamic analyses of the proposed wind turbine under the non-uniform flow condition by CFD simulations. The setup of simulations has been presented in Chapter 5.

6.1 Wind Turbine Model under Non-uniform Flow

Features of the flow inside the omni-flow wind energy system have been reviewed in Section 2.3.2. A major feature is the non-uniform velocity distribution. Figure 6.1(a) shows the flow velocity distribution at the outlet of the omni-flow system when the free-stream wind is at 0^o to the omni-flow system. As shown in Figure 6.1(b), the flow velocity distribution at the outlet can be divided into two regions: high velocity region and low velocity region. The high velocity region occupies 20% of the outlet area. The low velocity region occupies 80% of the outlet area. The average velocity in the low velocity region is close to zero and much smaller than that in the high velocity region. Hence, the flow in the low velocity region can be treated as zero to reduce the complexities of analyses. In order to simulate these two different velocity regions, a cover was added in front of the wind turbine model in simulations as shown in Figure 6.2(a). The cover has a 20% entrance area corresponding to the high velocity region. Thus, with the aid of this cover, the 20% non-uniform flow condition can be created. When the wind is at 36^o to the omni-flow system model, the high velocity region occupies 40% of the outlet area as shown in Figures 6.3. In simulations, the cover has a 40% entrance area that is the same as the high velocity region as shown in Figure 6.2(b).

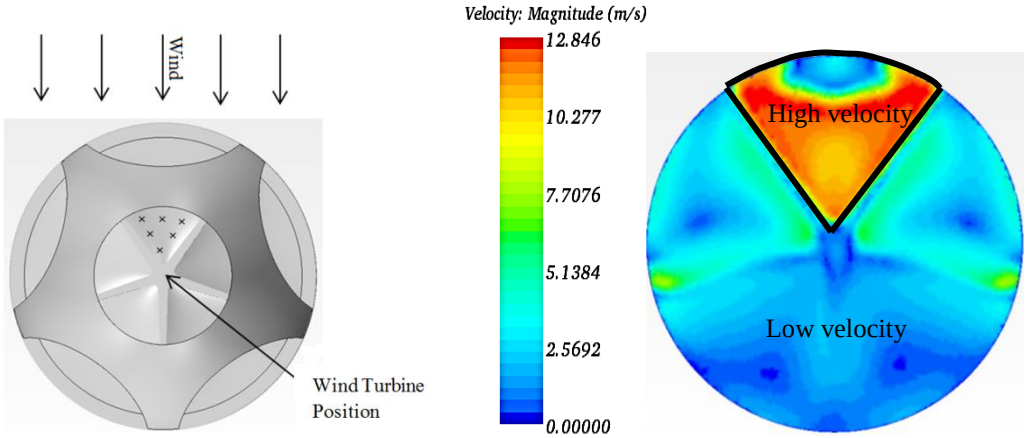

(a) (b)

Figure 6.1: 20% non-uniform flow condition: (a) wind direction; (b) velocity distribution at the outlet of the system.

(a) (b)

Figure 6.2: Wind turbine models: (a) for 20% non-uniform flow condition; (b) for 40% non-uniform flow condition.

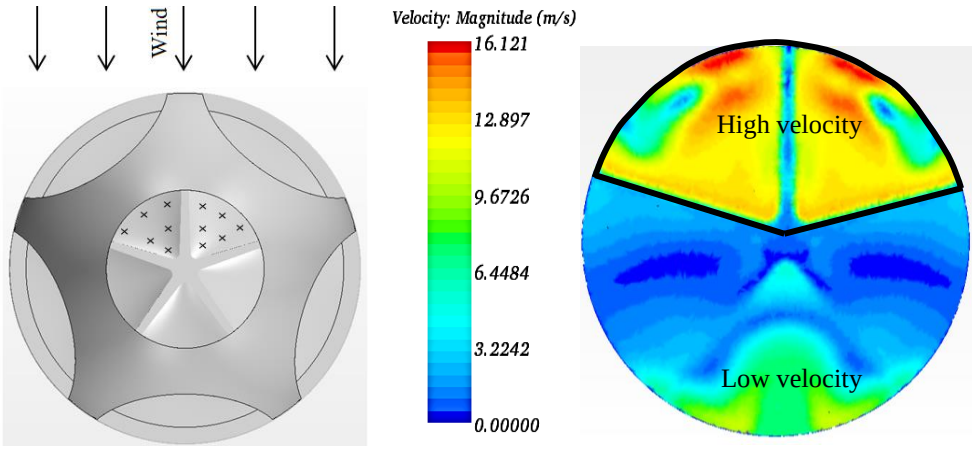

(a) (b)

Figure 6.3: 40% non-uniform flow condition: (a) wind direction; (b) velocity distribution at the outlet of the system.

There are two features about the wind turbine model with an added cover. Firstly, the cover divides the flow into the flow passing region and the non-flow passing region as shown in Figure 6.4. Due to the pressure difference between two regions, air flow may move from the flow passing region to the non-flow passing region. The second feature is that whereby the partial flow is blocked in the axial direction by the cover, a high pressure can be generated in front of the cover, which will accelerate the flow velocity at the entrance. Therefore, a correction about the flow velocity is needed to account for this effect due to the introduction of the cover.

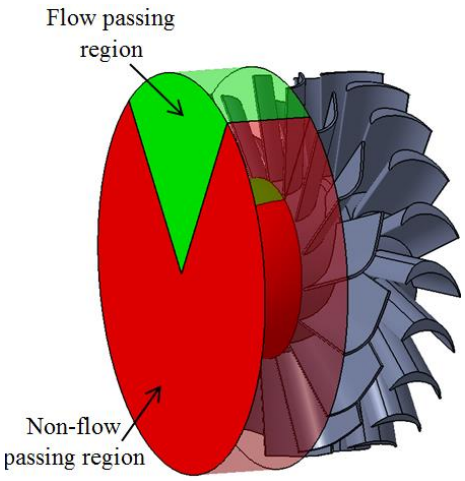

Figure 6.4: Two flow regions caused by the cover ahead the wind turbine.

The correction factor γ is defined as the ratio of the averaged flow velocities between covered and uncovered conditions:

$$\gamma = \frac{U_{covered}}{U_{uncovered}} \tag{6.1}$$

where $U_{covered}$ represents the average flow velocity at the entrance with the cover and $U_{uncovered}$ is the average velocity without the cover. This ratio represents the change of flow velocity due to the cover effect. Table 6.1 lists values of $U_{covered}$ and $U_{uncovered}$ obtained at the free stream velocity of 8.2 m/s. The correction factor is 1.56 for the 20% non-uniform flow

condition and 1.2 for the 40% non-uniform flow condition. Therefore, the corrected flow velocity is 12.8 m/s under the 20% non-uniform flow condition and 9.8 m/s under the 40% non-uniform flow condition. The corrected flow velocities of 12.8 m/s and 9.8 m/s have been used in calculations of power, torque and thrust coefficients under the non-uniform flow condition.

Table 6.1: Values of $U_{covered}$ and $U_{uncovered}$ under different rotational speeds.

Rotational speed, rpm	100 rpm	200 rpm	300 rpm	400 rpm
$U_{uncovered}$	3.4 m/s	3.39 m/s	3.34 m/s	3.31 m/s
$U_{covered}$ under 20% entrance area	5.3 m/s	5.27 m/s	5.22 m/s	5.18 m/s
Average γ under 20% entrance area	1.56			
$U_{covered}$ under 40% entrance area	4.12 m/s	4.1 m/s	4.07 m/s	4.03 m/s
Average γ under 40% entrance area	1.2			

6.2 Power Coefficient and Torque Coefficient

Power coefficient (C_P) and torque coefficient (C_T) of this wind turbine under the non-uniform flow condition are analysed in this section to evaluate its performance. As shown in Figure 6.5, the wind turbine under the non-uniform flow condition has the value of the maximum C_P in a range of 0.06 – 0.126 which is lower than the maximum C_P of 0.17 under the uniform flow condition. Figure 6.6 shows the distributions of torque coefficients under the non-uniform flow condition. The 40% entrance area results in the higher power coefficient and torque coefficient compared with the 20% entrance area. It can be seen that the value of the maximum C_T is in a range of 0.4 – 0.6 that is lower than 0.7 of the proposed wind turbine under the uniform flow condition, but higher than 0.1 of conventional wind turbines [52].

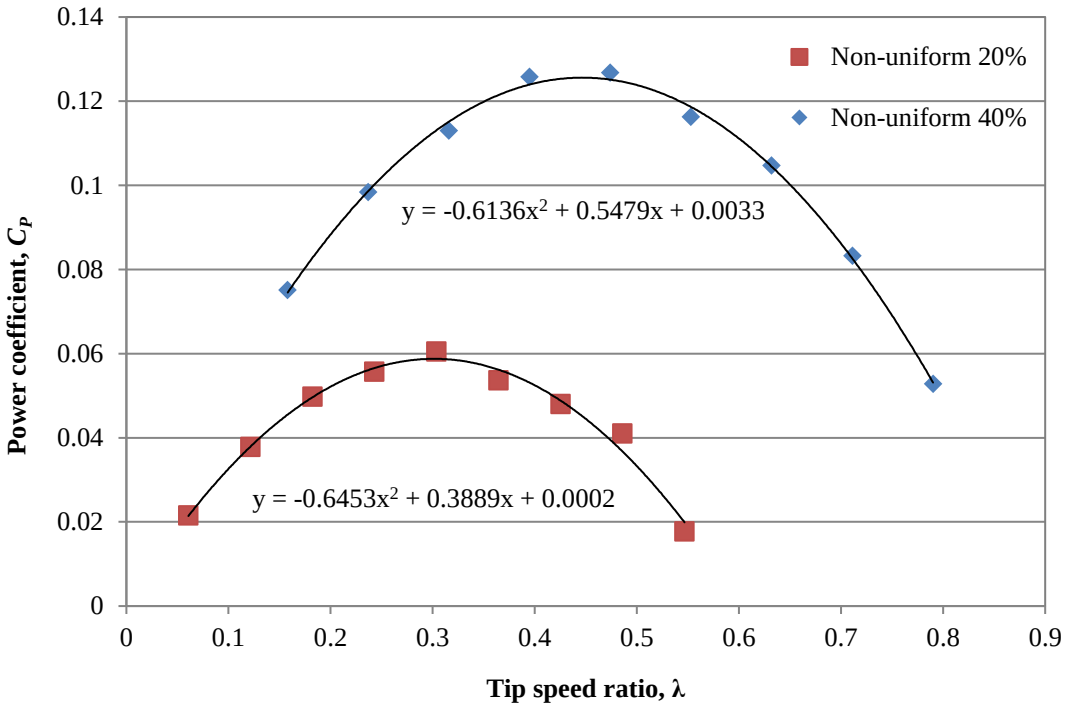

Figure 6.5: Distributions of power coefficient under two non-uniform flow conditions.

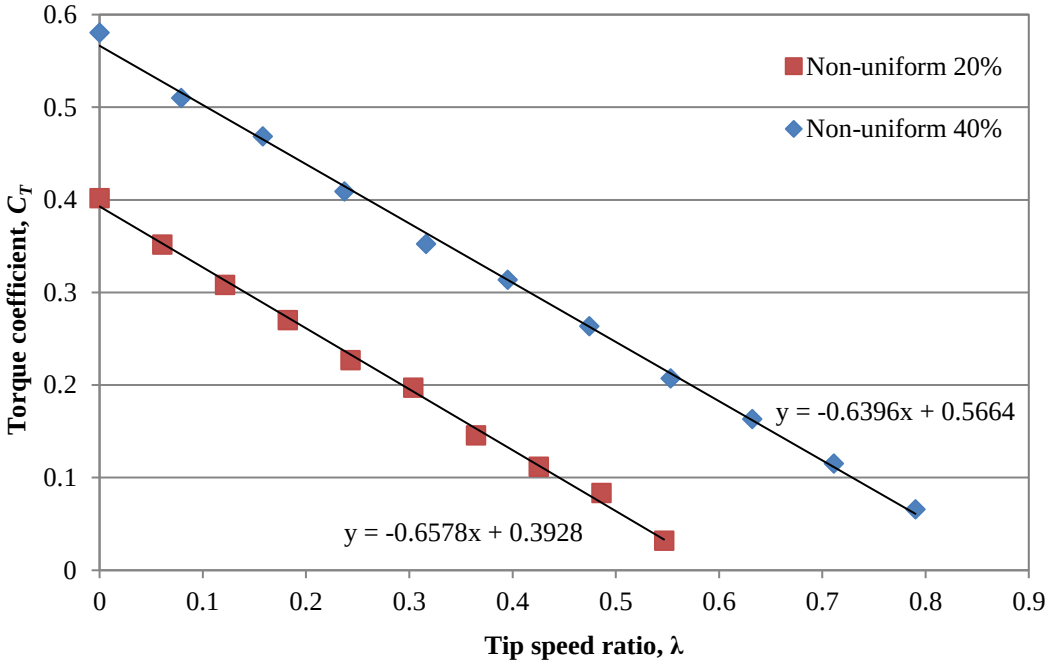

Figure 6.6: Distributions of torque coefficient under two non-uniform flow conditions.

Due to the non-uniform flow, the torque distribution on blades is also non-uniform. Figure 6.7 shows the torque value on each blade under the 20% non-uniform flow condition. It can be

seen that blades (No.3 – No.8) in the flow passing region have much greater torque values than other blades. A blade in the flow passing region can produce larger torque than that in the non-flow passing region. Results indicate that blades in the flow passing region have the greater contribution to the overall torque of the wind turbine. Figure 6.7 also shows some blades (No.10 – No.20) in the non-flow passing region generate negative torque or negligible torque which lowers the overall performances of the wind turbine.

Figure 6.8 shows the torque value on each blade under the 40% non-uniform flow condition. Compared with the wind turbine under the 20% non-uniform flow condition, the wind turbine under the 40% non-uniform flow condition has more blades (No.3 – No.12) to produce large torque as more blades are rotating in the flow passing region. Therefore, it results in the higher power and torque coefficients as shown in Figures 6.5 – 6.6. Figure 6.8 also shows that the blades (No.14 – No.20) produce negative torque or negligible torque as these blades are rotating in the non-flow passing region.

It is worth noting that six blades (No.3 – No.8) can produce high positive values of torque as shown in Figure 6.7 while only four blades of the wind turbine are directly exposed to the flow under the 20% condition as shown in Figure 6.2(a). The reason is that the flow moves from the flow passing region to the non-flow passing region due to the pressure difference between two regions. A similar phenomenon can be observed in Figure 6.2(b) and Figure 6.8.

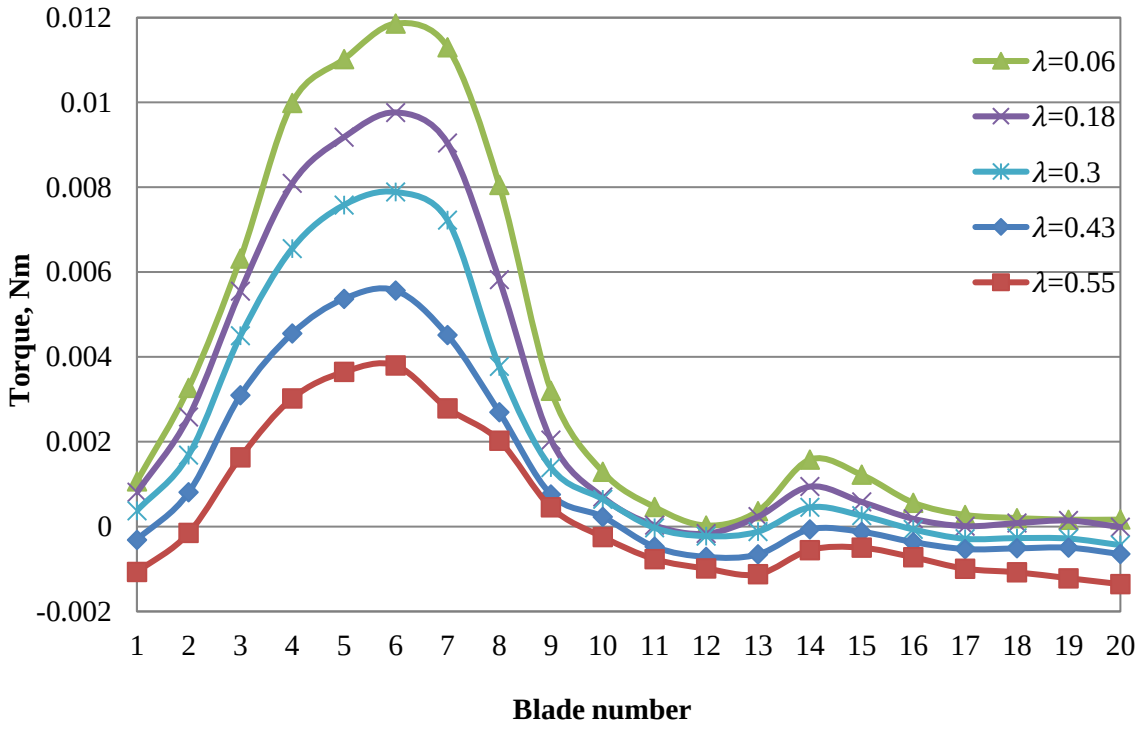

Figure 6.7: Torque generated on every blade under the 20% non-uniform flow condition.

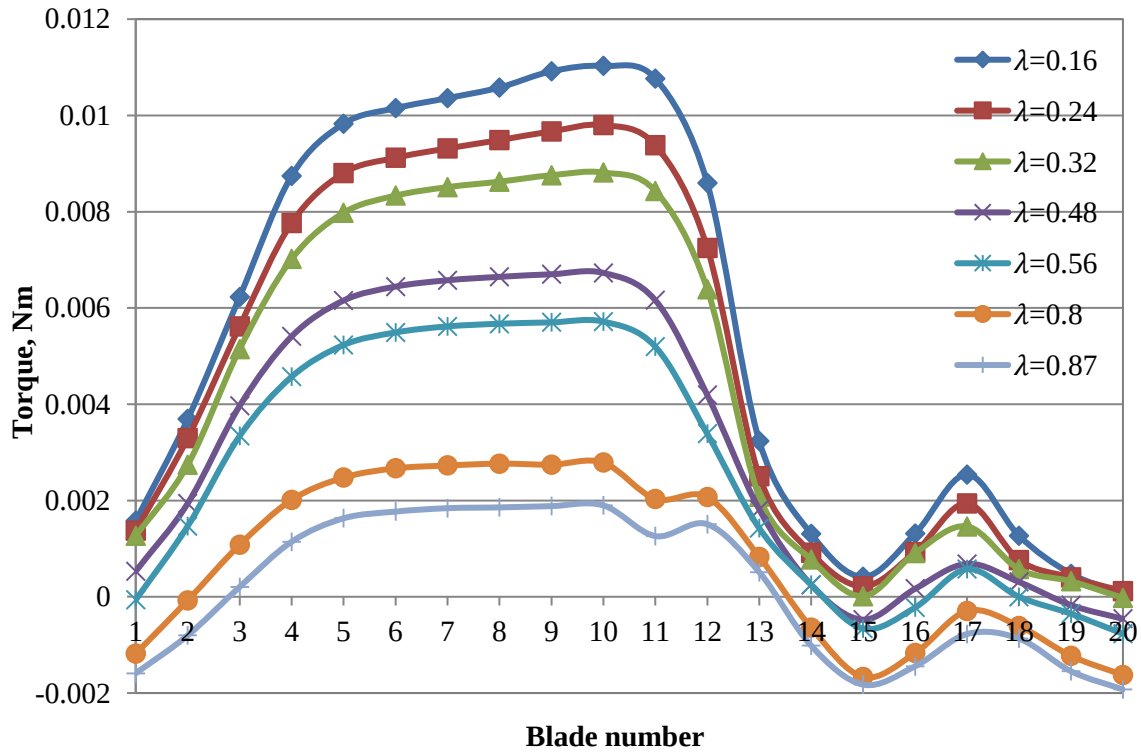

Figure 6.8: Torque generated on every blade under the 40% non-uniform flow condition.

The distribution of pressure coefficients on the aerofoil in the flow passing region is compared with that in the non-flow passing region in Figure 6.9. No.6 blade is in the flow passing region and No.16 is in the non-flow passing region. It can be seen that No.6 blade has a much larger positive area about pressure coefficient than No.16 blade. Therefore, the normal force produced by No.6 blade is larger than that by No.16 blade. Figure 6.9 indicates that the different distributions of pressure cause different torque values on blades as shown in Figures 6.7 – 6.8.

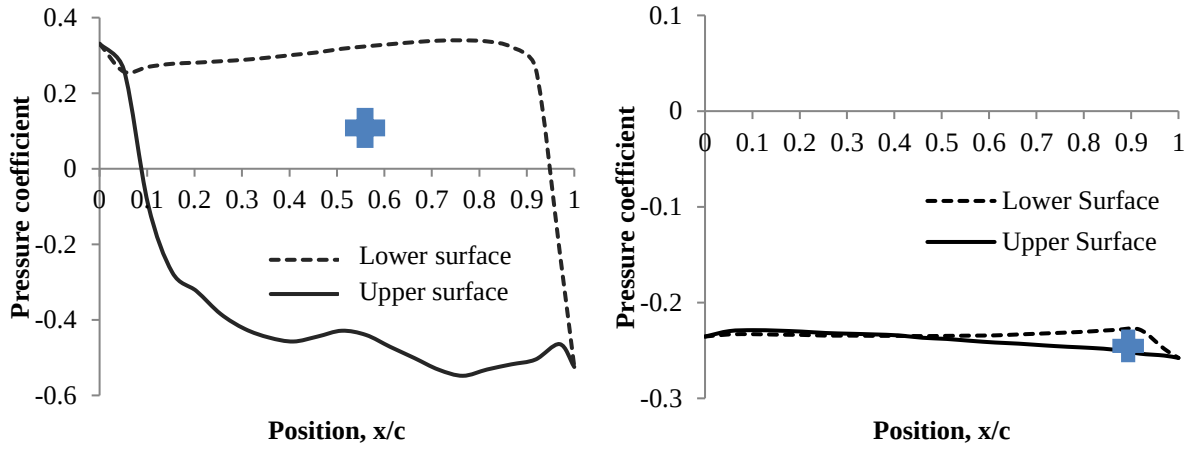

Figure 6.9: Pressure coefficient distributions at r = 140 mm and λ = 0.3 under the 20% non-uniform flow condition: (a) No. 6 blade; (b) No. 16 blade.

6.3 Thrust

The thrust distribution of the proposed wind turbine has been studied. Thrust is a part of the aerodynamic force and acting in the axial direction. This study shows influences of the non-uniform flow on the thrust distribution, which is helpful in understanding aerodynamics of the proposed wind turbine.

Thrust on each blade under the non-uniform flow condition is shown in Figures 6.10 – 6.11. Figure 6.10 indicates that blades (No.3 – No.8) in the flow passing region have larger thrust

values than other blades in the non-flow passing region. Thrust can generate a bending moment on a blade. Considering small values of thrust on each blade, the generated bending moments will however be fairly small to affect the integrity of the blade structure.

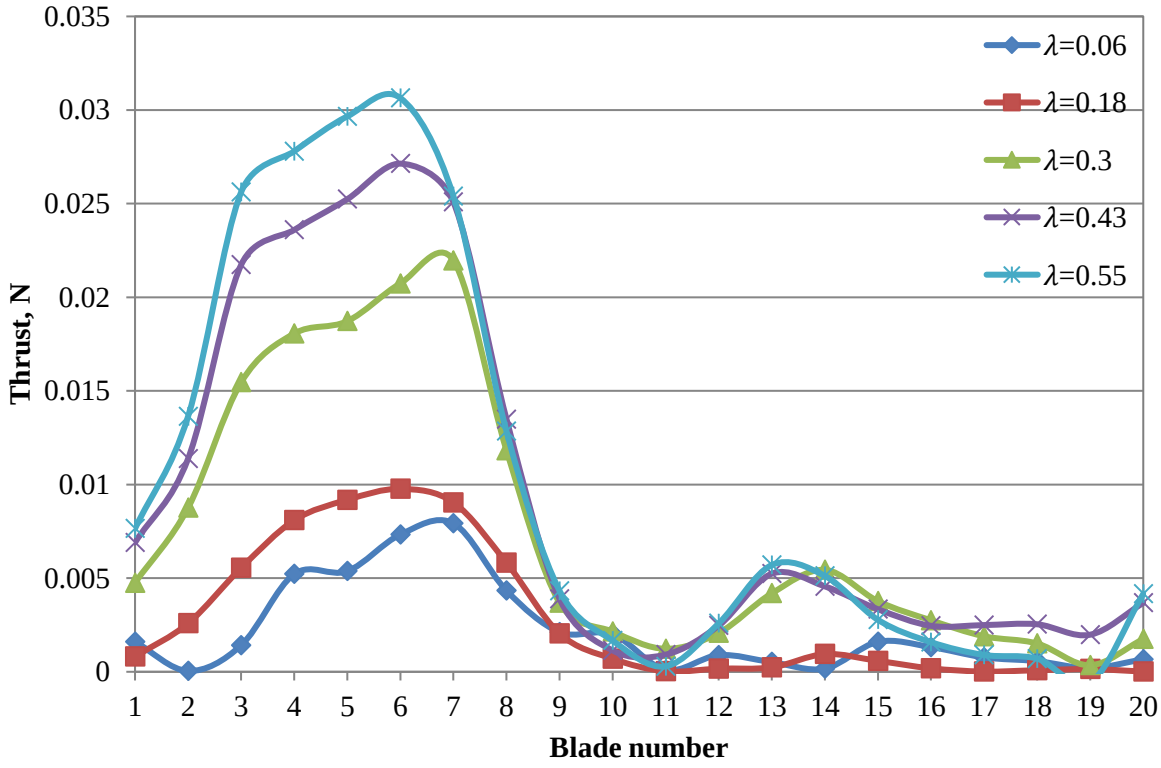

Figure 6.10: Thrust on every blade under the 20% non-uniform flow condition.

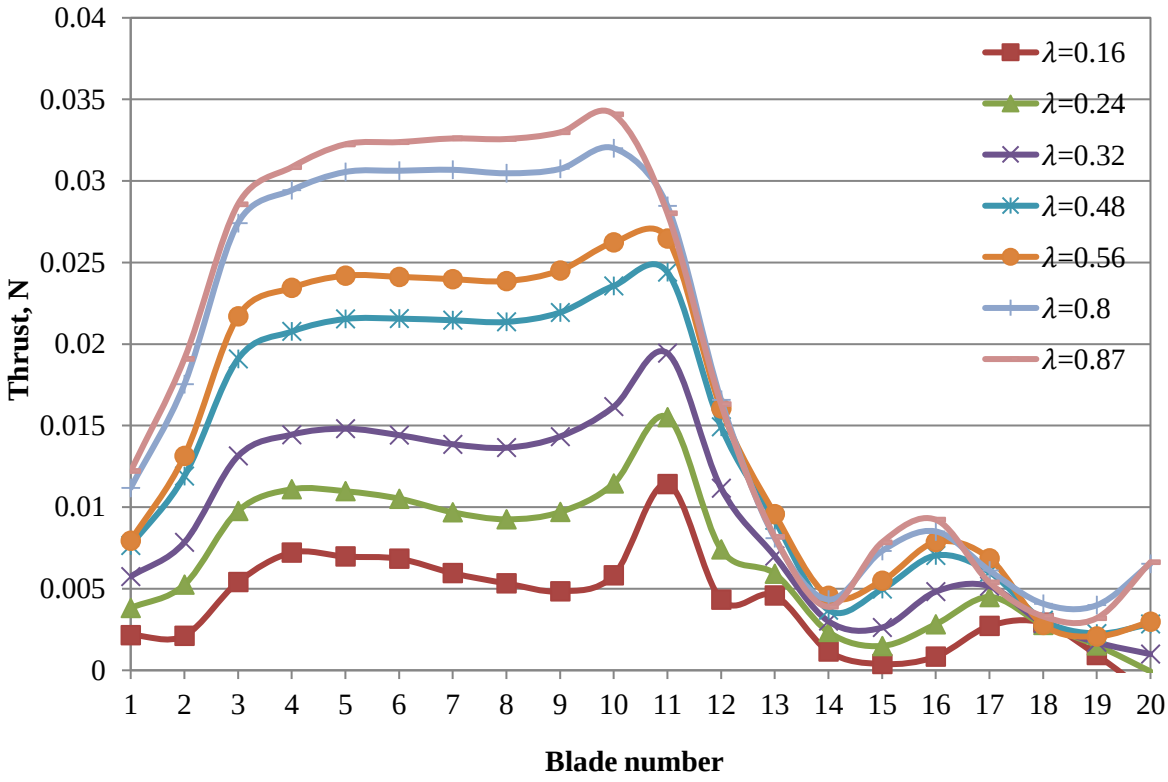

Figure 6.11: Thrust on every blade under the 40% non-uniform flow condition.

Results in Figures 6.10 – 6.11 indicate that thrust has a change during one operation cycle, that is that thrust increases up to the peak value and then decreases. The frequency of the change of thrust, *f*, can be calculated as

$$f = 2 \times \frac{N}{60} \tag{6.2}$$

where *N* is the rotational speed.

Based upon results in Figure 6.5, the rotational speed at the maximum C_P is 250 rpm under the 20% non-uniform flow condition. Therefore, the frequency of the thrust change is approximately 8 Hz. When the wind turbine operates under the 40% non-uniform flow condition, the wind turbine works with higher rotational speeds. Hence the frequency of the thrust change is about 10 Hz.

Considering the definition of tip speed ratio,

$$\lambda = \frac{\frac{N}{60} \times 2\pi \times R}{U} \tag{6.3}$$

the relationship between the thrust change frequency and the rotor radius can be given as

$$f = \frac{\lambda \times U}{\pi \times R} \tag{6.4}$$

Equation 6.4 states that the frequency of thrust change decreases with increasing the rotor radius under a constant wind speed. When the wind turbine has a rotor radius of 1 m, the frequency of thrust change will be decreased to 1.2 Hz under the 20% condition and 1.5 Hz under the 40% condition as listed in Table 6.2. It can be seen that such changes of frequencies of thrust are marginal. The maximum value of thrust on a blade for the wind turbine is also given in Table 6.2.

Table 6.2: Predicted maximum thrust and frequency with different radii.

Case at 8.2 m/s	λ	f at R = 0.15 m	f at R = 1 m	Thrust at R = 0.15 m	Thrust at R = 1 m
20% entrance area	0.3	8 Hz	1.2 Hz	0.022 N	1.3 N
40% entrance area	0.47	10 Hz	1.5 Hz	0.025 N	1.1 N

6.4 Summary

Aerodynamic performances of the proposed wind turbine under the non-uniform flow condition have been analysed in this chapter. The non-uniform flow results in poor performances of the wind turbine. It is found that the maximum C_P is in a range from 0.06 to 0.12 and that the maximum C_T is in a range of 0.4 – 0.6. The larger the entrance area of the non-uniform flow is, the higher the power coefficient and torque coefficient will be. It is found that the torque distribution is non-uniform on blades. The blade in the passing flow

region has the larger torque than that in the non-flow passing region. It is also found that the non-uniform flow can result in a periodical change of thrust on a blade in one operation cycle. The frequency of the thrust change is in a range from 8 Hz to 10 Hz for the proposed wind turbine. It is however worth nothing that the frequency of the thrust change depends on the size of the turbine. If the wind turbine employs a larger blade radius of 1 m, the frequency can reduce to approximately 1 Hz.

Chapter 7 Influences of Geometrical Parameters on Aerodynamics of the Wind Turbine

7.1 Introduction

Compared with conventional wind turbines, the proposed wind turbine has several exclusive geometrical features which include the large hub-to-tip ratio, more blades, and the special blade aerofoil and guide vanes. This chapter analyses influences of these geometrical parameters on the power out, torque and thrust of the wind turbine by the CFD approach. The computational setup has been presented in Chapter 5. All simulations in this chapter have an identical free stream velocity of 8.2 m/s.

7.2 Effects of Hub-to-tip Ratios

The proposed wind turbine has a large hub based upon the impulse turbine technology. The dimensionless hub-to-tip ratio is used to evaluate the effects of the hub size on the aerodynamic performance of the turbine. The hub-to-tip ratio is defined as the ratio between the hub diameter and the wind turbine diameter. Figure 7.1 shows the wind turbine models with three hub-to-tip ratios of 0.35, 0.45 and 0.6, representing the hub diameter of 105 mm, 135 mm and 180 mm, respectively. The blade length is 95.5 mm for the hub-to-tip ratio of 0.35, 80.5 mm for 0.45, and 58 mm for 0.6. As shown in Figure 7.1, the largest hub-to-tip ratio of 0.6 has the shortest blade and the smallest ratio of 0.35 has the longest blade. Because the blade is the component to produce power, performances of the wind turbine will be affected by the hub-to-tip ratio.

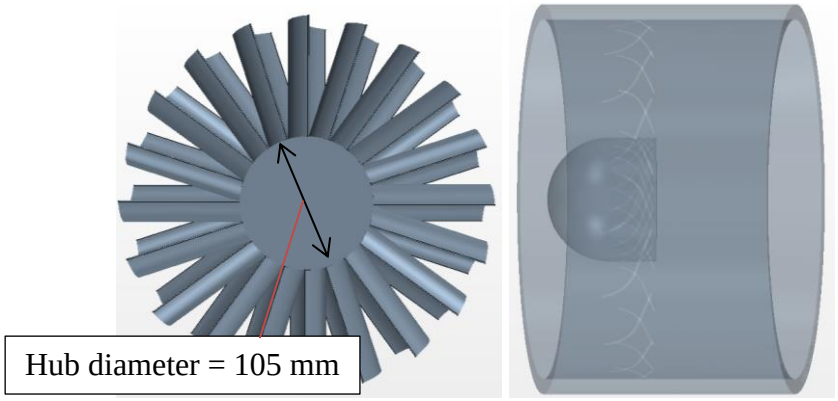

(a)

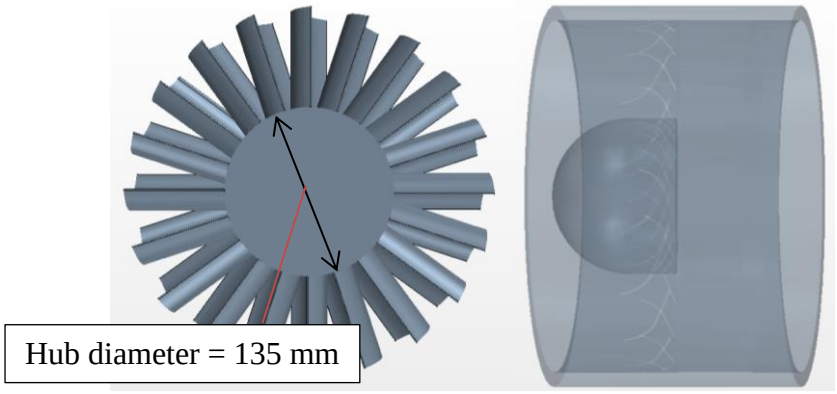

(b)

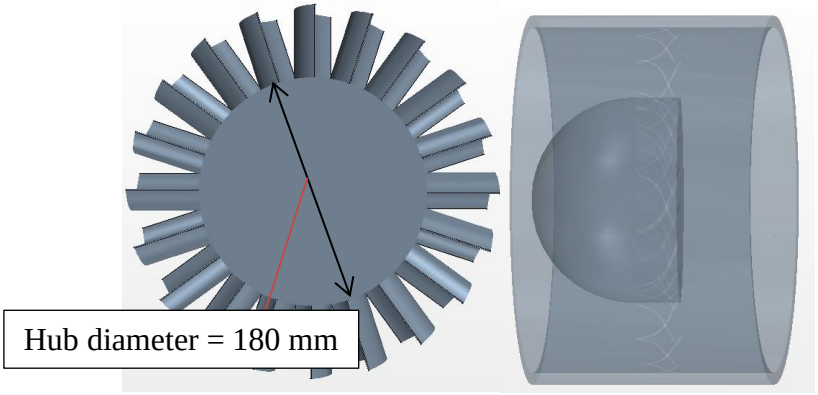

(c)

Figure 7.1: Employed three hub-to-tip ratios and hub diameters in simulations: (a) 0.35; (b) 0.45; (c) 0.6.

Figure 7.2 shows the distributions of the torque per unit length (*dT*) with three hub-to-tip ratios at $\lambda = 0.66$ where the wind turbine has the maximum power coefficient. It is found that for a given blade radius in the range of 90 mm – 140 mm the hub-to-tip ratio of 0.6 has the

smallest value of *dT*, which can result in the lowest power output and torque. Figure 7.2 also shows that the hub-to-tip ratio of 0.35 has a similar distribution of *dT* to the ratio of 0.45. However, the ratio of 0.35 has the negative *dT* in a larger range of r = 55 mm – 80 mm, while the ratio of 0.45 has the negative *dT* in a range of r = 70 mm – 80 mm. Therefore, more negative torque was produced when the hub-to-tip ratio was 0.35.

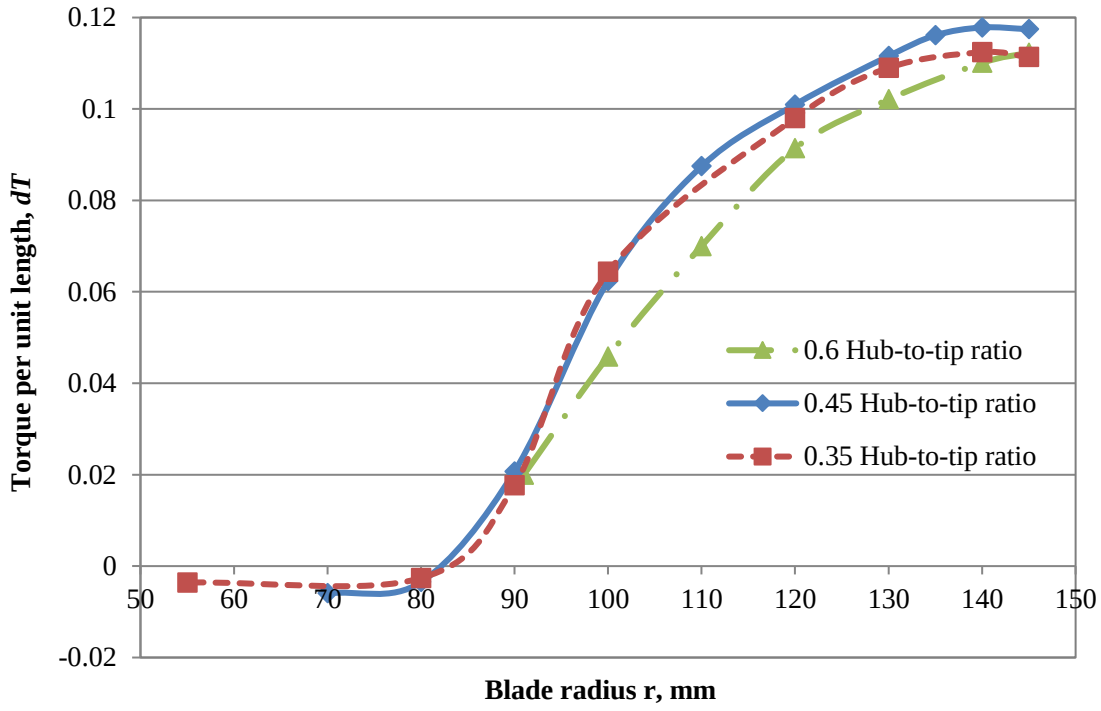

Figure 7.2: Distributions of torque per unit length on the blade with three hub-to-tip ratios at λ = 0.66.

Figure 7.3 shows the distributions of power coefficient at three hub-to-tip ratios. It can be seen that three C_P–λ curves have a similar trend. The hub-to-tip ratio of 0.6 has the lowest power coefficient, which is caused by the lowest *dT* as shown in Figure 7.2. Figure 7.3 indicates that the ratio of 0.45 has the highest power coefficient. And the maximum power coefficient of the ratio of 0.45 is 3.5% higher than that of 0.35. The reason is that the ratio of

0.45 has the smaller range of negative *dT* than the ratio of 0.35 as shown in Figure 7.2. Negative *dT* can reduce the power out of the wind turbine.

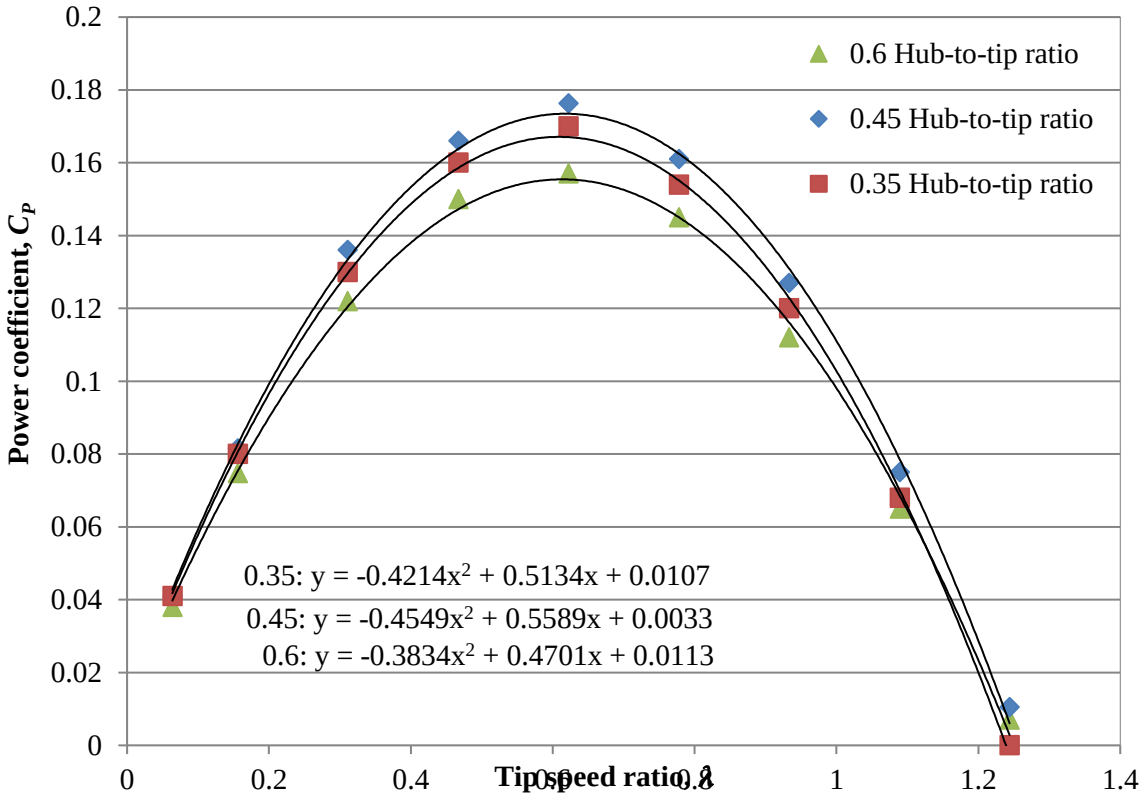

Figure 7.3: Distributions of power coefficient of the proposed wind turbine with three hub-to-tip ratios.

Distributions of torque coefficient with three hub-to-tip ratios are shown in Figure 7.4. For the hub-to-tip ratio varying from 0.35 to 0.6, the maximum torque coefficient is in the range of 0.5 - 0.6 which is higher than 0.1 of conventional wind turbines [52]. As the ratio of 0.6 has the lowest value of the maximum C_T, the starting capability of the wind turbine with the ratio of 0.6 would be the worst among the three ratios concerned.

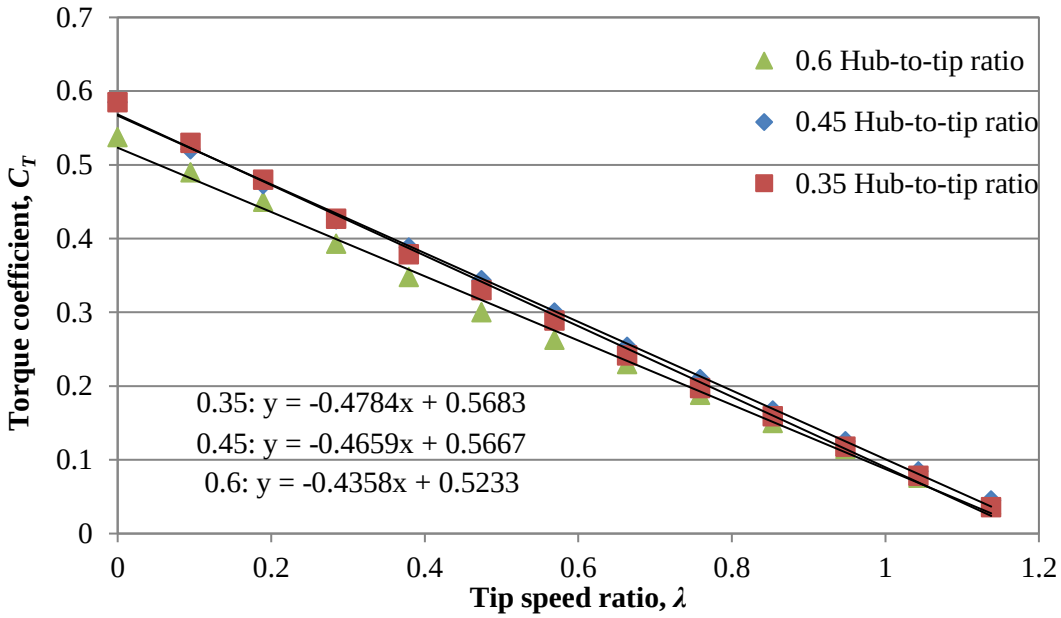

Figure 7.4: Distributions of torque coefficient of the proposed wind turbine with three hub-to-tip ratios.

Figure 7.5 shows that the distribution of thrust coefficient varies with the hub-to-tip ratio. Thrust coefficient consists of a positive component from the blades and a negative component from the rotor hub. As shown in Figure 7.5, at low tip speed ratios (λ) thrust coefficient is negative because the negative thrust component from the rotor hub is dominant in thrust generation. At high λ thrust coefficient is positive as the blades are dominant in thrust generation. The hub-to-tip ratio of 0.6 has the largest negative thrust component from the hub due to the largest hub size, and the smallest positive thrust component from blades due to the shortest blade length. Hence, the hub-to-tip ratio of 0.6 has the lowest thrust coefficient and the hub-to-tip ratio of 0.35 has the highest thrust coefficient as shown in Figure 7.5. The hub-to-tip ratio of 0.45 has the middle thrust coefficient because of the medium hub size and blade length.

When the hub-to-tip ratio is 0.35, the blades have more contribution to thrust than the rotor hub at high λ. However, the negative thrust from hub increases faster than the positive thrust

from blades, which is shown by the concave C_N-λ curve in Figure 7.5. On the other hand, the C_N-λ curve with the hub-to-tip ratio of 0.6 is convex, which indicates that the negative thrust from the hub increases slower than the positive thrust from blades. A regression analysis for three hub-to-tip ratios indicates that C_N rises with the increment of λ, which is similar to the distribution of C_N-λ of a HAWT [18]. The values of maximum C_N of the proposed wind turbine are however lower than that of a HAWT [18].

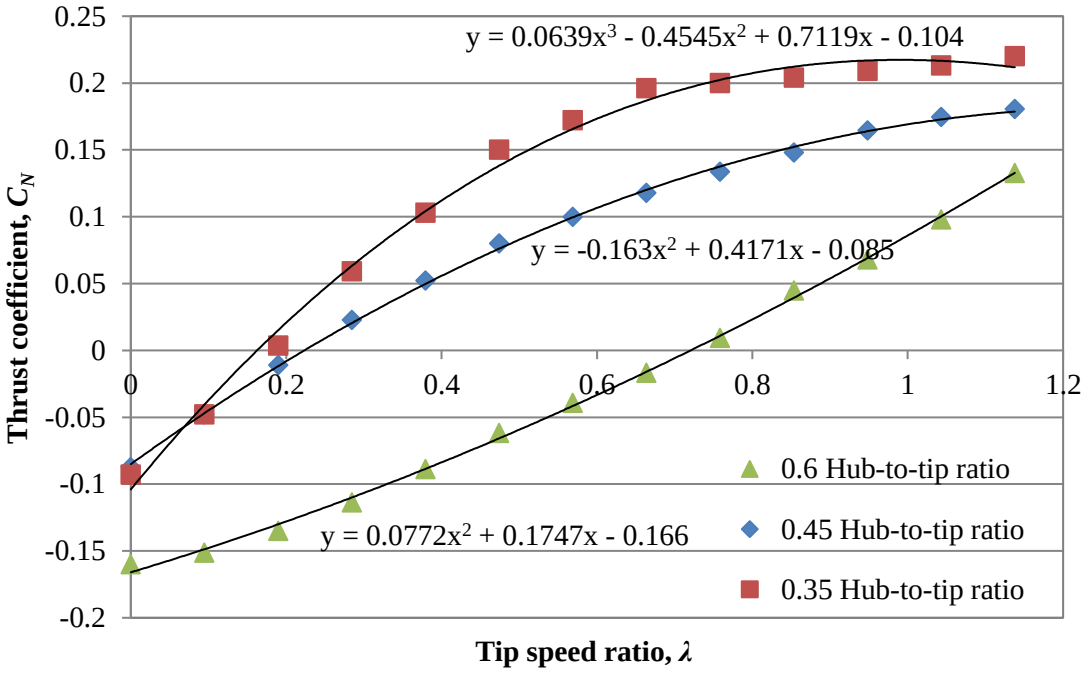

Figure 7.5: Distributions of thrust coefficient of the proposed wind turbine with three hub-to-tip ratios.

7.3 Influences of Blade Numbers

The proposed wind turbine has more blades than a conventional wind turbine. The literature review shows that the blade number is one of most important geometrical parameters for a wind turbine. In order to study influences of the blade number on aerodynamics of the turbine, the wind turbine models with 10, 15, 17, 20, 25 and 30 blades have been simulated. Figure 7.6 shows distributions of power coefficient of turbines with different blade numbers. It can

be seen that the maximum power coefficient has two clear incremental steps of approximately 10% when the blade number has been increased from 15 to 17 and 17 to 20. There is however no significant improvement of the maximum power coefficient when the blade number is 20 or over.

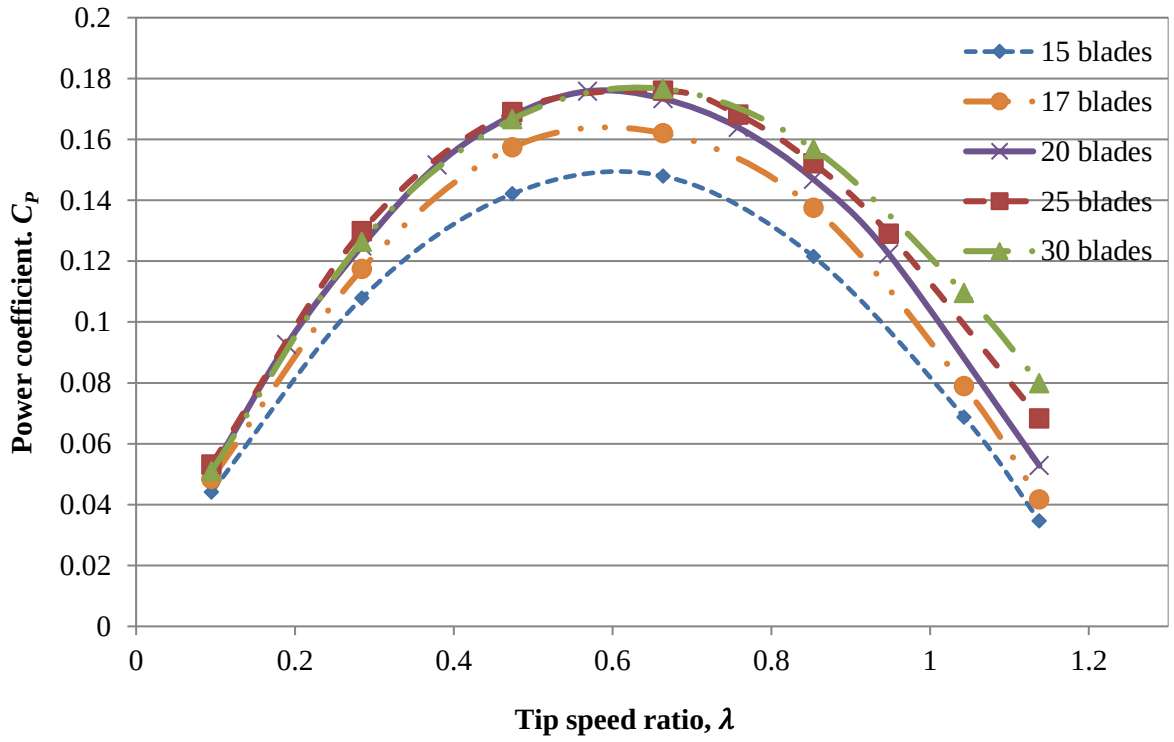

Figure 7.6: Distributions of torque coefficient of the proposed wind turbine with different blade numbers.

Distributions of pressure coefficient on the aerofoil are shown in Figure 7.7 when the numbers of blades are 15 and 30. The enclosed area (marked by +) in Figure 7.7 represents the positive normal force generated on the blade aerofoil. A comparison of the positive areas in Figure 7.7(a) and Figure 7.7(b) indicates that the positive normal force with the blade number of 15 is larger than that with the blade number of 30. Meanwhile, with the blade number of 30, a large negative area (marked by -) that represents the negative normal force can be found in Figure 7.7(b). This is caused by the narrow space between blades which

limits the flow moving when the wind turbine has more blades. Thus the normal force with the blade number of 15 is larger than that with 30. The power output from each individual blade decreases with the increase of the number of blades. The turbine with 15 blades however has the lowest power coefficient as shown in Figure 7.6 as the turbine has the least number of blades to produce power although power generated from each individual blade is higher.

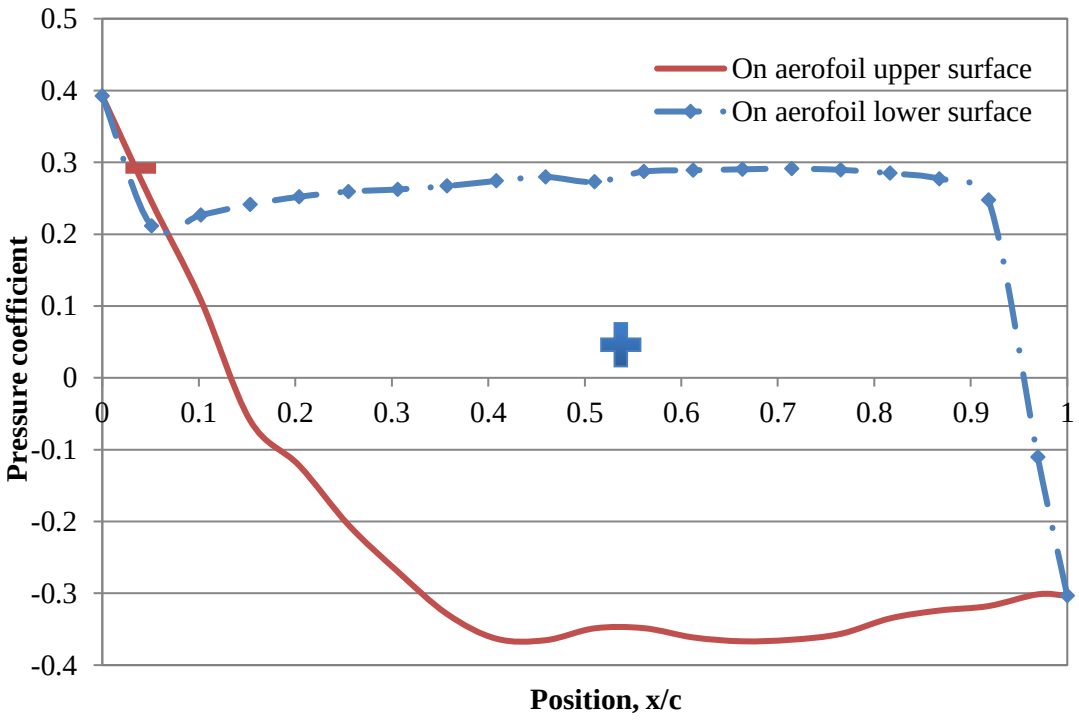

(a)

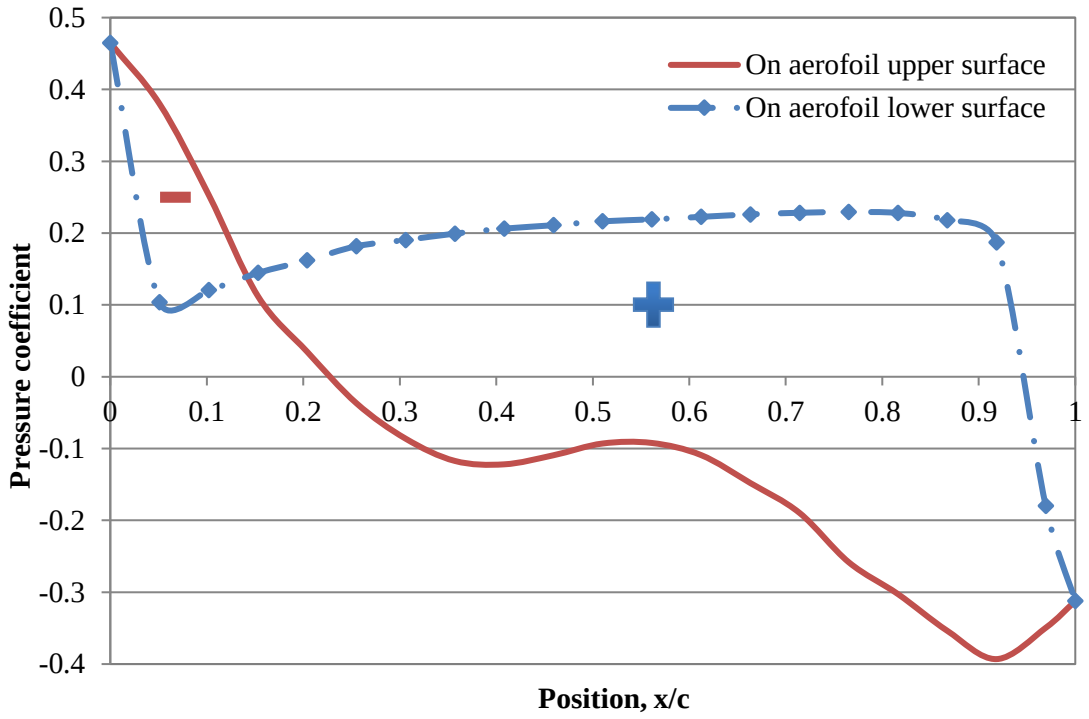

(b)

Figure 7.7: Distributions of pressure coefficient on the blade aerofoil at r = 140 mm: (a) the wind turbine with 15 blades; (b) the wind turbine with 30 blades.

Figure 7.8 shows the relationships between the torque coefficient and the tip speed ratio for the wind turbines with different blade numbers. Values of the maximum torque coefficients are in the range of 0.5 to 0.6 which is higher than that of a conventional wind turbine [52]. Results in Figure 7.8 show that the maximum torque coefficient are increased with more blades. Figure 7.8 indicates that the good starting capability of the wind turbine can be maintained with a change in the blade number.

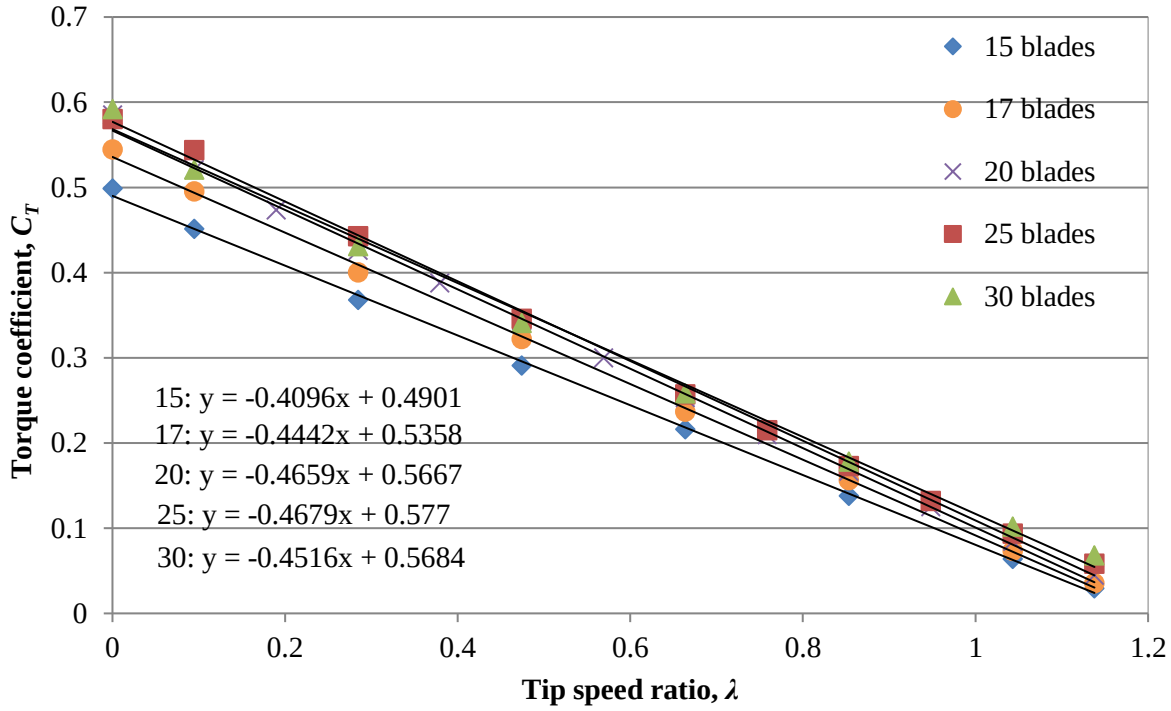

Figure 7.8: Distributions of torque coefficient of the proposed wind turbine with five blade numbers.

Relationships between the thrust coefficient and the tip speed ratio with different blade numbers are shown in Figure 7.9. It can be seen that the thrust coefficient increases with the number of blades. It is known that a wind turbine with a larger solidity can produce a higher thrust coefficient [18]. The solidity of a wind turbine is defined as

$$\sigma = \frac{B}{2\pi}\frac{c}{R} \tag{2.7}$$

where B is the blade number, c is the blade chord and R is the blade radius. Compared with the solidity of 0.1 of a conventional wind turbine, this wind turbine has the large solidity of 1.08 for 15 blades, 1.2 for 17 blades, 1.38 for 20 blades, 1.67 for 25 blades and 1.96 for 30 blades. This wind turbine has the large solidity, but the obtained maximum thrust coefficient in Figure 7.9 is smaller than that of a conventional wind turbine [18]. This is related to the low tip speed ratios of the turbine. Thrust increases with larger tip speed ratios but the

maximum tip speed ratio of this wind turbine is one fifth of that of a conventional wind turbine [18]. Figure 7.9 also shows how different blade numbers influence the C_N -λ relationship. It can be seen that C_N rises much quicker for the wind turbines with 25 blades and 30 blades compared with turbines of 20 blades or less.

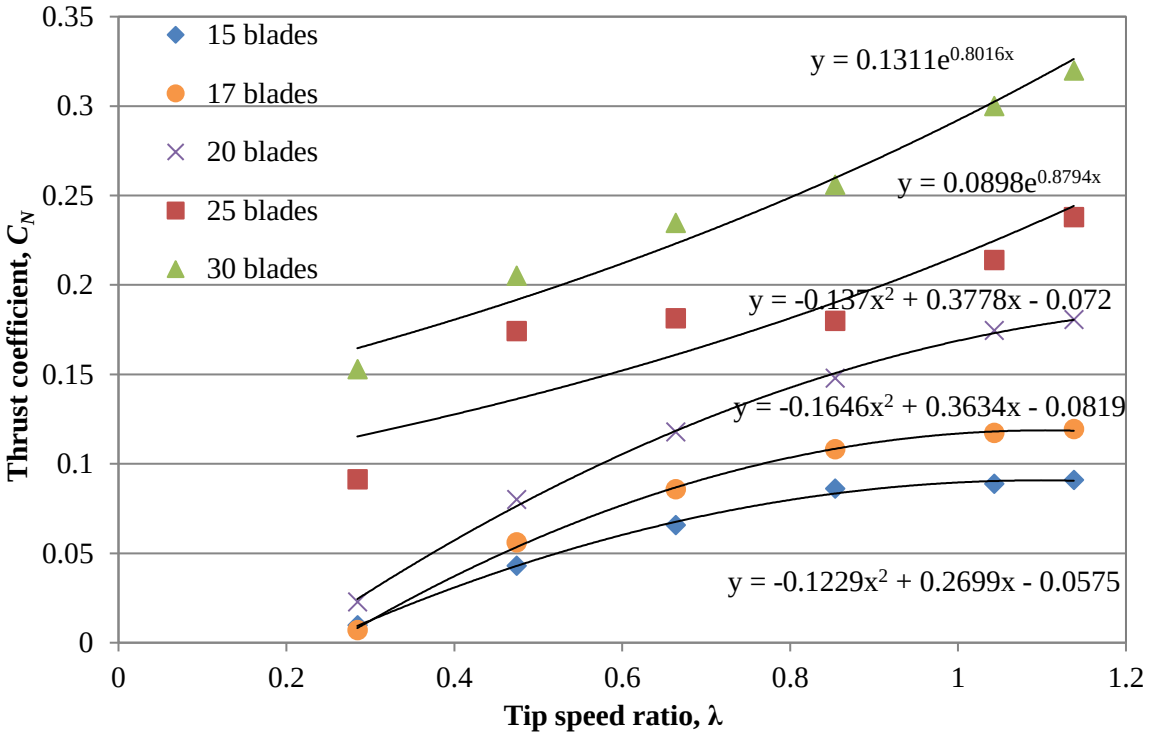

Figure 7.9: Distributions of thrust coefficient of the proposed wind turbine with five blade numbers.

7.4 Effects of Aerofoil Profiles

Analyses in Chapter 5 have shown that there is a negative pressure difference on the leading edge of the aerofoil. The negative pressure difference can result in a negative normal force and lower power output. Hence, there is the potential to improve the power performance by changing the leading edge profile of the aerofoil. In this section, aerodynamic performances

of the wind turbines with three aerofoils are compared. A schematic view of three aerofoils with different leading edges is shown in Figure 7.10. Coordinates of three aerofoils can be found in Appendix D.

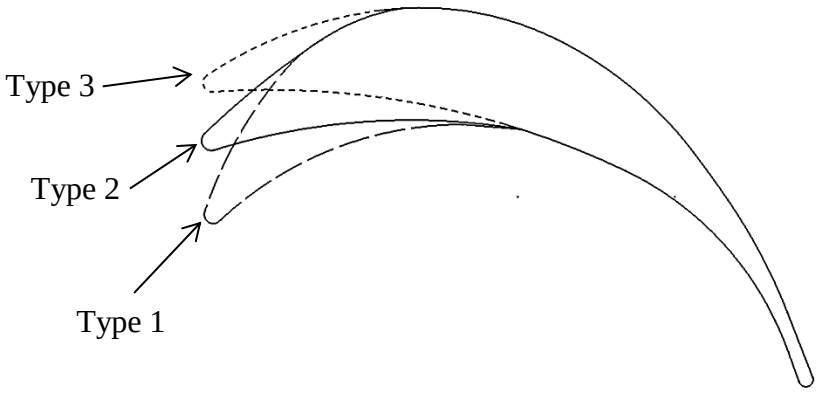

Figure 7.10: Schematic view of three blade aerofoils employed.

Figure 7.11 shows the power coefficient distributions of three aerofoils. It can be seen that the aerofoil change does not affect the power coefficient distributions when the tip speed ratio is less than 0.6. And there are slight improvements on the maximum power coefficient for all three aerofoil profiles. However, when the tip speed ratio exceeds 0.6, the power coefficient is increased by 12% and 25% when Type 1 is replaced by Type 2 and Type 3 aerofoil, respectively. It means that changing the leading edge can improve the power output performance at high tip speed ratios ($\lambda > 0.6$). Figure 7.11 also shows that Type 1 aerofoil has a λ range of 0.4 - 0.76 where the power coefficient exceeds 0.16. When using Type 3 aerofoil, the λ range is 0.4 - 0.9 which is 38.9 % wider. The wider λ range means that the wind turbine can produce power in a wider range of wind speeds.

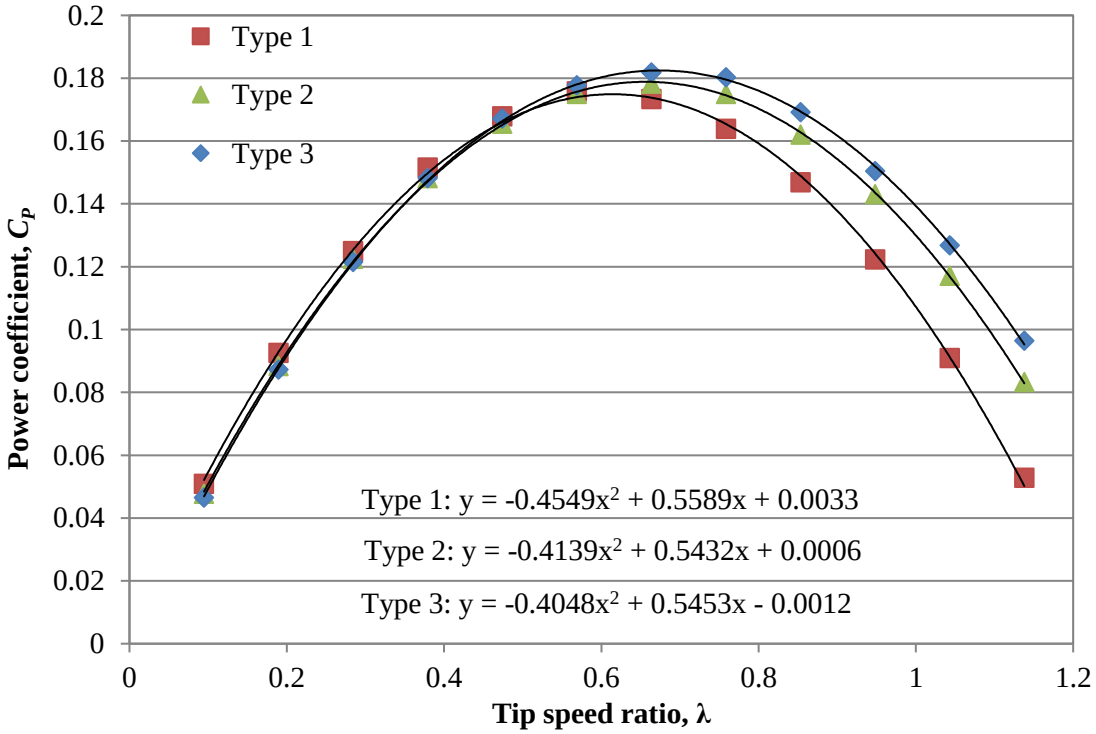

Figure 7.11: Distributions of power coefficient of the proposed wind turbine with three aerofoils.

Figure 7.12 shows distributions of pressure coefficient with different aerofoils at λ = 0.76 where the difference about C_P is significant. It can be seen that the enclosed area (marked by −) representing the negative normal force decreases when Type 1 is replaced by Type 2. There is no negative area (−) when Type 3 is used, meaning that no negative force is generated on Type 3 aerofoil. Hence, the wind turbine with Type 3 aerofoil has the best power performance at high λ (shown in Figure 7.11).

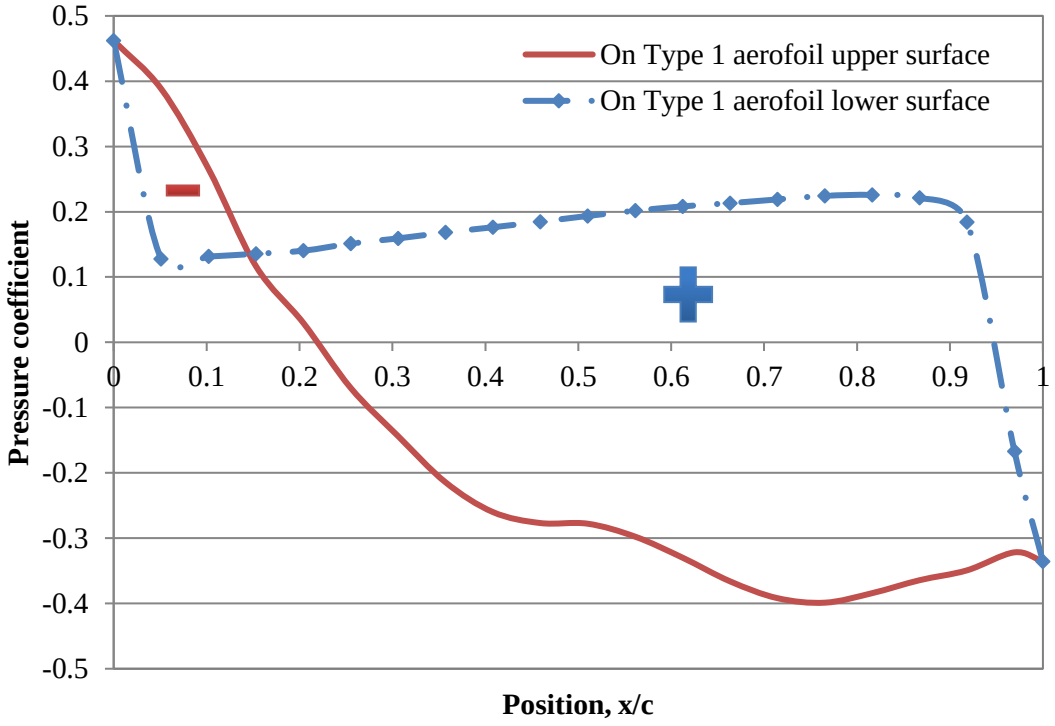
On Type 1 aerofoil upper surface
On Type 1 aerofoil lower surface
Pressure coefficient
Position, x/c
0.5
0.4
0.3
0.2
0.1
0
-0.1
-0.2
-0.3
-0.4
-0.5
0
0.1
0.2
0.3
0.4
0.5
0.6
0.7
0.8
0.9
1

(a)

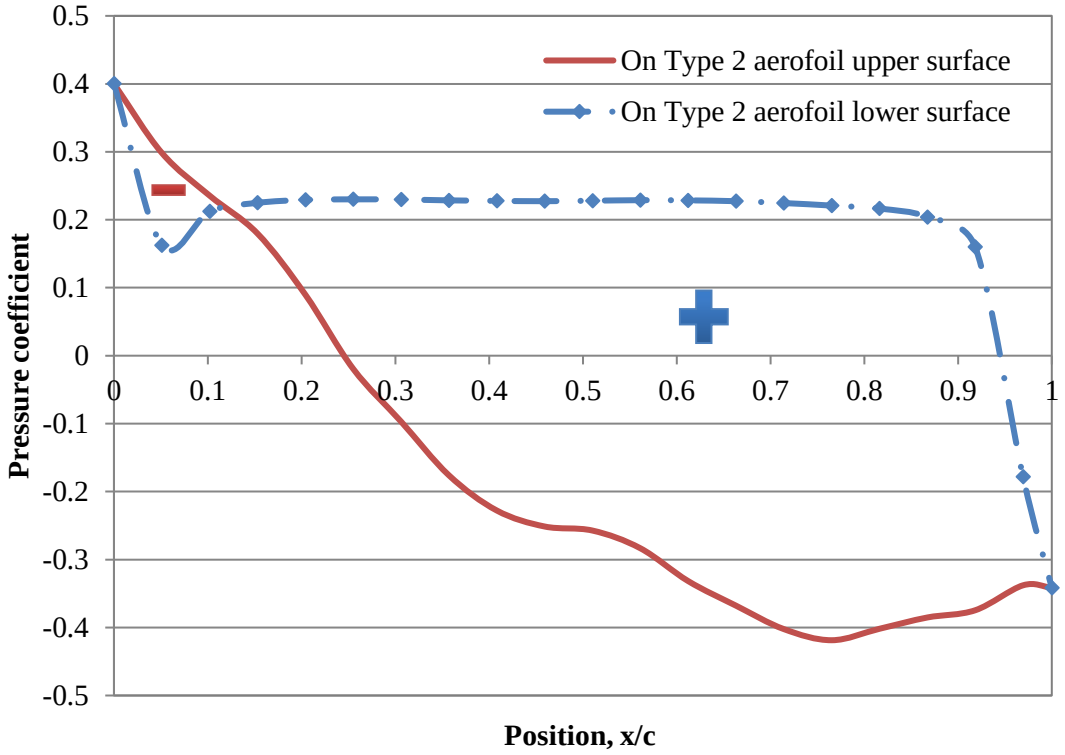
On Type 2 aerofoil upper surface
On Type 2 aerofoil lower surface
Pressure coefficient
Position, x/c
0.5
0.4
0.3
0.2
0.1
0
-0.1
-0.2
-0.3
-0.4
-0.5
0
0.1
0.2
0.3
0.4
0.5
0.6
0.7
0.8
0.9
1

(b)

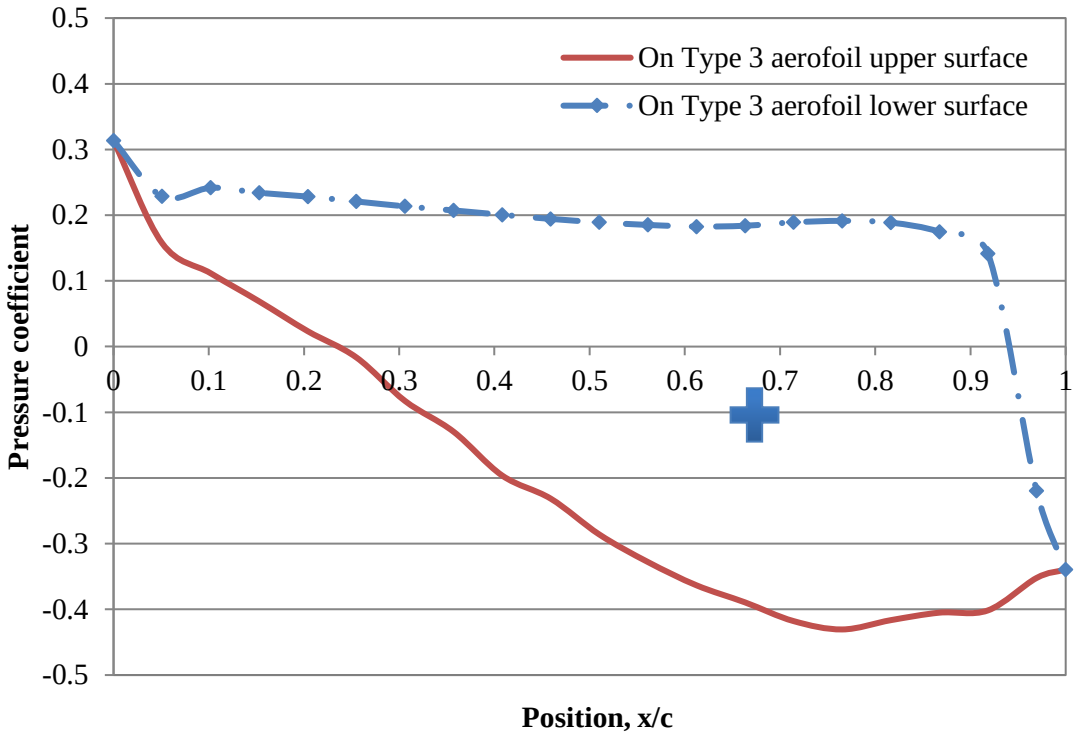

(c)

Figure 7.12: Distributions of pressure coefficient on the blade aerofoil at r = 140 mm: (a) Type 1; (b) Type 2; (c) Type 3.

Figure 7.13 shows distributions of torque coefficient for the three aerofoils. It can be seen that the difference of the torque coefficient among the three aerofoils is not significant. It indicates that the starting capability of three turbines is similar. Regression analysis result in Figure 7.14 shows however that there are two trends about thrust coefficient distributions. For Type 1 aerofoil, thrust coefficient increases steadily. For Type 2 and 3 aerofoils, the thrust coefficient varies over a much narrower band centred around 0.1. A comparison of the two trends in Figure 7.14 demonstrates that the leading edge is an important part in thrust generation.

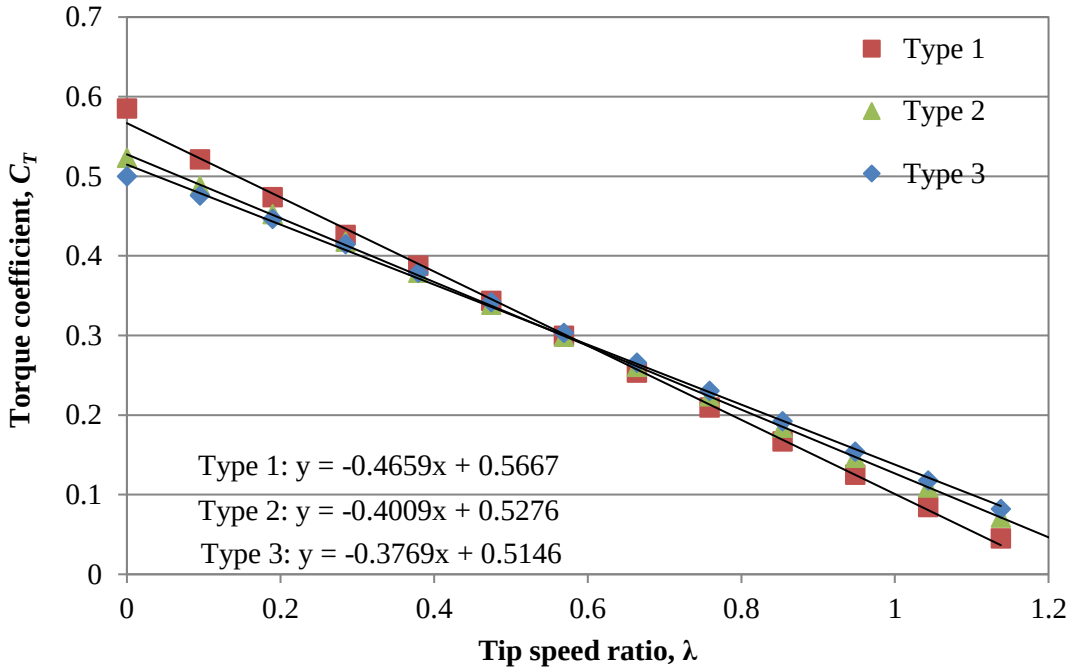

Figure 7.13: Distributions of torque coefficient of the proposed wind turbine with three aerofoils.

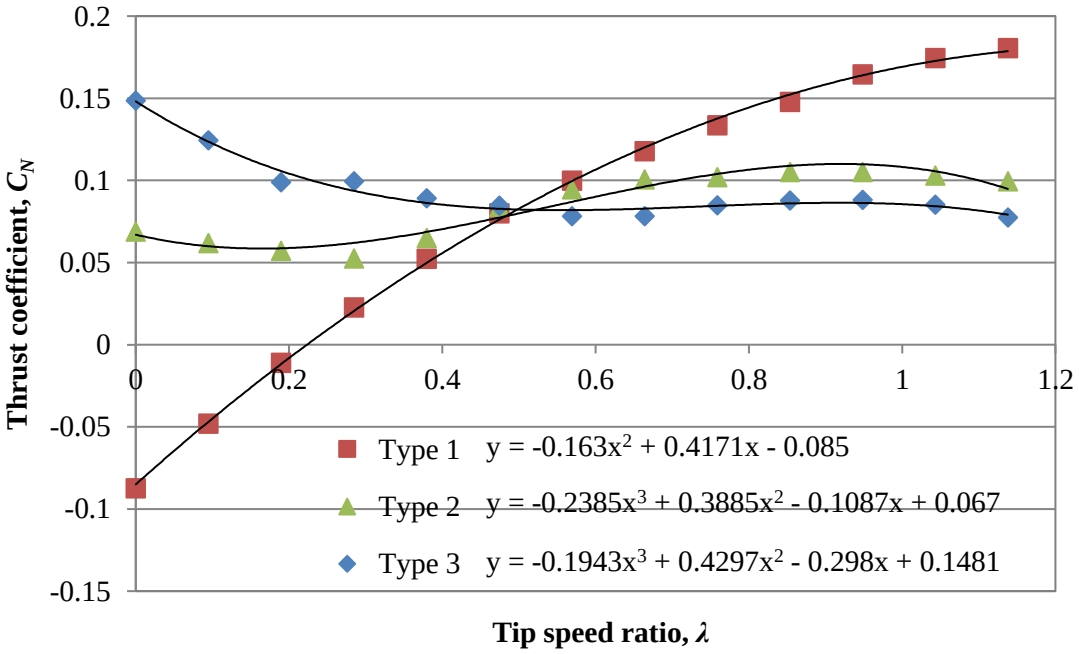

Figure 7.14: Distributions of thrust coefficient of the proposed wind turbine with three aerofoils.

7.5 Influences of Guide Vane Numbers

Analyses in Chapter 5 have shown that the stator affects characteristics of the passing flow. In this section, influences of guide vane numbers on aerodynamic performances of the wind turbine are studied. Figure 7.15 shows the stator models with 5, 10, 15 and 20 guide vanes, respectively.

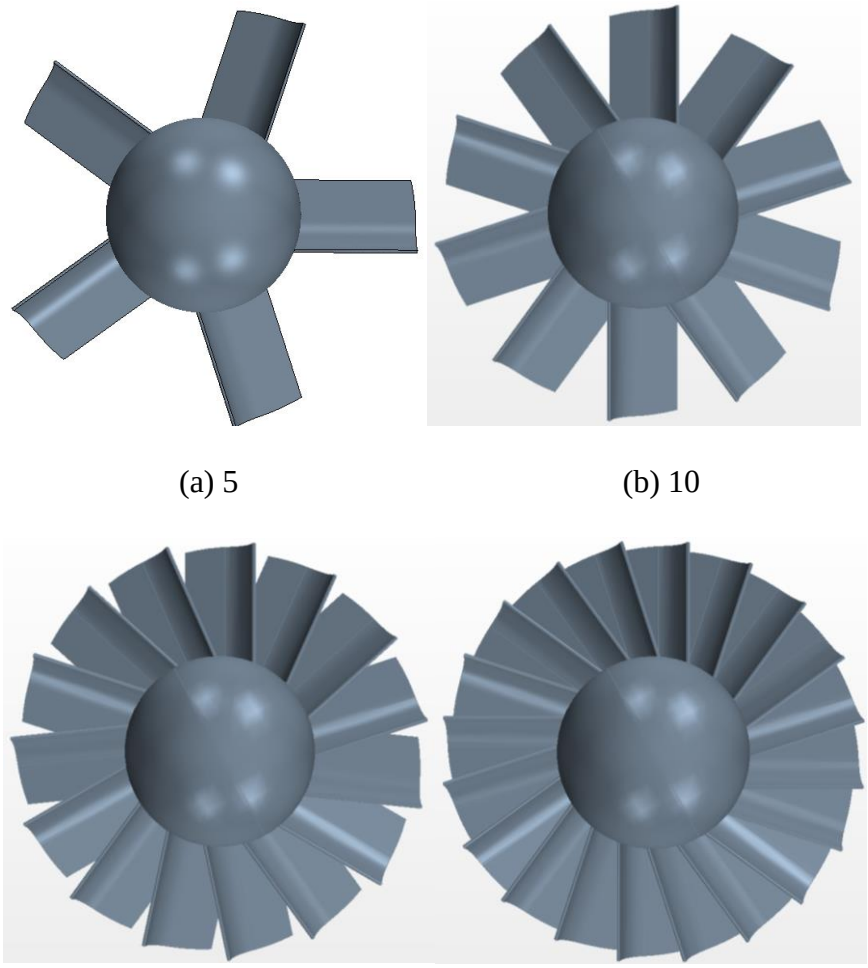

(a) 5 (b) 10

(c) 15 (d) 20

Figure 7.15: The stator model with four guide vane numbers: (a) 5; (b) 10; (c) 15; (d) 20.

As discussed in Section 5.5.1, guide vanes increase the speed of the passing flow, which can improve the aerodynamic performance of the turbine. Changing the guide vane number affects this potentially beneficial effect. Table 7.1 lists values of the maximum flow speed

against four guide vane numbers. Results show that the maximum speed increases with the number of guide vanes. It indicates that the beneficial effect of guide vanes is enhanced with the increase of the number of the guide vanes.

Table 7.1: Maximum speeds of the approaching flow with different guide vane numbers.

Number of guide vanes	5	10	15	20
Maximum flow speed (m/s)	8.24	9.56	10.08	10.45

On the other hand, changing guide vane number also affects the mass flow rate of the wind turbine. The mass flow rate represents mass of the flow per unit time passing through the wind turbine. Table 7.2 shows the mass flow rate against four guide vane numbers. It can be seen that the mass flow rate decreases with the number of guide vanes due to the restriction of the guide vane to flow moving.

Table 7.2: Mass flow rates for the wind turbine with different guide vane numbers.

Number of guide vanes	5	10	15	20
Mass flow rate (kg/s)	0.226	0.21	0.18	0.16

Tables 7.1-7.2 show that wind turbines with 10 guide vanes and 15 guide vanes can achieve moderate values in both the maximum flow speed and the mass flow rate. It means that guide vane number between 10 and 15 can achieve a balance between the flow speed and the mass flow rate.

Distributions of power coefficient with four guide vane numbers are shown in Figure 7.16. The wind turbines with 10 guide vanes and 15 guide vanes have good power coefficient performances due to the good balance between the flow speed and the mass flow rate. Figure 7.16 also shows that the wind turbine with 5 guide vanes has the lowest power coefficient,

which is caused by the smallest speed of the passing flow as listed in Table 7.1. It is suggested that the guide vane number of 5 has the weakest effect on increasing the flow speed. It can be seen that performances of power coefficient with 20 guide vanes are also poor. This is caused by the lowest mass flow rate as listed in Table 7.2. 20 guide vanes greatly restrain wind from passing through the wind turbine.

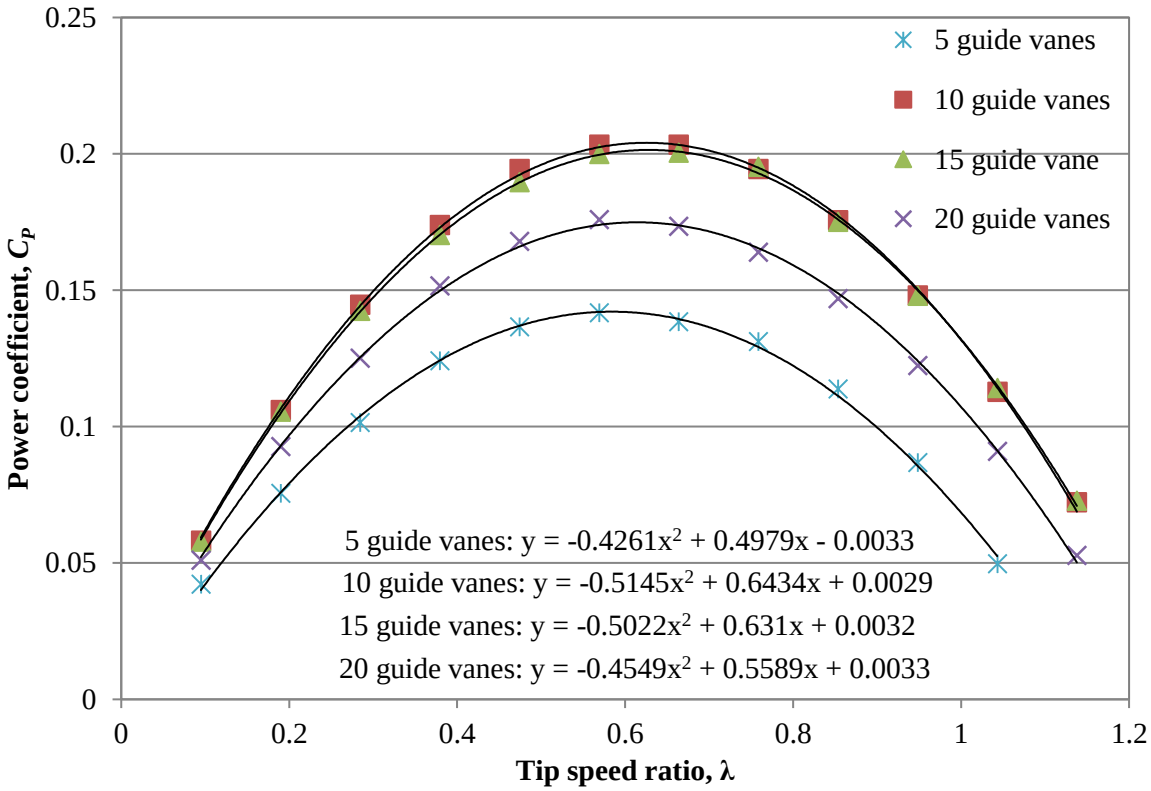

Figure 7.16: Distributions of power coefficient of the proposed wind turbine with four guide vane numbers.

Torque coefficient distributions with four guide vane numbers are shown in Figure 7.17. The values of maximum torque coefficients are in a range of 0.5 - 0.67. It is worth noting that, while the maximum torque coefficient reaches the lowest value for the turbine with 5 guide vanes due to the smallest flow speed, the minimum value of 0.5 is high compared with those

of conventional wind turbines [52], demonstrating the potential of the proposed wind turbine in terms of good starting capability.

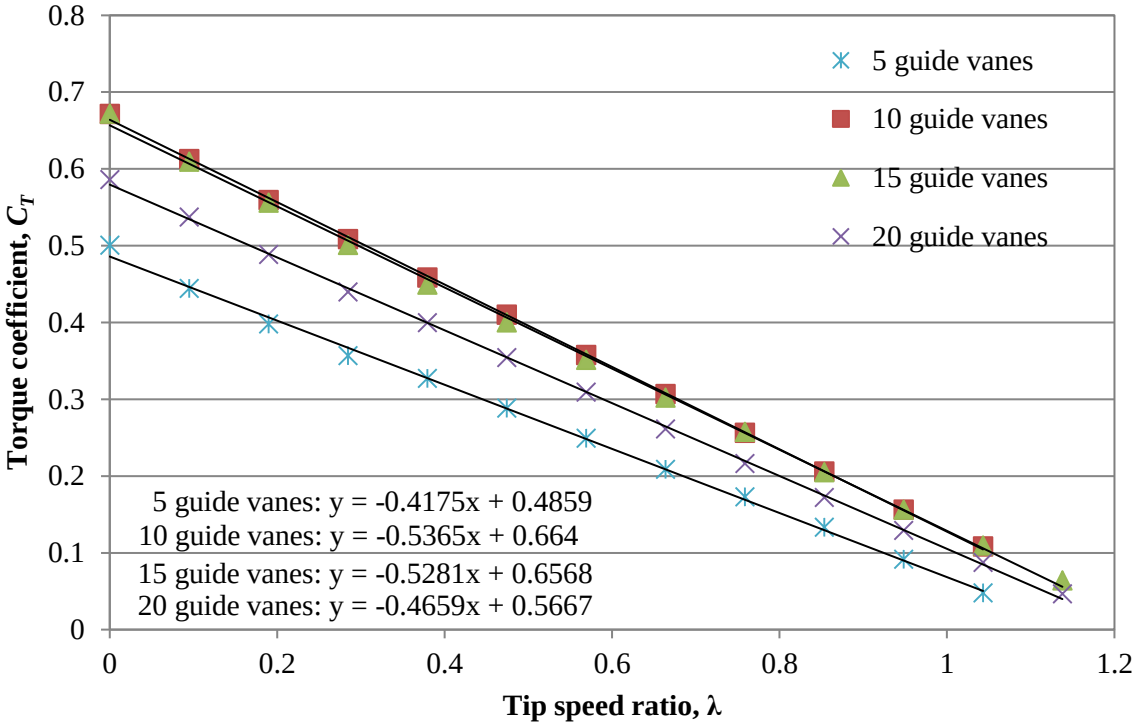

Figure 7.17: Distributions of torque coefficient of the proposed wind turbine with four guide vane numbers.

Figure 7.18 shows distributions of thrust coefficient of wind turbines with four guide vane numbers. It can be seen that thrust coefficient with 5 guide vanes is the highest. Influences of guide vanes on the properties of passing flow have been studied in Section 5.4. When the wind turbine has less guide vanes, guide vanes will have less influence on the flow direction. Therefore, the flow cannot pass blades with an optimal direction, which generates large thrust on blades. More guide vanes have stronger effects on the passing flow and result in lower thrust on blades.

The guide vane number also influences the trend of C_N-λ relationship. A regression analysis shows that the value of C_N rises slowly when the proposed wind turbine has 15 guide vanes or more. This indicates that guide vanes can restrict the increment of C_N and lead to the small C_N value.

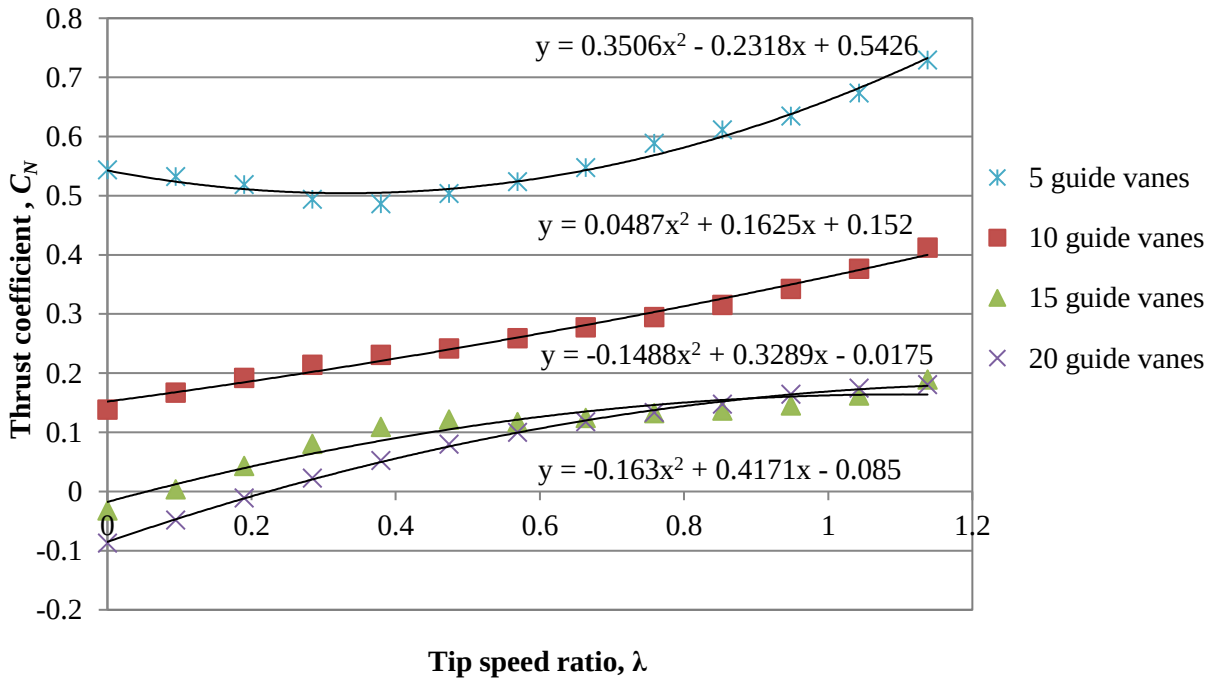

Figure 7.18: Distributions of thrust coefficient of the proposed wind turbine with four guide vane numbers.

7.6 Summary

In this chapter, influences of geometry parameters, such as hub-to-tip ratios, numbers of blades, aerofoil profiles and numbers of guide vanes, on aerodynamic performances of the wind turbine have been analysed. Results show that varying these geometrical parameters can affect the maximum power coefficient significantly. When the wind turbine has 10 guide vanes, the power coefficient can exceed 0.2 which is the highest value obtained by the wind

turbines investigated in the study. It is also found that the proposed wind turbine has higher values of the maximum torque coefficient compared with conventional wind turbines.

Chapter 8 Discussion

A novel wind turbine based on the impulse turbine technology has been proposed. The aerodynamics of the proposed wind turbine has been analysed by the wind tunnel testing and CFD simulations. Aerodynamic performances of the proposed wind turbine are discussed in this chapter.

8.1 Comparison about Aerodynamics between the Proposed Wind Turbine and Conventional Wind Turbines

Aerodynamic performances of the proposed wind turbine are compared with those of conventional wind turbines in this section. The power coefficient, torque coefficient and thrust coefficient represent power output, starting capability and axial loads on the rotor. The proposed wind turbine has a diameter of 300 mm. The diameter depends on the size of the omni-flow wind energy system [15]. Therefore, this proposed wind turbine is compared with the similar scale conventional wind turbines, along with aerodynamics under low wind speeds, due to the urban environment where it is situated.

8.1.1 Power Coefficient

The maximum power coefficient (C_P) of the proposed wind turbine is similar to that of a conventional wind turbine. In the wind speed range of 5 m/s – 6 m/s, the proposed wind turbine has the maximum C_P of approximately 0.16 as shown in Figure 5.16. From the literature review, the maximum C_P of a 391mm-diameter HAWT is 0.14 [47]. The maximum C_P of a 330mm-diameter Savonius VAWT is 0.13 [161]. In the wind speed range of 7 m/s - 8.2 m/s, the proposed wind turbine can achieve the maximum C_P of 0.2, as shown in Figure 7.16. From the literature review, a 234mm-diameter HAWT has a peak C_P of 0.18 [162]. The

maximum C_P of a 240mm-diameter VAWT is 0.14 [163]. Therefore, the proposed wind turbine has a competitive power generation capability, in the urban areas.

8.1.2 Torque Coefficient

The maximum torque coefficient (C_T) of the proposed wind turbine is approximately 0.7 as shown in Figure 5.19. From research performed, a small-scale HAWT has the maximum C_T of 0.11 and a VAWT has the maximum C_T of 0.4 [52, 163]. The proposed wind turbine has the greater value of the maximum C_T, when compared with conventional wind turbines. This indicates that the proposed wind turbine has a good starting capability. Experimental results in Figure 5.20 show that the wind turbine can start to work at wind speeds as low as 1.6 m/s. Hence, the wind turbine can capture wind energy with low velocity wind. This feature is important for an urban wind turbine because wind in an urban environment occurs at low speeds.

8.1.3 Thrust Coefficient

Results in Figure 7.5, Figure 7.9 and Figure 7.14 show that the thrust coefficient (C_N) corresponding to the maximum C_P is always less than 0.2. The C_N of a conventional wind turbine is high up to 1 [18]. The proposed wind turbine has 20 blades so thrust on one blade is much smaller than that of a conventional wind turbine. The small thrust can allow a reduction in strength and weight of the materials used in the turbine.

8.2 Comparison about Aerodynamics of the Proposed Wind Turbine under Uniform Flow and Non-uniform Flow

Recently, researchers have mainly focused on studying a wind turbine under the uniform flow condition [17]. In this project, the proposed wind turbine has been investigated under both uniform and non-uniform flow conditions. Compared with the maximum C_P under the

uniform flow condition, the maximum C_P decreases by 65% under the 20% non-uniform flow condition and by 29% under the 40% non-uniform flow condition. Hence, the power output capability of the wind turbine is weakened under the non-uniform flow conditions.

The maximum C_T decreases from 0.7 to 0.4 under the 20% non-uniform flow condition and to 0.58 under the 40% non-uniform flow condition. Therefore, the starting capability of the wind turbine is lowered under the non-uniform flow conditions, when compared to the uniform flow condition. However, values of maximum C_T under the non-uniform flow conditions are higher than those of conventional wind turbines [52, 163]. Hence, the proposed wind turbine has the potential of good starting capability even operating under the non-uniform flow conditions.

8.3 Effects of Geometrical Parameters on Aerodynamics

Influences of four geometrical parameters on aerodynamics of the proposed wind turbine have been studied under the uniform flow condition. Values of the maximum C_P, maximum C_T and maximum C_N with different geometrical parameters are listed in Tables 8.1 – 8.4. The ratio of 0.45 is the best of three ratios, due to the highest value of the maximum C_P shown in Table 8.1.

Table 8.1: Key aerodynamic features of the proposed wind turbine with three hub-to-tip ratios.

Hub-to-tip ratio	0.35	0.45	0.6
Maximum C_P	0.17	0.176	0.157
Maximum C_T	0.59	0.59	0.54
Maximum C_N	0.22	0.18	0.13

Table 8.2 shows that the wind turbine with 20 blades has a high value of the maximum C_P. When the blade number is greater than 20, there is no improvement on the maximum C_P and C_T. However, the thrust performance would be compromised. Table 8.2 indicates that the aerodynamics of the wind turbine cannot be improved significantly with more than 20 blades.

Table 8.2: Key aerodynamic features of the proposed wind turbine with five blades numbers.

Number of blades	15	17	20	25	30
Maximum C_P	0.148	0.162	0.176	0.177	0.177
Maximum C_T	0.5	0.54	0.59	0.59	0.59
Maximum C_N	0.09	0.12	0.18	0.24	0.32

When replacing Type 1 aerofoil with Type 2 or Type 3 aerofoils, there are slight improvements on the maximum C_P as shown in Table 8.3. On the other hand, Type 3 aerofoil has the highest C_P at a high tip speed ratio (λ = 0.76). Type 3 aerofoil also has a high value of maximum C_T for good startup capability. Table 8.3 also shows that Type 3 aerofoil has the good performance on thrust due to the improved leading edge. The comparison in Table 8.3 indicates that changing the leading edge of the blade aerofoil can improve the aerodynamic properties of the proposed wind turbine.

Table 8.3: Key aerodynamic features of the proposed wind turbine with three aerofoils.

Aerofoil type	Type 1	Type 2	Type 3
Maximum C_P	0.176	0.178	0.181
C_P at λ = 0.76	0.161	0.175	0.18
Maximum C_T	0.59	0.52	0.5
Maximum C_N	0.18	0.1	0.08

Table 8.4 lists key aerodynamic features of the wind turbines with four guide vane numbers (5, 10, 15 and 20) that have been studied. The wind turbines with 10 and 15 guide vanes have high values for maximum C_P and C_T. The 15 guide vane turbine is more efficient than the 10 guide vane turbine as it has a smaller C_N.

Table 8.4: Key aerodynamic features of the proposed wind turbine with four numbers of guide vanes.

Number of guide vanes	5	10	15	20
Maximum C_P	0.142	0.2	0.2	0.176
Maximum C_T	0.5	0.67	0.67	0.59
Maximum C_N	0.73	0.41	0.18	0.18

Although geometrical parameters affect values of C_T, the maximum C_T is in a high range from 0.5 to 0.67. This ensures the good starting capability of the proposed wind turbine with different geometrical parameters, when compared with conventional wind turbines.

8.4 Approaches Adopted in this Project

In this study, the CFD approach and wind tunnel testing have been utilised to investigate aerodynamics of the proposed wind turbine. The computational wind turbine model has the same dimensions to the experimental prototype, therefore, there is no scale effect when comparing numerical results with experimental data. The comparison has shown that the CFD approach can provide results with acceptable levels of accuracy, and that the realisable k-ε model is suitable to investigate the proposed wind turbine.

When compared with the wind tunnel testing, the CFD approach can save the cost of the test rig. Furthermore, through the use of CFD simulations, the cost of prototypes also can be saved, especially when studying influences of geometrical parameters. Visual indications

were found by CFD simulations and then employed in analyses such as, flow pressure distributions on the blade aerofoil, shown in Chapter 5. Because the blades were rotating in the wind tunnel testing, pressure on the blade aerofoil was very difficult to be detected.

Chapter 9 Conclusions and Recommendations for Future Work

9.1 Conclusions

A new wind turbine that employs the impulse turbine technology has been proposed. The aerodynamics of the proposed wind turbine subjected to the uniform and non-uniform flow conditions has been investigated. Influences of several key geometrical parameters on aerodynamic characteristics have also been studied. The project aim stated in Chapter 1 has been fulfilled.

Findings about aerodynamics of this wind turbine under the uniform flow condition are listed as follows:

- The wind turbine has the maximum power coefficient of 0.17, which means that the wind turbine has the potential to be used. The wind turbine has the maximum torque coefficient of 0.7 that means good self-starting capability to operate with low velocity wind in an urban environment.
- Guide vanes can increase the velocity of the passing flow. Guide vanes also can optimise directions of the passing flow inside the omni-flow wind energy system. Employment of such guide vanes can improve the potential of the wind turbine in power generation and starting capability.
- The numerical results have agreed well with experimental data. The realisable k-ε turbulence model is suitable to model the proposed wind turbine, compared with standard k-ε, standard k-ω and SST k-ω turbulence models.

The investigation under the non-uniform flow condition has revealed the following:

- Aerodynamic performances of this wind turbine under the non-uniform flow condition are poor. Due to the generation of the negative normal force on blades, the wind turbine has low values (0.06 – 0.126) of the maximum power coefficient and low values (0.4 – 0.58) of the maximum torque coefficient. It is found that the larger entrance area of the non-uniform flow, the higher the power coefficient and torque coefficient.
- The non-uniform flow leads to non-uniform thrust on the blades. It is found that thrust is subject to periodical changes of loading with the frequency of 8 Hz – 10 Hz.

Findings about investigations of geometrical parameters can be addressed as follows:

- Geometrical parameters affect the performances of power coefficient. The hub-to-tip ratio of 0.45 has the better distribution of power coefficient than the other two ratios. An increase of blade number improves the maximum power coefficient significantly, but there is only slight improvement when the blade number exceeds 20. The guide vane number of 15 can produce good performances on both power and thrust coefficients.
- A change of the leading edge of blade aerofoil helps to reduce the negative pressure difference that results in the negative normal force and lowering power output. With the improved aerofoil profile, power coefficient of the wind turbine is significantly improved at high tip speed ratios.
- The proposed wind turbine can maintain high values of the maximum torque coefficients with different geometrical parameters.

In summary, a new type of wind turbine has been presented in this thesis. On the basis of the aerodynamic analyses performed, there are indications that the wind turbine can be used in urban areas.

9.2 Recommendations for Future Work

The thesis provides aerodynamic analyses about the new wind turbine. The following recommendations are presented for future studies:

9.2.1 Study of the Whole Energy System

A study of the whole system, combining the novel wind turbine and the omni-flow system, was not carried out as part of this project. Due to the size of the omni-flow system, it is not feasible to test a prototype of the whole system in the wind tunnel. It is recommended for future researchers to implement an aerodynamic study of the whole system.

9.2.2 Optimisation of the Geometry

Because of the limited amount of time, the geometry of the proposed wind turbine has not been exhaustively investigated. From the literature review, optimisation of geometrical parameters, such as the twist angle of blades, the guide vane profile and the setting angle of guide vanes, can improve aerodynamics of a wind turbine. Therefore, it is recommended to optimise the geometry in further research.

9.2.3 Study of the Wind Turbine with a Diffuser

This project has carried out aerodynamic analyses for the proposed wind turbine working inside a cylindrical shroud that is based upon the impulse turbine technology. But the literature review shows that using a diffuser can improve aerodynamic performances of a

wind turbine. Therefore, it is suggested to study the aerodynamics when a diffuser is introduced into the proposed wind turbine.

References

[1] A. Arapogianni and J. Moccia, "Avoiding fossil fuel costs with wind energy," European Wind Energy Association, 2014.

[2] D. W. I. Association, "Denmark - Wind Energy Hub," 2014.

[3] "Wind energys cenarios for 2030," the European Wind Energy Association, 2015.

[4] "Wind Energy in the UK," RenewableUK, 2014.

[5] "Small and Medium Wind UK Market Report," RenewableUK, 2015.

[6] "Improving the energy efficiency of our homes and buildings - energy certificates and air-conditioning inspections for buildings," UK Department for Communities and Local Government, 2008.

[7] "Climate Chang Act 2008," UK Parliament, 2008.

[8] A. D. Peacock, D. Jenkins, M. Ahadzi, A. Berry, et al., "Micro wind turbines in the UK domestic sector," *Energy and Buildings*, vol. 40, pp. 1324-1333, 2008.

[9] W. T. Chong, A. Fazlizan, S. C. Poh, K. C. Pan, et al., "The design, simulation and testing of an urban vertical axis wind turbine with the omni-direction-guide-vane," *Applied Energy*, vol. 112, pp. 601-609, 2013.

[10] F. Balduzzi, A. Bianchini, E. A. Carnevale, L. Ferrari, et al., "Feasibility analysis of a Darrieus vertical-axis wind turbine installation in the rooftop of a building," *Applied Energy*, vol. 97, pp. 921-929, 2012.

[11] S. Mertens, *Wind energy in the built environment*, Brentwood, UK: Multi-Science, 2006.

[12] "Global wind report," Global Wind Energy Council, 2014.

[13] V. Sureshan, "Omni-directional wind power station," Patent no. WO2008017106A1, 2008.

[14] X. Zhang, Y. K. Chen, and R. Calay, "Modelling and analysis of a novel wind turbine structure," *International Journal of Modelling, Identification and Control*, vol. 19, pp. 142-149, 2013.

[15] X. Zhang, "Analysis and optimisation of a novel wind turbine turbine," Ph.D. thesis, University of Hertfordshire, UK, 2013.

[16] P. Ying, Y. K. Chen, and Y. G. Xu, "An aerodynamic analysis of a novel small wind turbine based on impulse turbine principles," *Renewable Energy*, vol. 75, pp. 37-43, 2015.

[17] A. Miller, B. Chang, R. Issa, and G. Chen, "Review of computer-aided numerical simulation in wind energy," *Renewable and Sustainable Energy Reviews*, vol. 25, pp. 122-134, 2013.

[18] T. Burton, D. Sharpe, N. Jenkins, and E. Bossanyi, *Wind energy handbook*, Chichester, UK: John Wiley & Sons, Ltd., 2001.

[19] J. F. Manwell, J. G. McGowan, and A. L. Rogers, *Wind Energy Explained - Theory, Design and Application*, Chichester, UK: John Wiley & Sons, Ltd., 2002.

[20] "Global Wind Report Annual Market Update 2013," Global Wind Energy Concil, 2013.

[21] P. Molly, "Zukunft der Windenergie weltweit DEWI GmbH,Erneuerbare Großprojekte Wind und Wasser," in *Stiftung Energie & Klimaschutz Baden-Württemberg*, Stuttgart, Germany 2009.

[22] Y. Kyozuka, "An experimental study on the Darrieus-Savonius turbine for the tidal current power generation," *Journal of Fluid Science and Technology*, vol. 3, pp. 439-449, 2008.

[23] M. M. Aslam Bhutta, N. Hayat, A. U. Farooq, Z. Ali, et al., "Vertical axis wind turbine – a review of various configurations and design techniques," *Renewable and Sustainable Energy Reviews*, vol. 16, pp. 1926-1939, 2012.

[24] S. Eriksson, H. Bernhoff, and M. Leijon, "Evaluation of different turbine concepts for wind power," *Renewable and Sustainable Energy Reviews*, vol. 12, pp. 1419-1434, 2008.

[25] G. J. M. Darrieus, "Turbine having its rotating shaft trans-verse to the flow of the current," US Patent no.1835018, 1931.

[26] M. R. Patel, *Wind and Solar Power Systems: design, analysis and operation*, Boca Raton, US: CRC Press, 2005.

[27] R. Howell, N. Qin, J. Edwards, and N. Durrani, "Wind tunnel and numerical study of a small vertical axis wind turbine," *Renewable Energy*, vol. 35, pp. 412-422, 2010.

[28] J. L. Tangler and D. M. Somers, "NREL Airfoil Families for HAWTs," NREL, 1995.

[29] W. A. Timmer and R. P. J. O. M. van Rooij, "Summary of the Delft University wind turbine dedicated airfoils," *Journal of Solar Energy Engineering*, vol. 125, pp. 488-496, 2003.

[30] P. Fuglsang and C. Bak, "Development of the Riso wind turbine airfoils," *Wind Energy*, vol. 7, pp. 145-162, 2004.

[31] E. L. Houghton and P. W. Carpenter, *Aerodynamics for Engineering Students*, Fourth ed, London, UK: Edward Arnold, 1993.

[32] A. Makkawi, A. Celik, and T. Muneer, "Evaluation of micro-wind turbine aerodynamics, wind speed sampling interval and its spatial variation," *Building Services Engineering Research and Technology*, vol. 30, pp. 7-14, 2009.

[33] D. R. Drew, J. F. Barlow, and T. T. Cockerill, "Estimating the potential yield of small wind turbines in urban areas: a case study for Greater London, UK," *Journal of Wind Engineering and Industrial Aerodynamics*, vol. 115, pp. 104-111, 2013.

[34] J. T. Millward-Hopkins, A. S. Tomlin, L. Ma, D. B. Ingham, et al., "Assessing the potential of urban wind energy in a major UK city using an analytical model," *Renewable Energy*, vol. 60, pp. 701-710, 2013.

[35] F. Balduzzi, A. Bianchini, and L. Ferrari, "Microeolic turbines in the built environment: Influence of the installation site on the potential energy yield," *Renewable Energy*, vol. 45, pp. 163-174, 2012.

[36] P. Blackmore, "Siting micro-wind turbines on house roofs," BRE Press, 2008.

[37] I. Abohela, N. Hamza, and S. Dudek, "Effect of roof shape, wind direction, building height and urban configuration on the energy yield and positioning of roof mounted wind turbines," *Renewable Energy*, vol. 50, pp. 1106-1118, 2013.

[38] L. Ledo, P. B. Kosasih, and P. Cooper, "Roof mounting site analysis for micro-wind turbines," *Renewable Energy*, vol. 36, pp. 1379-1391, 2011.

[39] M. A. Kotb and H. A. Soliman, "Performance analysis of a horizontal axis wind turbine under non uniform flow with swirl," *Journal of Wind Engineering and Industrial Aerodynamics*, vol. 37, pp. 103-111, 1991.

[40] S. Murakami and A. Mochida, "3-D numerical simulation of airflow around a cubic model by means of the k-ϵ model," *Journal of Wind Engineering and Industrial Aerodynamics*, vol. 31, pp. 283-303, 1988.

[41] S. Wagner, R. Bareib, and G. Guidati, *Wind Turbine Noise*, Berlin, Germany: Springer-Verlag, 1996.

[42] L. D. Knopper and C. A. Ollson, "Health effects and wind turbines: a review of the literature," *Environmental Health*, vol. 10, pp. 78, 2011.

[43] E. Pedersen and K. Persson Waye, "Perception and annoyance due to wind turbine noise—a dose–response relationship," *The Journal of the Acoustical Society of America*, vol. 116, pp. 3460, 2004.

[44] A. L. Rogers, J. F. Manwell, and S. Wright, "Wind Tubrine Acoustic Noise," Renewable Energy Research Laboratory, University of Massachusetts at Amherst, 2002.

[45] B. Vick and S. Broneske, "Effect of blade flutter and electrical loading on small wind turbine noise," *Renewable Energy*, vol. 50, pp. 1044-1052, 2013.

[46] G. J. W. Van Bussel, "Small wind turbines for the built environment," in *4th Eurpean and Asian Wind Engineering Conference*, Prague, Czech, 2005.

[47] R. A. Kishore, T. Coudron, and S. Priya, "Small-scale wind energy portable turbine (SWEPT)," *Journal of Wind Engineering and Industrial Aerodynamics*, vol. 116, pp. 21-31, 2013.

[48] R. K. Singh, M. R. Ahmed, M. A. Zullah, and Y.-H. Lee, "Design of a low Reynolds number airfoil for small horizontal axis wind turbines," *Renewable Energy*, vol. 42, pp. 66-76, 2012.

[49] R. K. Singh and M. R. Ahmed, "Blade design and performance testing of a small wind turbine rotor for low wind speed applications," *Renewable Energy*, vol. 50, pp. 812-819, 2013.

[50] O. Ozgener and L. Ozgener, "Exergy and reliability analysis of wind turbine systems: A case study," *Renewable and Sustainable Energy Reviews*, vol. 11, pp. 1811-1826, 2007.

[51] "Small Wind Systems UK Market Report," RenewableUK, 2010.

[52] R. A. Kishore and S. Priya, "Design and experimental verification of a high efficiency small wind energy portable turbine (SWEPT)," *Journal of Wind Engineering and Industrial Aerodynamics*, vol. 118, pp. 12-19, 2013.

[53] M. S. Selig and B. D. McGranahan, "Wind tunnel aerodynamic tests of six airfoils for use on small wind turbines," *Journal of Solar Energy Engineering*, vol. 126, pp. 986, 2004.

[54] P. Giguere and M. S. Selig, "Low Reynoldes number airfoils for small horizontal axis wind turbines," *Wind Engineering*, vol. 21, pp. 367-380, 1997.

[55] J. C. C. Henriques, F. Marques da Silva, A. I. Estanqueiro, and L. M. C. Gato, "Design of a new urban wind turbine airfoil using a pressure-load inverse method," *Renewable Energy*, vol. 34, pp. 2728-2734, 2009.

[56] P. R. Ebert and D. H. Wood, "Observations of the starting behavior of a small horizontal axis wind turbine," *Renewable Energy*, vol. 12, pp. 245-257, 1997.

[57] M. M. Duquette and K. D. Visser, "Numerical implications of solidity and blade number on rotor performance of horizontal-axis wind turbines," *Journal of Solar Energy Engineering*, vol. 125, pp. 425-432, 2003.

[58] E. Dayan, "Wind energy in buildings: Power generation from wind in the urban environment-where it is needed most," *Refocus*, vol. 7, pp. 33-38, 2006.

[59] G. M. Joselin Herbert, S. Iniyan, and D. Amutha, "A review of technical issues on the development of wind farms," *Renewable and Sustainable Energy Reviews*, vol. 32, pp. 619-641, 2014.

[60] K. Pope, I. Dincer, and G. F. Naterer, "Energy and exergy efficiency comparison of horizontal and vertical axis wind turbines," *Renewable Energy*, vol. 35, pp. 2102-2113, 2010.

[61] J. V. Akwa, H. A. Vielmo, and A. P. Petry, "A review on the performance of Savonius wind turbines," *Renewable and Sustainable Energy Reviews*, vol. 16, pp. 3054-3064, 2012.

[62] B. L. Gilbert, R. A. Oman, and K. M. Foreman, "Fluid dynamics of diffuser-augmented wind turbines," *Journal of Energy*, vol. 2, pp. 368-374, 1978.

[63] O. Igra, "Research and development for shrouded wind turbines," *Energy Conversion and Management*, vol. 21, pp. 13-48, 1981.

[64] B. L. Gilbert and K. Foreman, "Experiments with a diffuser-augmented model wind turbine," *Journal of Energy Resources Technology*, vol. 105, pp. 46-53, 1983.

[65] K. Abe, M. Nishida, A. Sakurai, Y. Ohya, et al., "Experimental and numerical investigations of flow fields behind a small wind turbine with a flanged diffuser," *Journal of Wind Engineering and Industrial Aerodynamics*, vol. 93, pp. 951-970, 2005.

[66] Y. Ohya, T. Karasudani, A. Sakurai, K. Abe, et al., "Development of a shrouded wind turbine with a flanged diffuser," *Journal of Wind Engineering and Industrial Aerodynamics*, vol. 96, pp. 524-539, 2008.

[67] R. K. W. Dannecker and A. D. Grant, "Investigations of a building-integrated ducted wind turbine module," *Wind Energy*, vol. 5, pp. 53-71, 2002.

[68] S. Y. Hu and J. H. Cheng, "Innovatory designs for ducted wind turbines," *Renewable Energy*, vol. 33, pp. 1491-1498, 2008.

[69] G. W. Webster, "Devices for utilizing the power of the wind," Patent No. US4154556, 1979.

[70] N. A. Ahmed, "A novel small scale efficient wind turbine for power generation," *Renewable Energy*, vol. 57, pp. 79-85, 2013.

[71] M. H. Mohamed, G. Janiga, E. Pap, and D. Thévenin, "Optimization of Savonius turbines using an obstacle shielding the returning blade," *Renewable Energy*, vol. 35, pp. 2618-2626, 2010.

[72] B. D. Altan and M. Atılgan, "The use of a curtain design to increase the performance level of a Savonius wind rotors," *Renewable Energy*, vol. 35, pp. 821-829, 2010.

[73] K. Irabu and J. N. Roy, "Characteristics of wind power on Savonius rotor using a guide-box tunnel," *Experimental Thermal and Fluid Science*, vol. 32, pp. 580-586, 2007.

[74] A. Dragomirescu, "Performance assessment of a small wind turbine with crossflow runner by numerical simulations," *Renewable Energy*, vol. 36, pp. 957-965, 2011.

[75] G. Müller, M. F. Jentsch, and E. Stoddart, "Vertical axis resistance type wind turbines for use in buildings," *Renewable Energy*, vol. 34, pp. 1407-1412, 2009.

[76] W. T. Chong, K. C. Pan, S. C. Poh, A. Fazlizan, et al., "Performance investigation of a power augmented vertical axis wind turbine for urban high-rise application," *Renewable Energy*, vol. 51, pp. 388-397, 2013.

[77] W. T. Chong, A. Fazlizan, S. C. Poh, K. C. Pan, et al., "Early development of an innovative building integrated wind, solar and rain water harvester for urban high rise application," *Energy and Buildings*, vol. 47, pp. 201-207, 2012.

[78] K. Pope, V. Rodrigues, R. Doyle, A. Tsopelas, et al., "Effects of stator vanes on power coefficients of a zephyr vertical axis wind turbine," *Renewable Energy*, vol. 35, pp. 1043-1051, 2010.

[79] T. Sharpe and G. Proven, "Crossflex: Concept and early development of a true building integrated wind turbine," *Energy and Buildings*, vol. 42, pp. 2365-2375, 2010.

[80] T. Snaker and M. Tiryakioglu, "Design and power characterisation of a novel vertical axis wind energy conversion system (VAWECS)," *Wind Engineering*, vol. 32, pp. 559-73, 2008.

[81] S. McTavish, D. Feszty, and T. Sankar, "Steady and rotating computational fluid dynamics simulations of a novel vertical axis wind turbine for small-scale power generation," *Renewable Energy*, vol. 41, pp. 171-179, 2012.

[82] D. Japikse and N. C. Baines, *Introduction to Turbomachinery*, Concepts ETI, 1997.

[83] L. M. C. Gato and A. F. O. Falcão, "Aerodynamics of the wells turbine," *International Journal of Mechanical Sciences*, vol. 30, pp. 383-395, 1988.

[84] T. Setoguchi, S. Santhakumar, H. Maeda, M. Takao, et al., "A review of impulse turbines for wave energy conversion," *Renewable Energy*, vol. 23, pp. 261-292, 2001.

[85] T. Setoguchi and M. Takao, "Current status of self rectifying air turbines for wave energy conversion," *Energy Conversion and Management*, vol. 47, pp. 2382-2396, 2006.

[86] D. L. O'Sullivan and A. W. Lewis, "Generator selection and comparative performance in offshore oscillating water column ocean wave energy converters," *IEEE Transactions on Energy Convertion*, vol. 26, pp. 603-613, 2011.

[87] A. F. O. Falcão, "Wave energy utilization: A review of the technologies," *Renewable and Sustainable Energy Reviews*, vol. 14, pp. 899-918, 2010.

[88] A. Thakker and T. S. Dhanasekaran, "Computed effects of tip clearance on performance of impulse turbine for wave energy conversion," *Renewable Energy*, vol. 29, pp. 529-547, 2003.

[89] A. Thakker, J. Jarvis, and A. Sahed, "Design charts for impulse turbine wave energy extraction using experimental data," *Renewable Energy*, vol. 34, pp. 2264-2270, 2009.

[90] I. López, J. Andreu, S. Ceballos, I. Martínez de Alegría, et al., "Review of wave energy technologies and the necessary power-equipment," *Renewable and Sustainable Energy Reviews*, vol. 27, pp. 413-434, 2013.

[91] H. Maeda, S. Santhakumar, T. Setoguchi, M. Takao, et al., "Performance of impulse turbine with fixed guide vanes for wave power conversion," *Renewable Energy*, vol. 17, pp. 533-547, 1999.

[92] A. Thakker and F. Hourigan, "Modeling and scaling of the impulse turbine for wave power applications," *Renewable Energy*, vol. 29, pp. 305-317, 2004.

[93] H. Maeda, M. Takao, T. Setoguchi, K. Kaneko, et al., "Impulse turbine for wave power conversion with air flow rectification system," *Proc. of the Eleventh International Offshore and Polar Engineering Conference*, Stavanger (Norway), 2001.

[94] V. Jayashankar, S. Anand, T. Geetha, S. Santhakumar, et al., "A twin unidirectional impulse turbine topology for OWC based wave energy plants," *Renewable Energy*, vol. 34, pp. 692-698, 2009.

[95] K. Mala, J. Jayaraj, V. Jayashankar, T. M. Muruganandam, et al., "A twin unidirectional impulse turbine topology for OWC based wave energy plants – Experimental validation and scaling," *Renewable Energy*, vol. 36, pp. 307-314, 2011.

[96] H. K. Versteeg and W. Malalasekera, *An introduction to computational fluid dynamics - the finite volume method*, Second ed, Harlow, UK: Pearson Education Ltd., 2007.

[97] J. H. Ferziger and M. Peric, *Computational Methods for Fluid Dynamics*, Third ed, Springer, 2001.

[98] T. J. Chung, *Computational Fluid Dynamics*, Second ed, Cambridge University Press, 2002.

[99] R. Lanzafame, S. Mauro, and M. Messina, "Wind turbine CFD modeling using a correlation-based transitional model," *Renewable Energy*, vol. 52, pp. 31-39, 2013.

[100] C. Thumthae and T. Chitsomboon, "Optimal angle of attack for untwisted blade wind turbine," *Renewable Energy*, vol. 34, pp. 1279-1284, 2009.

[101] L. A. Danao, J. Edwards, O. Eboibi, and R. Howell, "A numerical investigation into the influence of unsteady wind on the performance and aerodynamics of a vertical axis wind turbine," *Applied Energy*, vol. 116, pp. 111-124, 2014.

[102] K. M. Almohammadi, D. B. Ingham, L. Ma, and M. Pourkashan, "Computational fluid dynamics (CFD) mesh independency techniques for a straight blade vertical axis wind turbine," *Energy*, vol. 58, pp. 483-493, 2013.

[103] A. Thakker and F. Hourigan, "A comparison of two meshing schemes for CFD analysis of the impulse turbine for wave energy applications," *Renewable Energy*, vol. 30, pp. 1401-1410, 2005.

[104] B. Geurts, *Elements of Direct and Large-eddy Simulation*, R.T.Ewards, 2004.

[105] W. Rodi, "Comparison of LES and RANS calculations of the flow around bluff bodies," *Journal of Wind Engineering and Industrial Aerodynamics*, vol. 69, pp. 55-75, 1997.

[106] C. J. Simão Ferreira, A. van Zuijlen, H. Bijl, G. van Bussel, et al., "Simulating dynamic stall in a two-dimensional vertical-axis wind turbine: verification and validation with particle image velocimetry data," *Wind Energy*, vol. 13, pp. 1-17, 2010.

[107] M. Lesieur, O. Métais, and P. Comte, *Large-Eddy Simulations of Turbulence*, Cambridge University Press, 2005.

[108] S. Benjanirat, L. N. Sankar, and G. Xu, "Evaluation of turbulence models for the prediction of wind turbine aerodynamics," *Proc. of ASME 2003 Wind Energy Symposium*, Reno, Nevada, USA, 2003.

[109] A. Makridis and J. Chick, "Validation of a CFD model of wind turbine wakes with terrain effects," *Journal of Wind Engineering and Industrial Aerodynamics*, vol. 123, pp. 12-29, 2013.

[110] F. Balduzzi, A. Bianchini, R. Maleci, G. Ferrara, et al., "Critical issues in the CFD simulation of Darrieus wind turbines," *Renewable Energy*, vol. 85, pp. 419-435, 2016.

[111] B. E. Launder and D. B. Spalding, "The numerical compution of turbulent flows," *Computer Methods in Applied Mechanics and Engineering*, vol. 3, pp. 269-289, 1974.

[112] D. C. Wilcox, "Comparison of two-equation turbulence models for boundary layers with pressure gradients," *AIAA Journal*, vol. 31, pp. 1414-1421, 1993.

[113] W. Wolfe and S. S. Ochs, "CFD calculations of S809 aerodynamic characteristics," in *35th AIAA Aerospace Sciences Meeting and Exhibit*, Reno, Nevada, USA, 1997.

[114] L. Aresti, M. Tutar, Y. Chen, and R. K. Calay, "Computational study of a small scale vertical axis wind turbine (VAWT): comparative performance of various turbulence models," *Wind and Structures*, vol. 17, pp. 647-670, 2013.

[115] A. Thakker and T. S. Dhanasekaran, "Experimental and computational analysis on guide vane losses of impulse turbine for wave energy conversion," *Renewable Energy*, vol. 30, pp. 1359-1372, 2005.

[116] A. Thakker, T. S. Dhanasekaran, and J. Ryan, "Experimental studies on effect of guide vane shape on performance of impulse turbine for wave energy conversion," *Renewable Energy*, vol. 30, pp. 2203-2219, 2005.

[117] T. Shih, W. W. Liou, A. Shabbir, Z. Yang, et al., "A new k- eddy viscosity model for high reynolds number turbulent flows," *Computers & Fluids*, vol. 24, pp. 227-238, 1995.

[118] T. Shih, "Some developments in computational modeling of turbulent flows," *Fluid Dynamics Research*, vol. 20, pp. 67-96, 1997.

[119] M. Raciti Castelli, A. Englaro, and E. Benini, "The Darrieus wind turbine: Proposal for a new performance prediction model based on CFD," *Energy*, vol. 36, pp. 4919-4934, 2011.

[120] M. Raciti Castelli, G. Pavesi, L. Battisti, E. Benini, et al., "Modeling strategy and numerical validation for a Darrieus vertical axis micro-wind turbine," *Proc. of ASME ASME 2010 International Mechanical Engineering Congress & Exposition*, Vancouver, British Columbia, Canada, 2010.

[121] M. H. Mohamed, "Impacts of solidity and hybrid system in small wind turbines performance," *Energy*, vol. 57, pp. 495-504, 2013.

[122] D. C. Wilcox, "Reassessment of the scale-determining equation for advanmced turbulence models," *AIAA Journal*, vol. 26, pp. 1299-1310, 1988.

[123] F. R. Menter, "Zonal two-equation k-w turbulence models for aerodynamic flows," *AIAA Paper 2906*, vol., 1993.

[124] S. L. Yang, Y. L. Chang, and O. Arici, "Navier-Stokes computations of the NREL airfoil ssing a κ — ω turbulent model at high angles of attack," *Journal of Solar Energy Engineering*, vol. 117, pp. 304-310, 1995.

[125] B. Yang and C. Lawn, "Fluid dynamic performance of a vertical axis turbine for tidal currents," *Renewable Energy*, vol. 36, pp. 3355-3366, 2011.

[126] F. Menter, "Two-equation eddy-viscosity turbulence model for engineering applications," *AIAA Journal*, vol. 32, pp. 1598-1605, 1994.

[127] A. L. Pape and J. Lecanu, "3D Navier-Stokes computations of a stall-regulated wind turbine," *Wind Energy*, vol. 7, pp. 309-324, 2004.

[128] S. Yang, Y. Chang, and O. Arici, "Navier-Stokes computations of the NREL airfoil using a k-w turbulent model at high ang;es of attack," *Journal of Solar Energy Engineering*, vol. 117, pp. 304-310, 1995.

[129] W. Wolfe and S. Ochs, "Predicting aerodynamic characteristics of typical wind turbine airfoils using CFD," Sandia National Laboratories, 1997.

[130] P. Fuglsang, C. Bak, M. Gaunaa, and I. Antoniu, "Designa nd verification of the Riso-B1 airfoil family for wind turbines," *Journal of Solar Energy Engineering*, vol. 126, pp. 1002-1010, 2006.

[131] F. Bertagnolio, N. Sorensen, and J. Johansen, "Profile catalogue for airfoil sections based on 3D computations," Riso, 2006.

[132] E. Duque, W. Johnson, C. van Dam, R. Cortes, et al., "Numerical predictions of wind turbine power and aerodynamic loads for the NREL phase II combined experiment rotor," in *ASME Wind Energy Symposium*, Reno, Nevada, US, 2000.

[133] N. Sorensen and M. O. L. Hansen, "Rotor performance predictions using a Navier-Stokes method," in *ASME Wind Energy Symposium*, Reno, Nevada, US, 1998.

[134] Y. Li, K. J. Paik, T. Xing, and P. M. Carrica, "Dynamic overset CFD simulations of wind turbine aerodynamics," *Renewable Energy*, vol. 37, pp. 285-298, 2012.

[135] S. Lin and T. Shieh, "Study of aerodynamical interference for a wind turbine," *International Communications in Heat and Mass Transfer*, vol. 37, pp. 1044-1047, 2010.

[136] Y. Bazilevs, M. C. Hsu, I. Akkerman, S. Wright, et al., "3D simulation of wind turbine rotors at full scale. Part I: Geometry modeling and aerodynamics," *International Journal for Numerical Methods in Fluids*, vol. 65, pp. 207-235, 2011.

[137] Y. Bazilevs, M. C. Hsu, J. Kiendl, R. Wüchner, et al., "3D simulation of wind turbine rotors at full scale. Part II: Fluid-structure interaction modeling with composite blades," *International Journal for Numerical Methods in Fluids*, vol. 65, pp. 236-253, 2011.

[138] C. A. Baxevanou, P. K. Chaviaropoulos, S. G. Voutsinas, and N. S. Vlachos, "Evaluation study of a Navier–Stokes CFD aeroelastic model of wind turbine airfoils

in classical flutter," *Journal of Wind Engineering and Industrial Aerodynamics*, vol. 96, pp. 1425-1443, 2008.

[139] N. Tachos, C. Zioutis, A. Filios, and D. Margaris, "Aerodynamic computational analysis for a HAWT rotor," in *European Wind Energy Conference*, Athens, Greece, 2006.

[140] N. Mandas, F. Cambuli, and C. Carcangiu, "Numerical prediction of horizontal axis wind turbine flow," in *European Wind Energy Conference*, Athens, Greece, 2006.

[141] D. Hartwanger and A. Horvat, "3D modelling of a wind turbine using CFD," in *NAFEMS Conference*, Cheltenham, UK, 2008.

[142] F. Bet and H. Grassmann, "Upgrading conventional wind turbines," *Renewable Energy*, vol. 28, pp. 71-78, 2003.

[143] T. Y. Chen, Y. T. Liao, and C. C. Cheng, "Development of small wind turbines for moving vehicles: Effects of flanged diffusers on rotor performance," *Experimental Thermal and Fluid Science*, vol. 42, pp. 136-142, 2012.

[144] L. A. Danao, O. Eboibi, and R. Howell, "An experimental investigation into the influence of unsteady wind on the performance of a vertical axis wind turbine," *Applied Energy*, vol. 107, pp. 403-411, 2013.

[145] M. Burlando, A. Ricci, A. Freda, and M. P. Repetto, "Numerical and experimental methods to investigate the behaviour of vertical-axis wind turbines with stators," *Journal of Wind Engineering and Industrial Aerodynamics*, vol. 144, pp. 125-133, 2015.

[146] S. Rolland, W. Newton, A. J. Williams, T. N. Croft, et al., "Simulations technique for the design of a vertical axis wind turbine device with experimental validation," *Applied Energy*, vol. 111, pp. 1195-1203, 2013.

[147] R. Bravo, S. Tullis, and S. Ziada, "Performance testing of a small vertical-axis wind turbine," in *21st Canadian Congress of Applied Mechanics*, Toronto, Canada, 2007.

[148] J. B. Barlow, W. H. Jr. Rae, and A. Pope, *Low-speed Wind Tunnel Testing*, Third ed, New York, US: John Wiley & Sons Ltd., 1999.

[149] W. H. Rae and A. Pope, *Low-speed Wind Tunnel Testing*, Second ed, John Wiley & Sons Ltd., 1984.

[150] L. A. M. Danao, "The influence of unsteadywind on the performance and aerodynamics of veritical axis wind turbines," Ph.D. thesis, University of Sheffield, 2012.

[151] CD-adapco, *Star-CCM+ User Guide 6.04*, 2011.

[152] P. S. Bernard, *Fluid Dynamics*, Cambridge Unversity Press, 2015.

[153] V. L. Streeter, E. B. Wylie, and K. B. Bedford, *Fluid Mechanics*, Ninth ed, McGrew Hill, 1998.

[154] J. Chen, H. Yang, M. Yang, and H. Xu, "The effect of the opening ratio and location on the performance of a novel vertical axis Darrieus turbine," *Energy*, vol. 89, pp. 819-834, 2015.

[155] Y. Peet and P. Sagaut, "Theoretical prediction of turbulent skin friction on geometrically complex surfaces," *Physics of Fluids*, vol. 21, pp. 105105, 2009.

[156] I. H. Abbott and A. E. Von Doenhoff, *Theory of Wind Sections, Including a Summary of Airfoil Data*, Dover, 1959.

[157] CD-adapco, *Star-CCM+ Training*, US, 2011.

[158] A. Thakker and F. Hourigan, "Computational fluid dynamics analysis of a 0.6m, 0.6 hub-to-tip ratio impulse turbine with fixed guide vanes," *Renewable Energy*, vol. 30, pp. 1387-1399, 2005.

[159] T. Shih, J. Zhu, and J. L. Lumley, "A realizable Reynolds stress algebraic equation model," National Aeronaustic and Space Administration, 1993.

[160] P. E. Smirnov and F. R. Menter, "Sensitization of the SST turbulence model to rotation and curvature by applying the Spalart-Shur correction term," *Journal of Turbomachinery*, vol. 131, pp. 041010-1-7, 2009.

[161] T. Hayashi, Y. Li, and Y. Hara, "Wind tunnel tests on a different phase three-stage Savonius rotor," *JSME International Journal Series B: Fluids and Thermal Engineering*, vol. 48, pp. 9-16, 2005.

[162] D. Y. C. Leung, Y. Deng, and M. K. H. Leung, "Design optimization of a cost-effective micro wind turbine," *Proc. of the World Congress on Engineering*, London, UK, 2010.

[163] U. K. Saha and M. J. Rajkumar, "On the performance analysis of Savonius rotor with twisted blades," *Renewable Energy*, vol. 31, pp. 1776-1788, 2006.

Appendix A – Drawing of Guide Vane

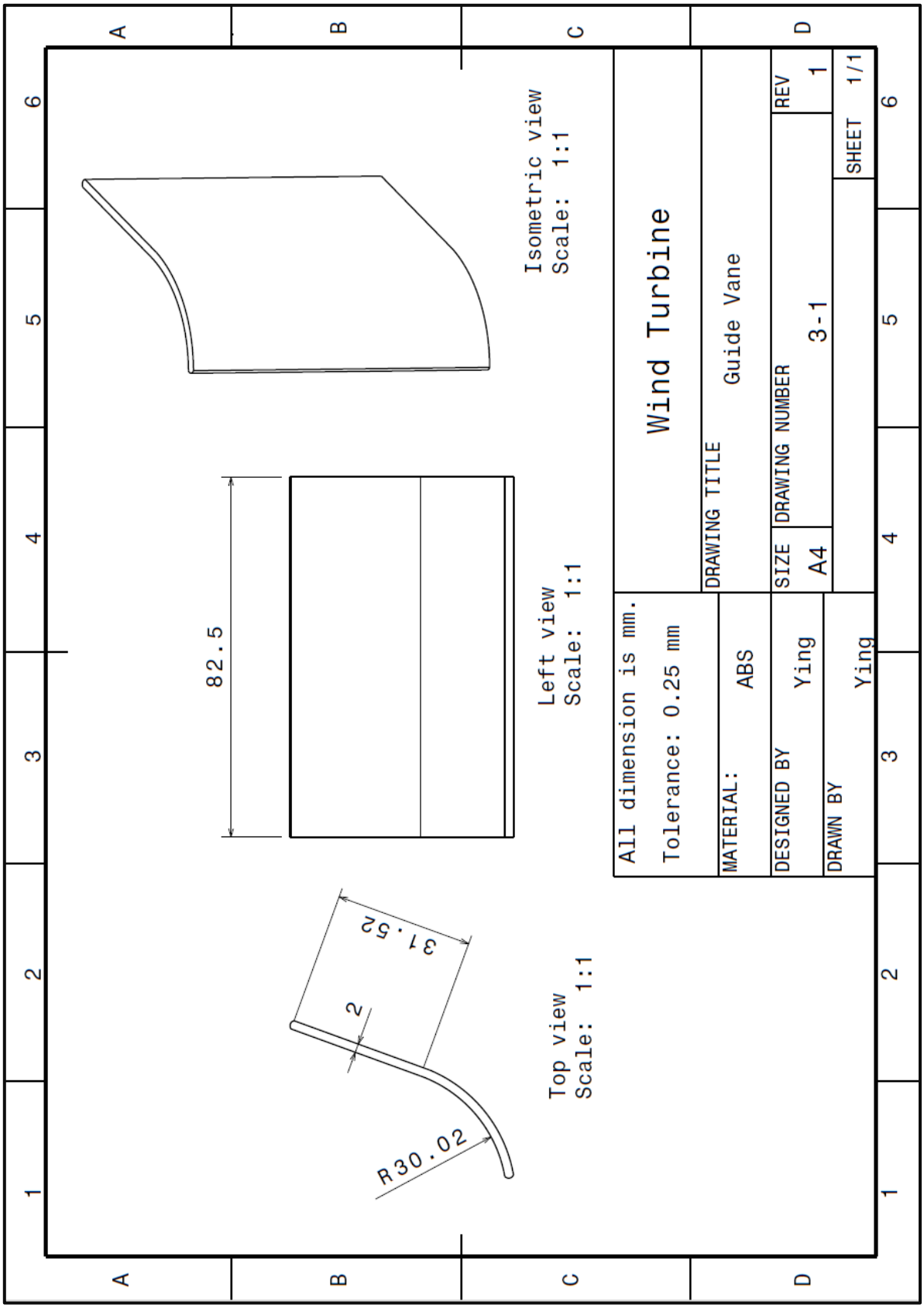

Appendix B – Drawing of Stator Hub

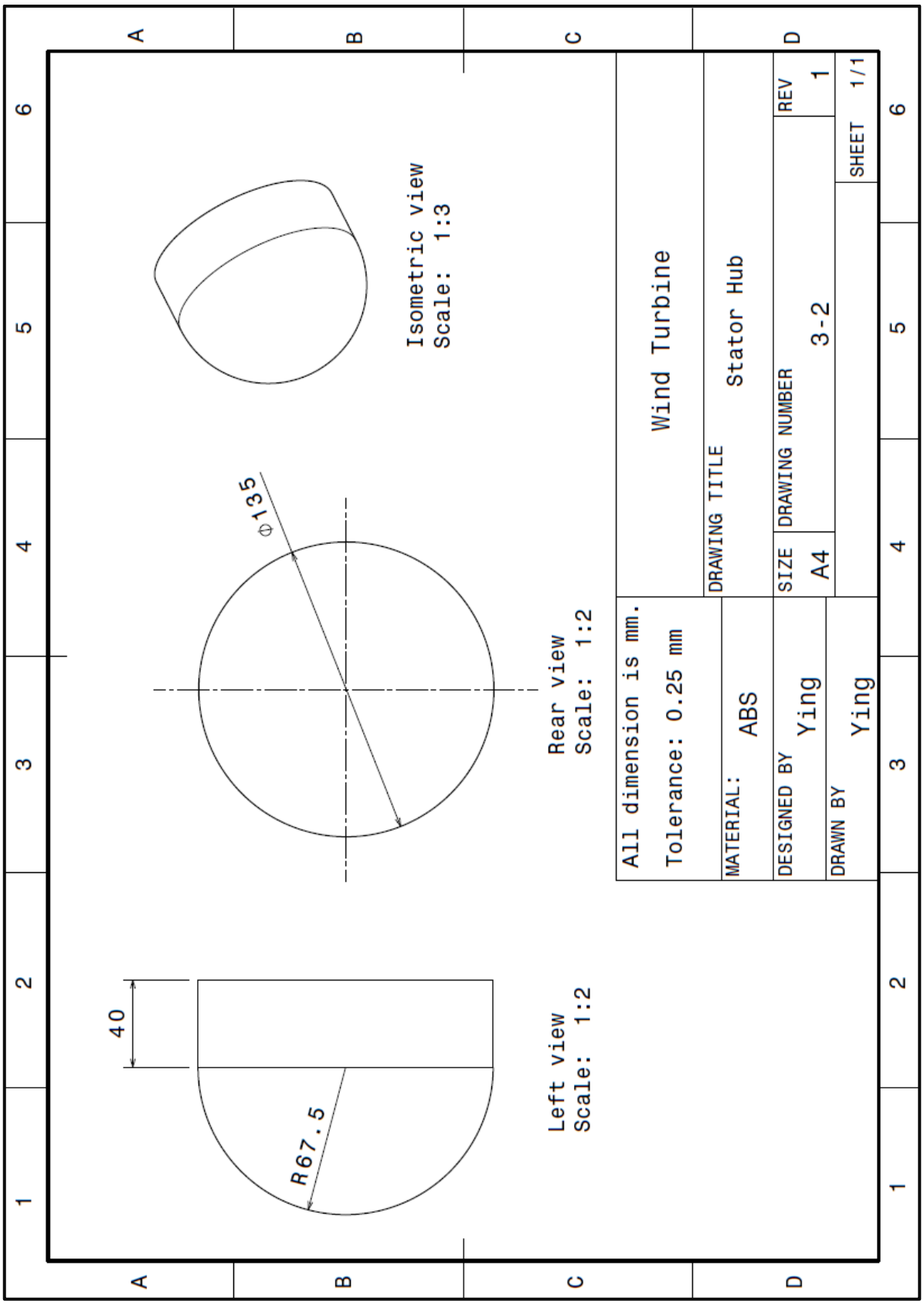

Appendix C – Drawing of Rotor Hub

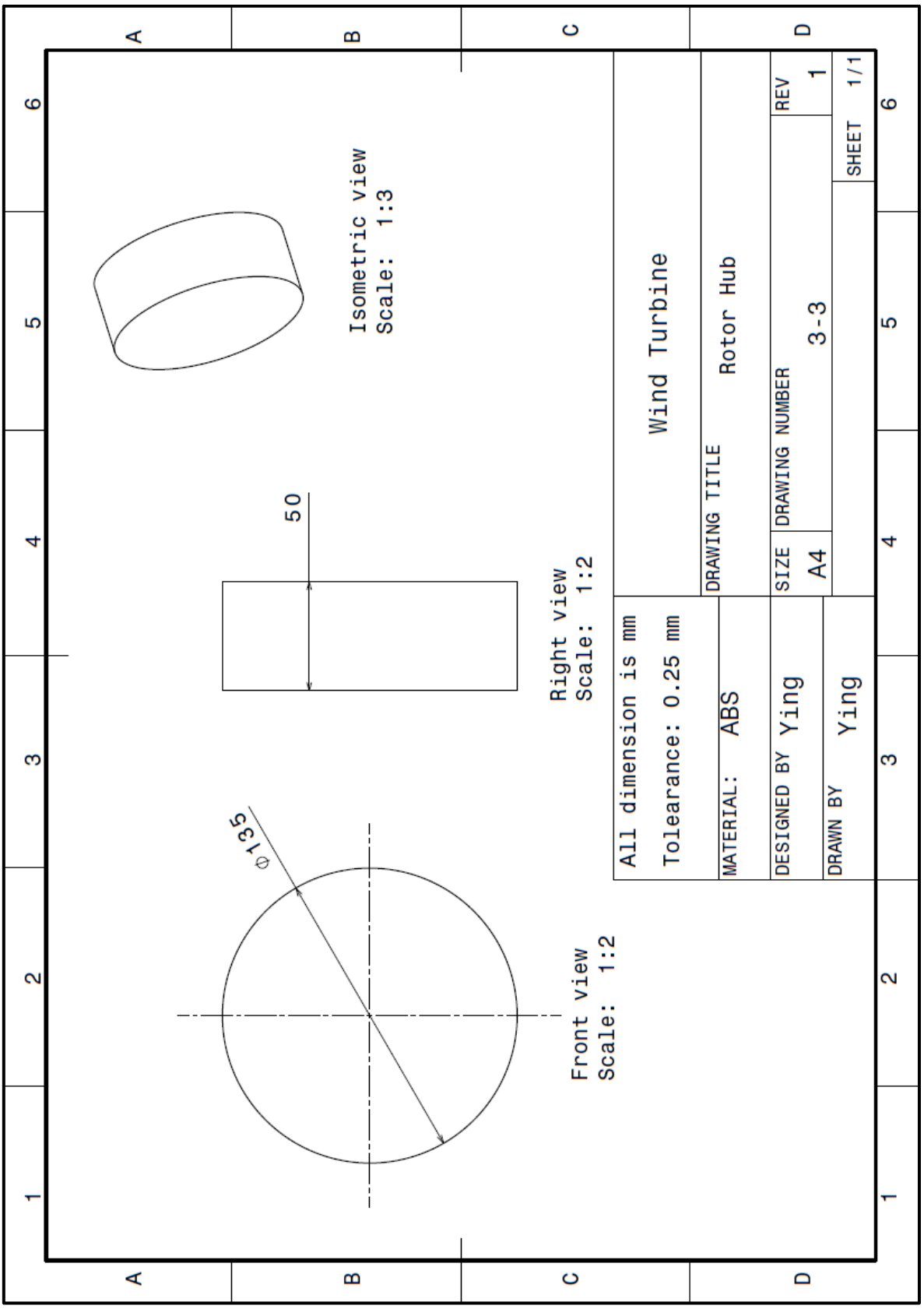

Appendix D – Coordinates of Three Aerofoils

Type 1

x (mm)	y (mm)	x (mm)	y (mm)	x (mm)	y (mm)	x (mm)	y (mm)
0	0.77	25	21.306	50.476	0.056	22	13.777
0.04	1.343	26	21.05	50.24	0	21	13.777
0.06	1.605	27	20.788	50.124	0.016	20	13.441
0.08	1.843	28	20.429	50	0.056	19	13.217
0.1	2.064	29	20.062	49.875	0.133	18	12.956
0.2	2.992	30	19.655	49.79	0.22	17	12.655
0.3	3.745	31	19.207	49.5	0.626	16	12.31
0.4	4.395	32	18.715	49	1.332	15	11.929
0.6	5.502	33	187.178	48	2.734	14	11.502
1	7.276	345	17.591	47	4.01	13	11.028
1.5	9.047	35	16.953	46	5.147	12	10.505
2	10.531	36	16.258	45	6.169	11	9.931
3	12.988	37	15.507	44	7.093	10	9.3
4	14.833	38	14.727	43	7.933	9	8.61
5	16.133	39	13.926	42	8.696	8	7.853
6	17.213	40	13.299	41	9.391	7	7.024
7	18.158	41	12.251	40	10.024	6	6.113
8	18.96	42	11.349	39	10.599	5	5.11
9	19.645	43	10.389	38	11.121	4	3.998
10	20.229	44	9.368	37	11.593	3	2.758
11	20.723	45	8.279	36	12.017	2	1.359
12	21.138	46	7.115	35	12.397	1.5	0.586
13	21.478	47	5.864	34	12.733	1.2	0.171
14	21.748	48	4.538	33	13.027	1	0.051
15	21.953	49	3.204	32	13.282	0.9	0.02
16	22.094	49.5	2.537	31	13.497	0.7	0
17	22.144	50	1.87	30	13.675	0.5	0.051
18	22.153	50.4	1.337	29	13.815	0.4	0.079
19	22.129	50.7	0.936	28	13.918	0.3	0.141
20	22.279	50.77	0.819	27	13.985	0.2	0.229
21	21.986	50.818	0.609	26	14.18	0.1	0.364
22	21.866	50.8	0.438	25	14.01	0.06	0.444
23	21.713	50.732	0.281	24	13.973	0.04	0.497
24	21.526	50.611	0.141	23	13.891	0	0.77

Type 2

x (mm)	y (mm)	x (mm)	y (mm)	x (mm)	y (mm)	x (mm)	y (mm)
0	0.786	28.5	17.914	52.15	0.185	23	10.762
0.069	1.108	29.5	17.654	52.073	0.231	22	10.522
0.25	1.507	30.5	17.359	51.95	0.35	20	9.981
0.5	2.048	31.5	17.026	51.5	0.854	18	9.355
1	3.092	32.5	16.655	51	1.418	17	9.009
1.5	4.091	33.5	16.244	50	2.539	16	8.641
2.5	5.971	34.5	15.791	49	3.574	15	8.25
3.5	7.733	35.5	15.294	48	4.509	14	7.836
5	10.122	36.5	14.752	47	5.358	13	7.398
5.5	10.875	37.5	14.15	46	6.13	11	6.447
6	11.607	38.5	13.547	45	6.832	9	5.39
7.5	13.475	39.5	12.916	44	7.472	7	4.222
8.5	14.462	40.5	12.268	43	8.054	6	3.594
9.5	15.3	41.5	11.601	42	8.582	5	2.933
10.5	16.013	42.5	10.9	41	9.059	4	2.24
11.5	16.621	43.5	10.158	40	9.489	3	1.513
12.5	17.139	44.5	9.371	39	9.874	2	0.749
13.5	17.573	45.5	8.537	38	10.215	1.5	0.353
14.5	17.932	46.5	7.653	37	10.514	1.25	0.152
15.5	18.221	47.5	6.713	36	10.774	0.9	0.009
16.5	18.429	48.5	5.713	35	10.994	0.8	0
17.5	18.565	49.5	4.656	34	11.175	0.7	0.005
18.5	18.668	50.5	3.588	33	11.32	0.6	0.022
19.5	18.738	51.5	2.521	32	11.427	0.5	0.054
20.5	18.776	52.5	1.454	31	11.498	0.4	0.101
21.5	18.782	52.83	1.103	30	11.533	0.3	0.168
22.5	18.756	52.97	0.856	29	11.532	0.2	0.262
23.5	18.698	52.97	0.557	28	11.495	0.15	0.324
24.5	18.608	52.83	0.31	27	11.421	0.1	0.402
25.5	18.485	52.63	0.173	26	11.311	0.1	0.03
26.5	18.328	52.41	0	25	11.165	0.05	0.51
27.5	18.138	52.25	0.147	24	10.98	0	0.786

Type 3

x (mm)	y (mm)	x (mm)	y (mm)	x (mm)	y (mm)	x (mm)	y (mm)
0	0.723	29	15.83	54.21	0	24	8.341
0.02	0.875	30	15.655	54.09	0.04	23	8.17
0.05	0.978	31	15.446	53.97	0.077	22	7.984
0.08	1.047	32	15.203	53.84	0.161	21	7.781
0.15	1.171	33	14.924	53.79	0.213	20	7.563
0.3	1.428	34	14.608	53.5	0.487	19	7.328
0.4	1.596	35	14.254	53	0.967	18	7.077
0.6	1.925	36	13.861	52.5	1.446	17	6.809
0.8	2.246	37	13.427	52	1.922	16	6.525
2	4.015	38	12.951	51	2.838	15	6.223
3	5.32	39	12.45	50	3.667	14	5.904
4	6.502	40	11.929	49	4.418	13	5.568
5	7.578	41	11.395	48	5.098	12.29	5.32
6	8.564	42	10.847	47	5.712	11	4.842
7	9.47	43	10.277	46	6.265	10	4.451
8	10.305	44	9.672	45	6.762	9	4.042
9	11.076	45	9.032	44	7.206	8	3.614
10	11.788	46	8.353	43	7.601	7	3.165
11	12.444	47	7.634	42	7.95	6	2.697
12	13.038	48	9.872	41	8.251	5	2.209
13	13.57	49	6.064	40	8.509	4	1.7
14	14.046	50	5.208	39	8.725	3	1.168
15	14.468	51	4.307	38	8.9	2	0.615
16	14.84	52	3.399	37	9.035	1	0.048
17	15.164	53	2.491	36	9.13	0.9	0.016
18	15.441	54	1.583	35	9.185	0.8	0
19	15.675	54.5	1.129	34	9.205	0.5	0.034
20	15.865	54.6	1.0335	33	9.2	0.4	0.076
22	16.119	54.687	0.941	32	9.2	0.25	0.178
23	16.184	54.765	0.784	31	9.104	0.15	0.286
24	16.209	54.793	0.57	30	9.04	0.1	0.361
25	16.198	54.748	0.379	29	8.96	0.08	0.4
26	16.155	54.67	0.243	28	8.869	0.05	0.469
27	16.079	54.56	0.141	27	8.76	0.02	0.571
28	15.971	54.42	0.063	26	8.636	0	0.723

Appendix E – Flow Velocity and Pressure Change When Passing Guide Vanes

r = 70mm

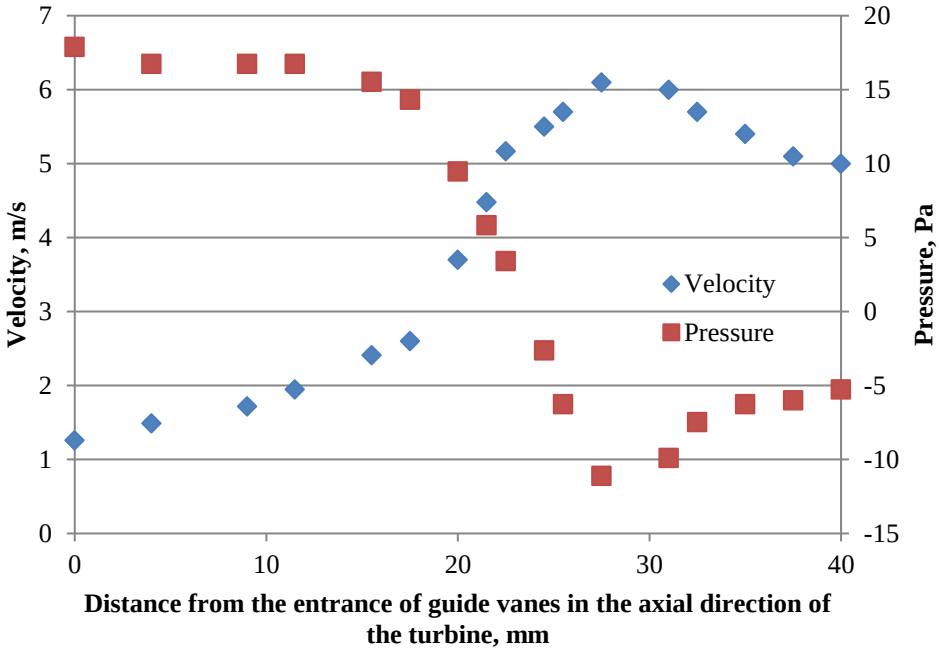

r = 147mm

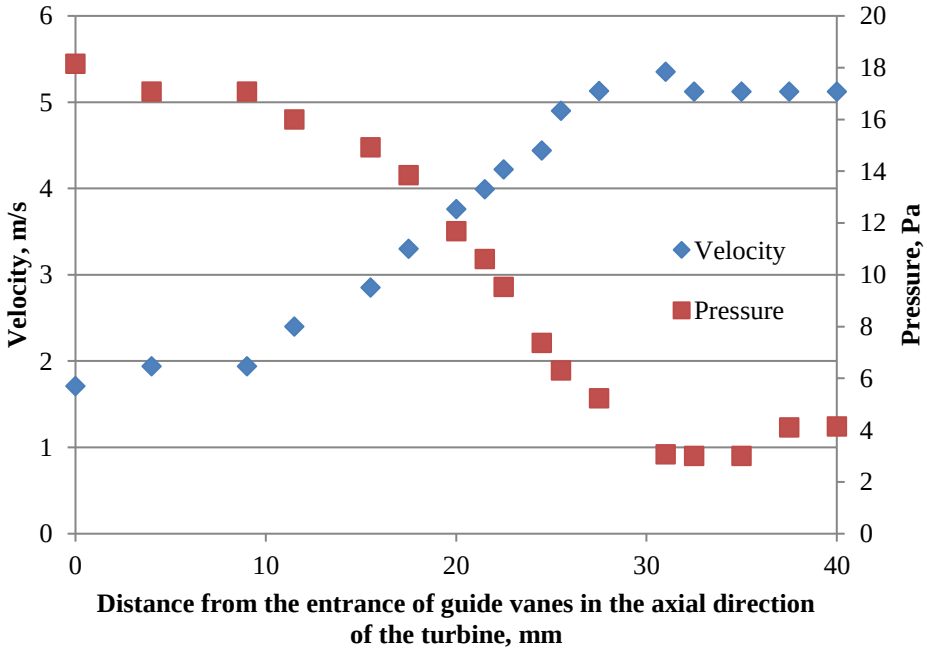

Appendix F – Flow Directions inside the Omni-flow System with and without a Stator

(a) When free stream wind is at 12^o to the omni-flow system without the stator

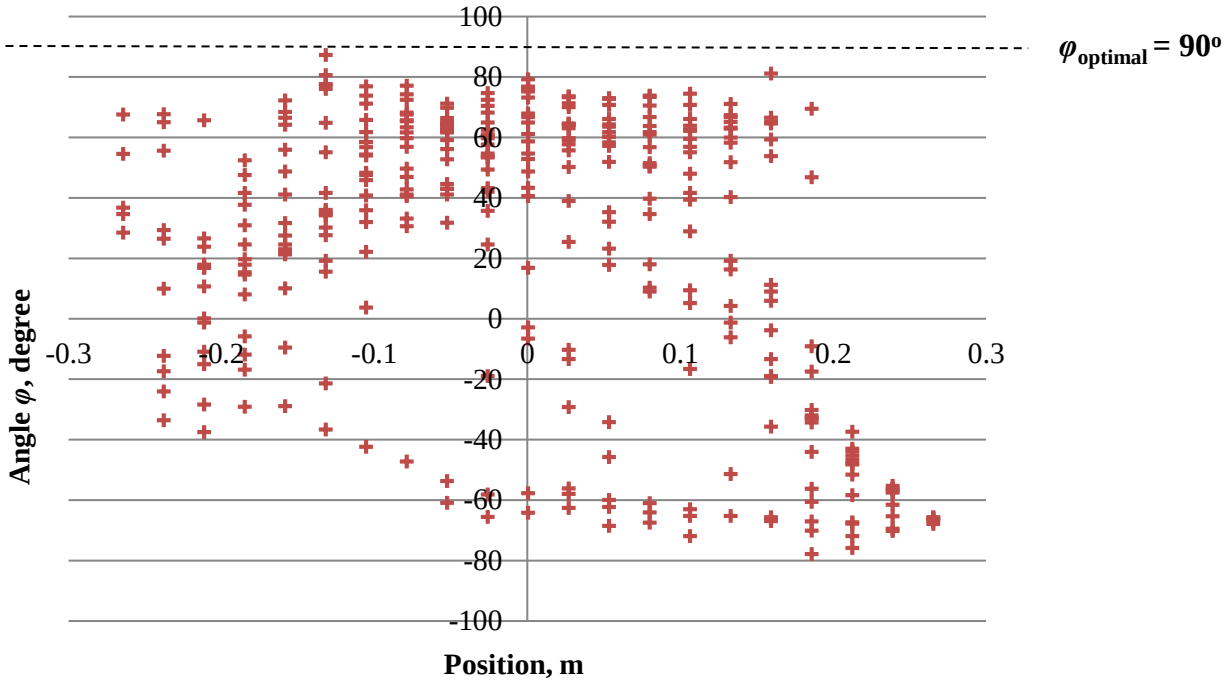

(b) When free stream wind is at 12^o to the omni-flow system with the stator

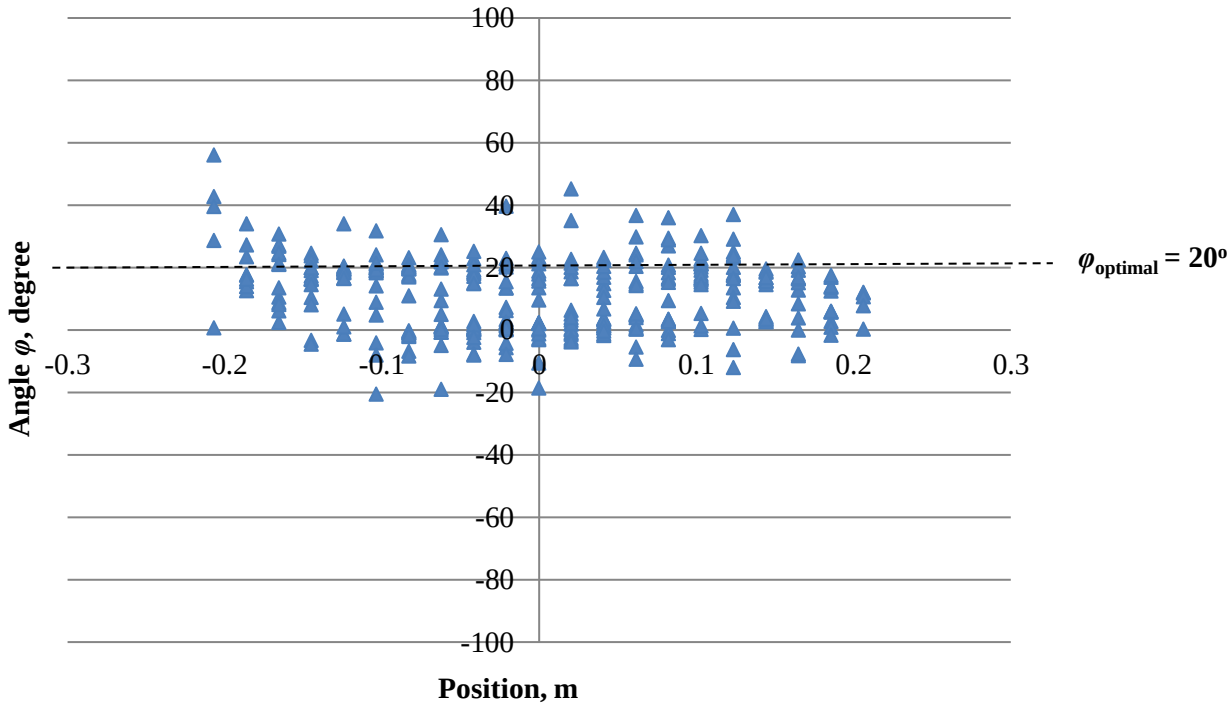

(c) When free stream wind is at 24° to the omni-flow system without the stator

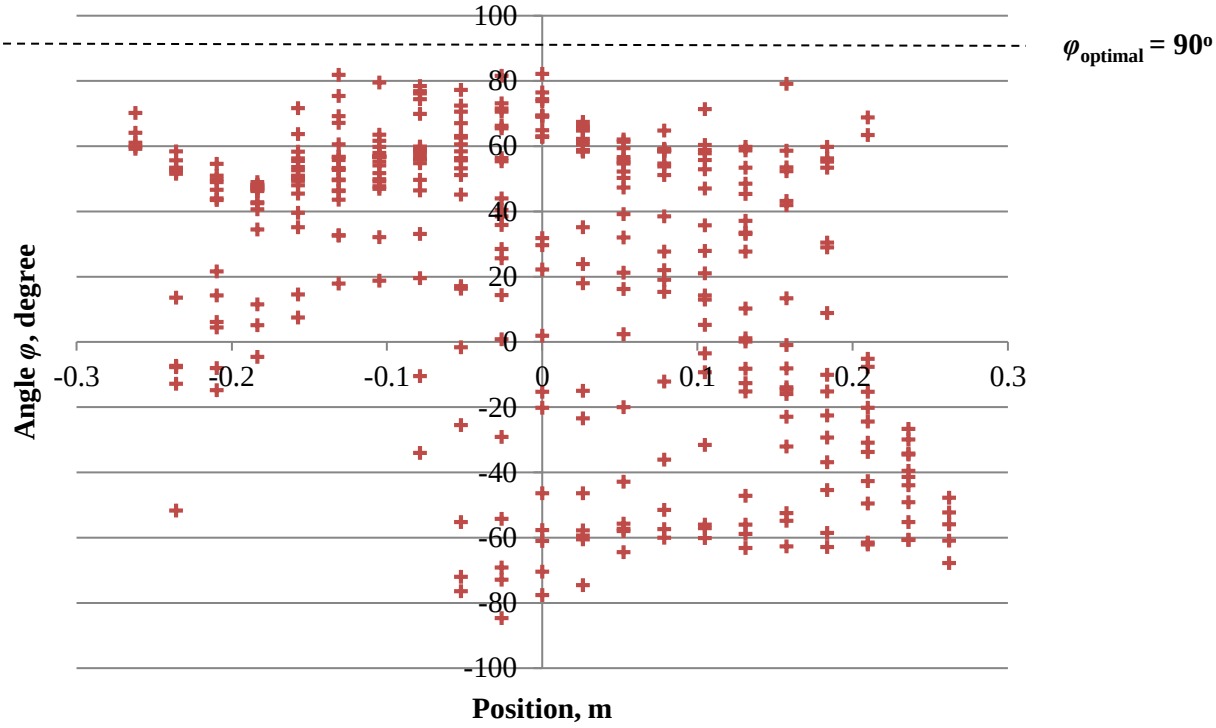

(d) When free-stream wind is at 24° to the omni-flow system with the stator

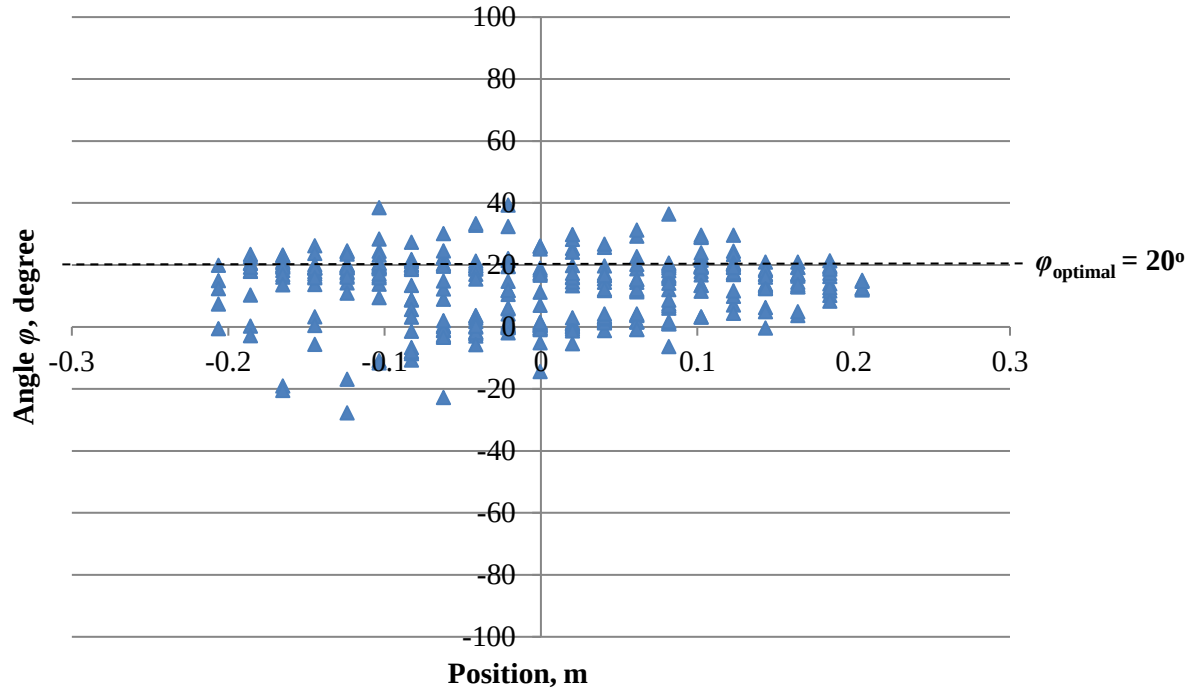

(e) When free stream wind is at 36° to the omni-flow system without the stator

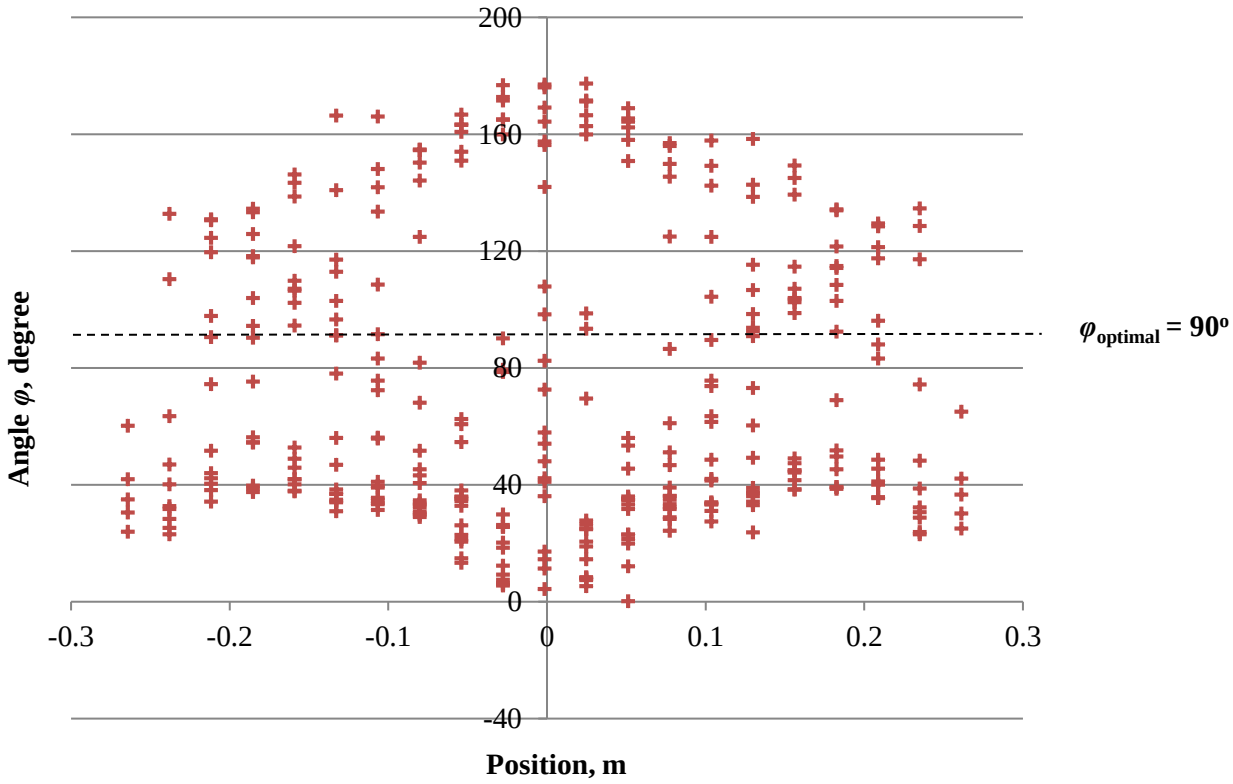

(f) When free stream wind is at 36° to the omni-flow system with the stator